Numerical general relativity and beyond
formation of relativistic axion stars, boosting and colliding oscillotons, and gravitational collapse in khronometric theory

Widdicombe, James

Awarding institution:
King's College London

Numerical General Relativity and Beyond

Formation of Relativistic Axion Stars, Boosting and Colliding Oscillotons, and Gravitational Collapse in Khronometric Theory

James Young Widdicombe

Supervisor: Dr Eugene Lim

Department of Physics
King's College London

A thesis presented for the degree of
Doctor of Philosophy

September 2019

Declaration

I declare that this thesis has been composed solely by myself and that it has not been submitted, in whole or in part, in any previous application for a degree. Except where stated otherwise by reference or acknowledgement, the work presented is entirely my own. This thesis contains fewer than 100,000 words excluding the appendices, bibliography, tables and equations.

James Widdicombe
September 2019

Acknowledgements

I would like to thank my wife, family and friends for all of the support given to me throughout my PhD. Their support has been invaluable, and without them, I would not have been able to get to where I am today.

I am sincerely grateful to my supervisor, Eugene Lim, for the guidance he has given me throughout my PhD, and for giving me the opportunity to undertake it. I would also like to thank and acknowledge his contributions to the work presented in this thesis.

I would like to thank the GRChombo team [1], the COSMOS team at DAMTP, Cambridge University, and Intel for their technical support throughout my PhD, as well as allowing me to contribute towards their collaboration. Without them, the research carried out in this PhD would not have been possible. I would especially like to thank Katy Clough for guiding me when I first started my PhD, and for proofreading this work. In addition, I am grateful to Thomas Helfer, Josu Aurrekoetxea and Rupert Widdicombe for proofreading. In the research presented in this thesis, simulations were performed on several supercomputers:

- COSMOS, CSD3 Peta4 and Leicester DiAL (Data Intensive Cluster), funded by DIRAC/BIS
- ARCHER UK National Supercomputing Service (http://www.archer.ac.uk), via the ARCHER driving test. They also provided substantial training throughout my PhD
- BSC Marenostrum IV (Tier-0 PRACE grant PPFPWG), by the Supercomputing Centre of Galicia and La Palma Astrophysics Centre (BSC/RES grants AECT-2017-2-0011 and AECT-2017-3-0009)
- SurfSara Cartesius (Tier-1 PRACE grant DECI-14 14DECI0017)
- LRZ SuperMUC Phase 2 (Tier-0 PRACE grant 2018194669)

I would like to thank each centre for their technical support, and for enabling me to undertake my research.

Chap. 2 is based on published research presented in [2]. I would like to thank and acknowledge the contributions of David J E Marsh, Eugene Lim, and Thomas Helfer to the research. I would also like to thank the University of Göttingen for funding my visit to see David J E Marsh during the research process, as well as giving me the opportunity to present my research whilst I was there.

Chap. 3 and Chap. 4 are based on published research presented in [3], and on a second paper that is currently in preparation. I would like to thank Ricardo Becerril for the use of his initial condition code for oscillotons that was used, as well as acknowledging and thanking Thomas Helfer, Eugene Lim, Marcos A.G. Garcia, and Mustafa A. Amin for their contributions.

Chap. 5 is based on unpublished work with Diego Blas, Eugene Lim, and Enrico Barausse. I would like to thank and acknowledge their contributions towards this work.

The visualization toolkit YT [4], Numpy [5] and Matplotlib [6] were used throughout the work presented here. I would like to thank them for providing these packages.

I would like to thank the STFC for the financial support that enabled me to undertake a PhD. I would also like to thank the staff of the Physics department of King's College London, for supporting me throughout my PhD, as well as the staff of the Physics and Astronomy department at Queen Mary, University of London for providing the foundation that enabled me to undertake a PhD. Finally, I would like to thank every teacher and mentor I have had growing up.

Abstract

General Relativity (GR) is one of the wonders of the modern era. It beautifully predicts the nature of a strong gravitational field, and there are many exact analytical solutions that describe the world around us using GR. However there are many more scenarios that cannot be solved analytically, and furthermore, there are scenarios in which GR no longer makes sense.

This thesis concerns itself with investigating these scenarios numerically using Numerical General Relativity (NR), as well as numerically probing what lies beyond GR, by studying a form of Lorentz-Violating gravity known as Khronometric Theory. The NR simulations were carried out using GRChombo, which is a new open source code C++ 14, hybrid MPI/OpenMP code that utilises adaptive mesh refinement.

Using GRChombo, we study the formation of compact axion stars and black holes (BH) with aspherical initial conditions that could represent the final stages of axion dark matter structure formation. We show that the final states of such collapse closely follow the known relationship of initial mass and axion decay constant f_a. We demonstrate with a toy model how this information can be used to scan a model density field to predict the number densities and masses of axion stars and BH. In addition to being detectable by the LIGO/VIRGO gravitational wave interferometer network for axion mass of $10^9 < m_a < 10^{11}$ eV, we show using peak statistics that for $f_a < 0.2M_{pl}$, there exists a "mass gap" between the masses of axion stars and BH formed from collapse.

We investigate the physics of black hole formation from the head-on collisions of boosted equal mass oscillotons (OS) in NR, for both the cases where the OS have equal phases or are maximally off-phase (anti-phase). While unboosted OS collisions will form a BH as long as their initial compactness $\mathcal{C} \equiv GM/R$ is above a numerically determined critical value $\mathcal{C} > 0.035$, we find that imparting a small initial boost counter-intuitively *prevents* the formation of black holes even if $\mathcal{C} > 0.035$. If the boost is further increased, at very high boosts $\gamma > 1/12\mathcal{C}$, BH formation occurs as predicted by the hoop conjecture, leading to a "stability band" where collisions result in either the OS "passing through" (equal phase) or "bouncing back" (anti-phase), with a "critical point" occurring around $\mathcal{C} \approx 0.07$. We argue that the existence of this stability band can be explained by the competition between the

free fall and the interaction timescales of the collision. Furthermore we provide an in-depth explanation of the construction of initial data for a pair of boosted OS as well as the modifications needed during evolution, and comment on the potential for further study.

In the final part of this thesis, we investigate spherically symmetric gravitational collapse in Khronometric Theory. The system of equations is solved numerically using code written in C utilising the PETSc tool kit. We comment on a number of instabilities within the system and attempt to demonstrate why these exist. We attempt to regularise the system using a method from 1+1D spherically symmetric GR, however even after this regularisation the system does not appear to be stable. Finally, we comment on some ideas that could be used to stabilise the system both numerically and analytically, as well as discussing recent work by others in the field.

Contents

List of Figures

Chapter 1

Introduction

"Computers make excellent and efficient servants, but I have no wish to serve under them."

Mr Spock
Star Trek: The Original Series

We are in a new golden era of astronomy thanks to the historic measurements of gravitational waves (GW) from the binary coalescence of black holes (BH) [7–12] (see Fig. 1.1) and neutron stars [13]. The detection of GW170817 further pushed our understanding with the first multi-messenger detection of GWs and electromagnetic signals [14, 15]. It would seem that we are standing on the edge of unravelling some of the mysteries of our universe.

But what are the mysteries of the universe that could be unravelled with GWs? Simply put, our whole universe is a mystery. We only understand 5% of the matter content of the universe, with the rest being comprised mostly of dark matter and dark energy[1]. If one was to detect an unknown GW signal, it could tell us about these unknown components of the universe, or more specifically, it could tell us about exotic compact objects (ECOs) that could be comprised of these components.

Our question, and thus the mission of this thesis can now be defined. We want to understand the ECOs that could give rise to potentially unknown GWs. Specifically, we select that the ECOs will be comprised of axions, a theoretical type of dark matter, and hence, these objects are studied in Chap. 2, Chap. 3, and Chap. 4. We study the ECOs by numerically simulating them in full Numerical General Relativity (NR) using GRChombo [1]. Within this thesis, we also study a form of modified gravity known as Khronometric Theory in Chap. 5. Since this topic represents a new direction of which is independent of other work presented in this thesis, the

[1]We will revisit this point in more detail in Sec. 1.3

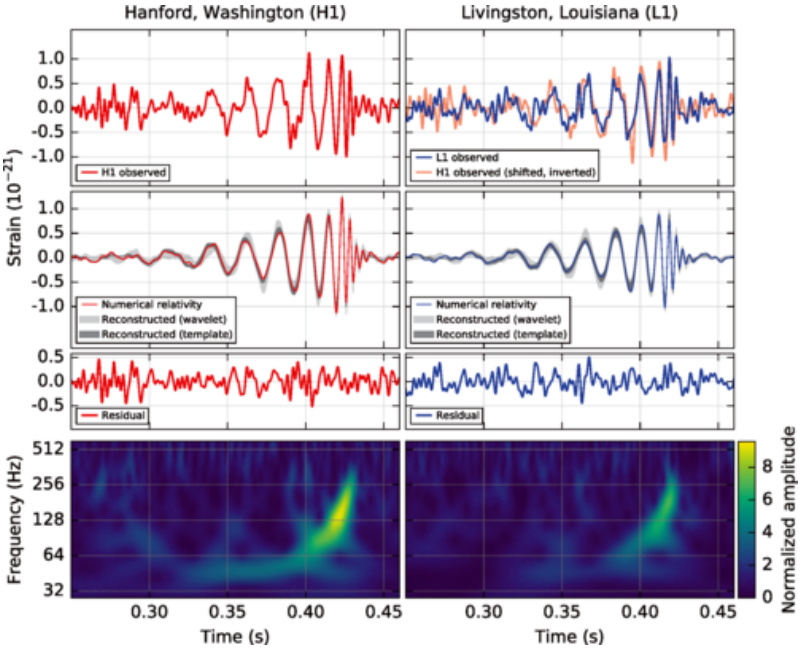

Figure 1.1: The GW event of GW150914, which was the first binary black hole coalescence GW signal to be detected in human history. The panels show the event at two detectors, both of which belong to the LIGO collaboration, and can be seen to be in agreement with each other, as well as with a NR waveform. Since this signal was detected, many more GW events have been observed. Image from [7].

introductory material for that research is confined to that chapter to preserve a logical flow.

Over the course of this chapter, we will provide the background material necessary for this thesis. We will provide some details on General Relativity[2] (GR), and then introduce, in detail, NR. We continue the chapter by exploring Cosmology and Dark Matter (DM), where we provide more details on axions, and "axion stars"; an ECO that is comprised of axions. The chapter ends with an overview of the code we used to conduct the research presented here[3].

Throughout this thesis we will be using Einstein Summation Convention, with Greek indices, $(\alpha, \beta, \mu, \nu, ...)$, referring to four dimensional spacetime, and running from 0 to 3, and Latin indices, $(i, j, k, l, ...)$ referring 3 dimensional space and taking the values 1 to 3. The signature of the spacetime metric is taken to be $(-1, +1, +1, +1)$, and unless otherwise specified we use the units that $\hbar = c = 1$ and, we use the reduced Planck mass $M_{pl} = 1/\sqrt{8\pi G}$. Other conventions will be described within text of the appropriate chapter.

[2]It should be noted that this section is not intended to be a detailed introduction to the subject, and instead we refer the reader to any other standard textbook, for example Schutz [16] or Carroll [17].

[3]As previously stated, all background information necessary for the understanding of Khronometric Theory is presented within the research chapter itself.

1.1 General Relativity

When Einstein introduced the theory of Special Relativity (SR) [18, 19] in 1905, it became clear that Newton's theory of gravity would need to be modified. This is due to the fact that Newtonian gravity implies that gravitational interaction is transmitted between bodies at infinite speed, in sheer contrast to SR; which states that no physical interaction can travel faster then the speed of light [20, p.1]. Thus, at the end of 1915, Einstein postulated General Relativity (GR) [21]; which is what we now consider to be the modern theory of gravitation.

Simply put, GR considers that gravity is not a force, and instead it is a manifestation of the curvature of spacetime. A massive object will cause a "bending" in spacetime, and subsequently that "bending" then controls the movement of physical objects. This can be summarised more beautifully, by the words of John A. Wheeler [22] as:

"Matter tells spacetime how to curve, and spacetime tells matter how to move."

Although these words are beautiful, a far more informative[4] description of GR, is presented in it's mathematical form via the Einstein Field Equations (EFEs). These are defined as

$$G_{\mu\nu} = M_{pl}^{-2} T_{\mu\nu} \,, \tag{1.1}$$

where M_{pl} is the reduced Planck mass, $T_{\mu\nu}$ is the energy-momentum (EM) tensor, and $G_{\mu\nu}$ is the Einstein tensor defined as

$$G_{\mu\nu} = R_{\mu\nu} - \frac{1}{2} R g_{\mu\nu} \,, \tag{1.2}$$

where $R_{\mu\nu}$ is the Ricci tensor, R is the Ricci scalar, and $g_{\mu\nu}$ is the metric tensor. The components of this equation shall be discussed later in the section, but for now it's sufficient to say that the Einstein tensor encodes the curvature of spacetime, whereas the EM tensor encodes the matter source. One can see that the EFEs are written using tensors that are invariant under coordinate transform, and hence, are a direct consequence of *The Principle of General Covariance*; that states the laws of physics must be invariant under coordinate transform, and hence, the same for all observers.

GR is in-fact based on two key principles; *The Principle of General Covariance*, as stated before, and the *Einstein Equivalence Principle* (EEP). The EEP states in a free-falling reference frame gravitational *force* effectively vanishes, and the laws of physics apply just like they do in SR. In other words, the EEP implies that

[4] Some may consider the mathematical form of GR far more beautiful then any combination of words used to describe it.

there exists local inertial frames. However, it should be noted that in a non-uniform gravitational field, these local inertial frames cannot be "glued" together to form a global inertial frame.

Geometrically, we can describe the EEP by saying that locally we can have a spacetime metric that is that of Minkowski. The fact that there is no global inertial frame corresponds to saying that there is no set of coordinates in which the spacetime metric has this form everywhere. This is an equivalent statement to the description of a curved manifold, which is the fundamental basis that GR is built on [20, p.28].

The mathematical basis for GR is complex, and one could write many chapters describing it. Instead here, using the notation of [20], we will briefly describe some key things that are helpful to the reader.

Extending the concept of the spacetime interval, $ds^2 = \eta_{\mu\nu}dx^\mu dx^\nu$, between two points in SR, we can "promote" the flat space metric (also known as the Minkowski interval), $\eta_{\mu\nu}$, to the metric tensor, $g_{\mu\nu}$, such that

$$ds^2 = g_{\mu\nu}dx^\mu dx^\nu \,. \tag{1.3}$$

The metric tensor can also be defined to as a one-to-one mapping between one forms and vectors, and as such can be used to *raise* and *lower* indices, e.g

$$v^\mu = g^{\mu\nu}v_\nu \,, \quad v_\nu = g_{\mu\nu}v^\mu \,, \quad L_{\mu\nu} = g_{\mu\alpha}g_{\nu\beta}L^{\alpha\beta} \,, \tag{1.4}$$

where $g^{\mu\nu}$ is the inverse of $g_{\mu\nu}$, and we have shown how this notion *raising* and *lowering* indices can be generalised to the notion of a tensor, $L_{\mu\nu}$. When taking the derivative of a tensor, one must also consider how the basis vectors change from one place on the manifold to another. We can signify this by replacing the partial derivatives, ∂_α, that would be taken in flat space, with a covariant derivative, such that

$$\nabla_\alpha p^\beta = \partial_\alpha p^\beta + p^\mu \Gamma^\beta_{\alpha\mu} \,, \quad \nabla_\alpha p_\beta = \partial_\alpha p_\beta - p_\mu \Gamma^\beta_{\alpha\mu} \,, \tag{1.5}$$

where ∇_μ is the covariant derivative[5], and we define the metric compatible Christoffel symbol, $\Gamma^\gamma{}_{\alpha\beta}$, to be

$$\Gamma^\gamma{}_{\alpha\beta} = \frac{1}{2}g^{\gamma\sigma}(\partial_\alpha g_{\sigma\beta} + \partial_\beta g_{\sigma\alpha} - \partial_\sigma g_{\alpha\beta}) \,. \tag{1.6}$$

[5]It should be noted that other notation can sometimes be used to define the covariant derivative, such as $\nabla_\mu v_\nu = v_{\nu;\mu} = D_\mu v_\nu$. In this chapter we will use ∇_μ to symbolise the covariant derivative, and where other versions are used, it will clearly be written in the text.

For completeness, we define the covariant derivative of a 2 rank tensor is

$$\begin{aligned}
\nabla_\alpha L^{\mu\nu} &= \partial_\alpha L^{\mu\nu} + \Gamma^\mu_{\alpha\beta} L^{\beta\nu} + \Gamma^\nu_{\alpha\beta} L^{\mu\beta}\,, \\
\nabla_\alpha L_{\mu\nu} &= \partial_\alpha L_{\mu\nu} - \Gamma^\beta_{\alpha\mu} L_{\beta\nu} - \Gamma^\beta_{\alpha\nu} L_{\mu\beta}\,, \\
\nabla_\alpha L^\mu{}_\nu &= \partial_\alpha L^\mu{}_\nu + \Gamma^\mu_{\alpha\beta} L^\beta{}_\nu - \Gamma^\beta_{\alpha\nu} L^\mu{}_\beta\,.
\end{aligned} \tag{1.7}$$

Using Eqn. (1.7), one can then calculate the covariant derivative of any tensor. The map defined by the Christoffel symbols, defines the notion of *parallel transport*, which allows us to drag a vector along a certain curve keeping it unchanged. Note that we do not need the Christoffel symbols explicitly defined by the metric for this definition, and hence, in this situation the Christoffel symbols are referred to as the connection coefficients.

Using the concept of parallel transport, one can define a tensor associated with the curvature of a manifold by considering the parallel transport of a vector, $\vec{v}$, along a closed circuit. We define this tensor as the Riemann tensor, $R^\epsilon{}_{\mu\nu\sigma}$, and can equivalently (and more easily be defined) as the commutator of covariant derivative acting on vector such that

$$[\nabla_\nu, \nabla_\sigma] v^\epsilon = R^\epsilon{}_{\mu\nu\sigma} v^\mu \tag{1.8}$$

with the Riemann tensor explicitly defined as

$$R^\epsilon{}_{\mu\nu\sigma} = -\partial_\sigma \Gamma^\epsilon{}_{\mu\nu} + \partial_\nu \Gamma^\epsilon{}_{\mu\sigma} + \Gamma^\alpha{}_{\mu\sigma} \Gamma^\epsilon{}_{\alpha\nu} - \Gamma^\alpha{}_{\mu\nu} \Gamma^\epsilon{}_{\alpha\sigma}\,. \tag{1.9}$$

In flat space all components of the Riemann tensor vanish. The various symmetries of the Riemann tensor imply that in 4 dimensions there are only 20 independent components, and also imply that the trace over the first and last pairs of indices vanish. The trace over the first and third index, does not vanish, and as such we can define the Ricci tensor as

$$R_{\mu\alpha} \equiv R^\mu{}_{\nu\mu\alpha}\,. \tag{1.10}$$

The Ricci tensor is symmetric, and hence, in 4 dimensions has 10 independent components. Therefore it should be noted, that even if the Ricci tensor vanishes, components of the Riemann tensor may not. One can finally define the Ricci (or Scalar) curvature, R,

$$R \equiv R^\mu{}_\mu\,. \tag{1.11}$$

With these terms defined, one can see that the Einstein Tensor defined in Eqn. (1.2), contains terms that define curvature. One can get intuition for the RHS of the EFEs

by considering the physical interpretations of the EM tensor

$$T^{00} = \text{energy density}\,, \tag{1.12}$$

$$T^{0i} = \text{momentum density}\,, \tag{1.13}$$

$$T^{ij} = \text{flux of } i \text{ in direction } j\,. \tag{1.14}$$

In general, the EM tensor is symmetric, and in GR, we refer to any source for it as matter (for example a scalar field we would use the terminology of scalar field matter). A black hole will have an EM tensor equal to 0. With the EM tensor defined, one can then construct various scenarios to study many interesting phenomena using GR.

GR has many observable consequences which have been used to validate the theory from its inception. In 1916, Einstein [23] suggested 3 tests of GR to test some of these consequences: 1) the perihelion precession of Mercury's orbit, which was immediately verified by work done by Levenier in 1845; 2) the deflection of light by the Sun, which is predicted by GR and not Newtonian gravity, and observed by Eddington in 1919 [24]; and 3) the gravitational redshift of light which was observed in 1959 in the Pound-Rebka experiment [25]. Furthermore, GR is tested on a daily basis by anyone who uses GPS!

Recently, one of the most popular consequences of GR has been the existence, and subsequent detections [7–13] of GWs. Simply put, GWs are propagating waves in spacetime emitted by the relative motion of masses. Thus far, GWs of the binary coalescence of both black holes and neutron stars have been detected by the LIGO/Virgo collaboration. Within this theses, we approximate the GW signals that could be emitted by the binary coalescence of a class of ECOs known as axion stars, which is studied in Chap. 2. We will provide the reader with information as to what an axion star is in Sec. 1.3.5.

1.2 Numerical General Relativity

Einstein's theory of General Relativity (GR) beautifully describes the nature of a strong gravitational field, and mathematically can be written as the Einstein Field equations (EFEs), Eqn. (1.1), which describes the relationship between curvature and matter. Their exists many exact analytical solutions to the EFEs, however, their are many more scenarios in which the equations cannot be solved analytically. For example, if one has a large amount of asymmetry in space and/or time NR is usually required. We want to study these scenarios, but how can one do so when there is no analytical solution? Simply put, we can reformulate the EFEs into a form that can be solved numerically, such that we can study the dynamics of the

chosen scenario, by providing initial data at some initial time, t_0, and evolving it numerically to some final time, t_f. In the following section we will study how to reformulate the EFEs to achieve this, and we will be using notation and formalism from [17, 20, 26–28][6].

1.2.1 3+1 split of spacetime

To describe scenarios which have no analytical solutions to the EFEs, we want to initially provide data at some time, t_0, evolving it numerically to some final time, t_f, and then interpret the corresponding dynamics of the system. The formulation of such a system is known as an "initial value" or "Cauchy problem": *"Given adequate initial (and boundary) conditions, the fundamental equations must predict the future (or past) evolution of the system"* [20, p.65].

The EFEs are written in such a way that space and time are treated equally, i.e spacetime, and as such, one cannot easily describe the evolution of a system forwards in time. Therefore, it would appear that to achieve our desired formulation, we need to explicitly split spacetime into space and time. This is known as the "3+1 formalism", and here we will be specifically describing the ADM (Arnowitt Deser Misner) [29] decomposition of spacetime, that was later reformulated by York [30].

We consider a globally hyperbolic spacetime with the metric $g_{\alpha\beta}$. Any globally hyperbolic spacetime can be completely foliated into non-intersecting spacelike hypersurfaces, Σ_i (see Fig. 1.2). We can identify the foliation with a scalar function, t, that can be interpreted as a global or universal time function.

Consider a specific foliation with two adjacent spacelike hypersurfaces, Σ_t, and Σ_{t+dt}. The geometry of the spacetime can then be determined with the following 3 definitions (see Fig. 1.3):

- The 3D metric, γ_{ij}, that measures proper distance within the hypersurface -

$$dl^2 = \gamma_{ij} dx^i dx^j \,. \tag{1.15}$$

- The lapse, $\alpha(t, x^i)$, of proper time, $d\tau$, between both hypersurfaces measured by an observer moving along the normal to those hypersurfaces -

$$d\tau = \alpha(t, x^i) dt \,. \tag{1.16}$$

- The relative velocity, $\beta^i(t, x^j)$, between the observers and the lines of constant

[6] It should be noted that although the notation and formalism was used from throughout [17, 20, 26–28], the ordering of the presentation reflects that of [20]

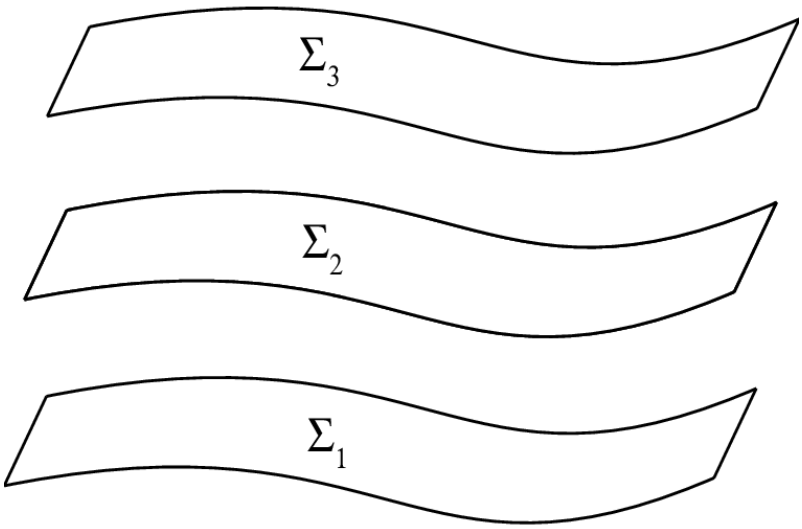

Figure 1.2: A schematic of the foliation of a globally hyperbolic spacetime into spacelike hypersurfaces, labelled Σ_i. Image from [31].

spatial coordinates -

$$x^i_{t+dt} = x^i_t - \beta^i(t, x^j)dt\,, \tag{1.17}$$

where we will define the relative velocity as the shift vector.

The choice in which one foliates the spacetime into spacelike hypersurfaces is not unique, and neither is the way in which the spatial coordinates propagate from one hypersurface to another, therefore it should be noted that the lapse, $\alpha(t, x^i)$, and the shift vector, $\beta^i(t, x^j)$, are freely specifiable, and are known as gauge functions (see Sec. 1.2.5 for a full discussion).

Using the 3 definitions above, the metric takes the following form

$$ds^2 = (-\alpha^2 + \beta_i\beta^i)dt^2 + 2\beta_i dt dx^i + \gamma_{ij}dx^i dx^j\,, \tag{1.18}$$

where $\beta_i = \gamma_{ij}\beta^j$. One can then define a unit normal vector, n^μ, to the hypersurfaces such that

$$n^\mu = (\alpha^{-1}, -\beta^i/\alpha), \;\; n_\mu = (-\alpha, 0)\,. \tag{1.19}$$

The normal vector will be used in what follows, and it should be noted that we are free to choose the sign of the normal vector, and as such, here we have chosen it in a way to ensure it is future pointing.

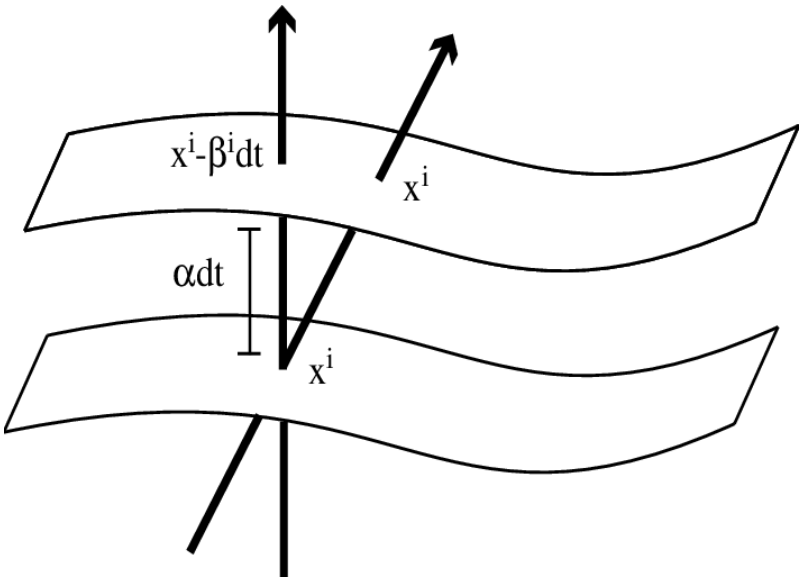

Figure 1.3: A schematic of two adjacent spacelike hypersurfaces, Σ_t, and Σ_{t+dt} with the definitions of the lapse, α and the shift, β^i. Image from [31].

1.2.2 Extrinsic curvature

We have defined the foliation of spacetime via choosing spacelike hypersurfaces, and as such, we must distinguish the difference between the intrinsic curvature (the curvature coming from internal geometry), and the extrinsic curvature (curvature coming from the way the hypersurfaces are immersed in 4D spacetime).

The intrinsic curvature is simply defined as the 3D Riemann tensor, ${}^{(3)}R_{abcd}$, in terms of the spatial metric, γ_{ij}. The extrinsic curvature, $K_{\alpha\beta}$, is defined as the change to the normal vector, as it is parallel transported from one point on the hypersurface to another [20, p.69].

To mathematically define the extrinsic curvature, $K_{\alpha\beta}$, we must first define the projector operator P^α_β onto the spatial hypersurfaces

$$P^\alpha_\beta = \delta^\alpha_\beta + n^\alpha n_\beta \,. \tag{1.20}$$

Using the projection operator, P^α_β, the extrinsic curvature, $K_{\alpha\beta}$, is defined as

$$K_{\alpha\beta} = -P^\mu_\alpha \nabla_\mu n_\beta \,. \tag{1.21}$$

$K_{\alpha\beta}$ is a purely spatial tensor i.e $K_{\alpha\beta} \to K_{ij}$ and is symmetric. Using this knowledge, as well as the definition of the projection operator, one finds that the extrinsic curvature is defined as

$$K_{ij} = \frac{-1}{2\alpha}\left(-\partial_t \gamma_{ij} + D_j\beta_i + D_i\beta_j\right) \,, \tag{1.22}$$

where we define D_i as the 3D covariant derivative associated the spatial metric, γ_{ij}, and is nothing more then the projection of the 4D covariant derivative, $D_\beta = P^\alpha_\beta \nabla_\alpha$. Notice that one can rearrange the definition of the extrinsic curvature, K_{ij}, such that

$$\partial_t \gamma_{ij} = -2\alpha K_{ij} + D_i \beta_j + D_j \beta_i \,. \tag{1.23}$$

We have just defined the time evolution of the spatial metric, γ_{ij}, and as such have obtained our first set of evolution equations. This was obtained only from geometric principles, it is clear that to obtain the remaining evolution equations, one must use the EFEs.

1.2.3 Constraint equations

As the dynamics of a gravitational field are contained within the EFEs, one must consider them. This is done via a series of projections onto the spatial hypersurface, and normal to it, of the Riemann tensor, and then substituting the EFEs into the the results of the projections. The full projection of the Riemann tensor onto the spatial hypersurfaces is known as the Gauss-Codazzi equations[7]

$$P^\delta_\alpha P^\kappa_\beta P^\lambda_\mu P^\sigma_\nu R_{\delta\kappa\lambda\sigma} = {}^{(3)}R_{\alpha\beta\mu\nu} + K_{\alpha\mu}K_{\beta\nu} - K_{\alpha\nu}K_{\beta\mu} \,. \tag{1.24}$$

Contracting both sides by $g^{\alpha\mu} g^{\beta\nu}$ we find that

$$2 n^\mu n^\nu G_{\mu\nu} = {}^{(3)}R + K^2 - K_{\mu\nu}K^{\mu\nu} \,. \tag{1.25}$$

Rearranging, and using the EFEs, the resultant is

$$\mathcal{H} \equiv R + K^2 - K_{ij}K^{ij} - 16\pi G\rho = 0 \,, \tag{1.26}$$

where we have defined $\rho \equiv n^\mu n^\nu T_{\mu\nu}$, and used the fact that the extrinsic curvature is a purely spatial tensor. This equation has no explicit time derivatives, and as such, is not an evolution equation. Rather it is a constraint equation, and must be satisfied at all times. We refer to this equation as the Hamiltonian constraint equation, $\mathcal{H}$, although in literature sometimes it is referred to as the energy constraint equation.

The projection of the Riemann tensor onto the spatial hypersurfaces contacted once with the normal vector is known as the Codazzi-Mainardi equations

$$P^\delta_\alpha P^\kappa_\beta P^\lambda_\mu n^\nu R_{\delta\kappa\lambda\nu} = D_\beta K_{\alpha\mu} - D_\alpha K_{\beta\mu} \,. \tag{1.27}$$

[7] We will omit the lengthy derivations from this section but the interested reader can find more details in [26].

Contracting both sides twice yields

$$P^{\alpha\mu}n^{\nu}G_{\mu\nu} = D^{\alpha}K - D_{\mu}K^{\alpha\mu}\,. \tag{1.28}$$

Rearranging, and using the EFEs we find that

$$\mathcal{M}^{i} \equiv D_{j}(K^{ij} - \gamma^{ij}K) - 8\pi G S^{i} = 0\,, \tag{1.29}$$

where we have defined $S^{i} \equiv -P^{i\mu}n^{\nu}T_{\mu\nu}$, and again we have used the fact that the extrinsic curvature is a purely spatial tensor. As before with the Hamiltonian constraint equation, these equations contain no time derivatives, and as such are constraint equations. These are known as the momentum constraint equations, $\mathcal{M}^{i}$.

The Hamiltonian, Eqn. (1.26), and Momentum, Eqn. (1.29), constraint equations allow a 3 dimensional slice with data to be embedded in a 4 dimensional spacetime. They are independent of all gauge functions, and imply that the initial data for the EFEs cannot be freely prescribed. A discussion on providing initial data that satisfy these equations is given in Sec. 1.2.5.

1.2.4 Evolution equations

As previously shown in Sec. 1.2.2, we have obtained 6 evolution equations, Eqn. (1.23), that relate to the dynamics of the variables from geometrical principles. Here we shall obtain the remaining evolution equations that correspond to the evolution of the gravitational field. To begin, we contract Eqn. (1.24) by $g^{\alpha\mu}$ such that

$$P^{\kappa}_{\beta}P^{\sigma}_{\nu}(R_{\kappa\sigma} + n^{\delta}n^{\lambda}R_{\delta\kappa\lambda\sigma}) = {}^{(3)}R_{\beta\nu} + KK_{\beta\nu} - K_{\alpha\nu}K^{\alpha}_{\beta}\,. \tag{1.30}$$

The projection of the Riemann tensor contracted twice by the normal vector can be shown to be

$$P^{\kappa}_{\beta}P^{\sigma}_{\nu}n^{\delta}n^{\lambda}R_{\delta\kappa\lambda\sigma} = \left(n^{\zeta}D_{\zeta}K_{\beta\nu} + K_{\beta\zeta}D_{\nu}n^{\zeta} + K_{\zeta\nu}D_{\beta}n^{\zeta}\right) + K_{\beta\lambda}K^{\lambda}_{\nu} + \frac{1}{\alpha}D_{\beta}D_{\nu}\alpha\,. \tag{1.31}$$

Next, using an alternative form of the EFEs

$$R_{\mu\nu} = 8\pi G\left(T_{\mu\nu} - \frac{1}{2}g_{\mu\nu}T\right)\,, \tag{1.32}$$

one can show that the time evolution of the extrinsic curvature, K_{ij} is

$$\begin{aligned}\partial_{t}K_{ij} = {}&\beta^{k}\partial_{k}K_{ij} + K_{ki}\partial_{j}\beta^{k} + K_{kj}\partial_{i}\beta^{k} - D_{i}D_{j}\alpha \\ &+ \alpha\left({}^{(3)}R_{ij} + KK_{ij} - 2K_{ik}K^{k}_{j}\right) + 4\pi\alpha\left(\gamma_{ij}(S-\rho) - 2S_{ij}\right)\,,\end{aligned} \tag{1.33}$$

where $S \equiv S^i{}_i$ and $S_{ij} \equiv \gamma_{i\mu}\gamma_{j\nu}T^{\mu\nu}$. Together with Eqn. (1.23), these are the full 12 set of evolution equations that are known as the ADM equations [29, 30], although the ones presented here are the ones reformulated by York [30]. These equations, together with the constraint equations, are completely equivalent to the EFEs, and therefore allows us to write the EFEs as a Cauchy problem. It is possible to show that using the Bianchi identities [32], that the evolution equations imply that if the constraint equations are initially satisfied, then they will continue to be satisfied throughout evolution. Therefore one only has to solve the constraint equations at time, t_0.

It should be noted that we do not have evolution equations for the gauge quantities, and we can choose these freely. The following section, Sec. 1.2.5, will discuss this in more depth, as well as how to construct initial data.

1.2.5 Initial data and lapse condition

The existence of the Hamiltonian, Eqn. (1.26), and Momentum, Eqn. (1.29), constraint equations implies that we are not free to arbitrarily choose initial data for all 12 dynamical quantities $\{\gamma_{ij}, K_{ij}\}$. Instead, the initial data must be chosen in a way that satisfies these constraints, as well as to represent physical values of the scenario in which one wishes to simulate.

The constraint equations remove 4 of the 12 degrees of freedom for the initial data. They are partial differential equations of the elliptical type, and in general are difficult to solve. There exists two common methods to solve the constraint equations in specific scenarios; which are the conformal decomposition of York and Lichnerowicz [33–35], and the thin-sandwich technique [36]. Neither of these methods are used in the research in this thesis, however we encourage the interested reader to refer to the original sources, or [20], for a review. Instead, throughout this thesis two simple techniques are used:

1. We can consider the metric to be conformally flat, which removes 5 of the 8 remaining degrees of freedom, and then we are left to impose some condition for the extrinsic curvature to remove the remaining 3. This technique was used in Chap. 2, and the specifics of the conditions that were imposed for the extrinsic curvature are given in Sec. 2.3.3.

2. One can consider specific symmetries with the initial data, e.g spherical symmetry, which greatly simplifies initial data generation. This was done for the research presented in Chap. 3 and Chap. 4.

After initial data has been set for the 12 dynamical variables, $\{\gamma_{ij}, K_{ij}\}$, one can ask what values to assign initially to the 4 gauge conditions, $\{\alpha, \beta_i\}$, and furthermore

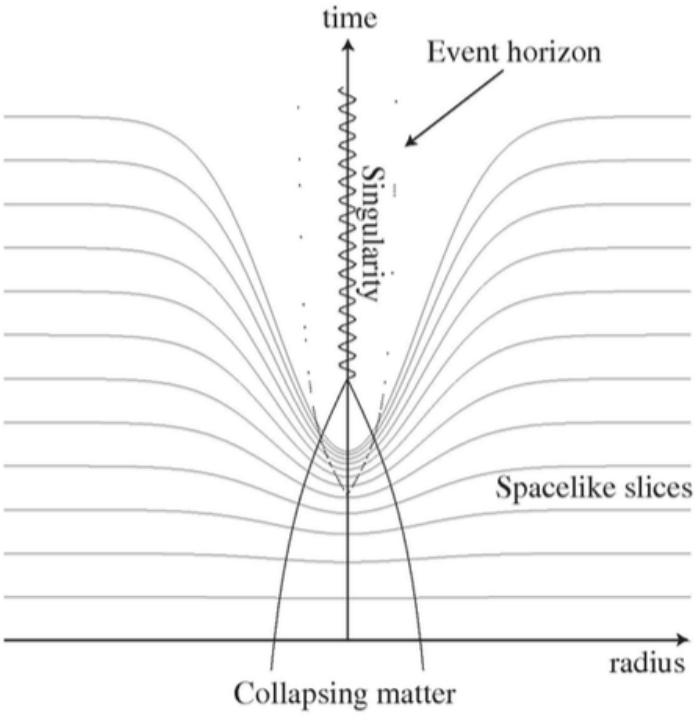

Figure 1.4: A schematic view of the collapse of the lapse when approaching a singularity. Image from [20].

how these gauge conditions evolve. These can be freely set, however, there are choices that will aid numerical stability.

In order to prescribe the foliation of the spacelike hypersurfaces, we need to calculate the lapse function, $\alpha(t, x^i)$. The most obvious choice, and used in early work in the 1960s [37], is to set $\alpha(t, x^i) = 1$, and is known as geodesic slicing. However, this is a very poor coordinate choice, as if one thinks about observers in freefall in a non-uniform gravitational field, different observers will fall in different directions, and there is nothing stopping them from eventually colliding. When this happens the coordinate system stops being one to one and is singular i.e the observers have become "focused" by the gravitational field [20, p.123].

To consider a solution to the "focusing" effect, one can first consider the evolution of the trace of the extrinsic curvature, K,

$$\partial_t K = \beta^i \partial_i K - D^2\alpha + \alpha \left[K_{ij} K^{ij} + 4\pi(\rho + S) \right] , \tag{1.34}$$

where the Hamiltonian constraint equation has been used to eliminate the Ricci scalar. With geodesic slicing, this becomes

$$\partial_t K - \beta^i \partial_i K = \left[K_{ij} K^{ij} + 4\pi(\rho + S) \right] . \tag{1.35}$$

The right hand side of above equation is positive if the strong energy condition holds. Hence the extrinsic curvature will grow without bound, and using the relation that $\nabla_\mu n^\mu = -K$, it implies that volume elements will collapse to zero. A solution to this is to ask that

$$\partial_t K = K = 0\,. \tag{1.36}$$

Thus, Eqn. (1.34) becomes

$$D^2\alpha = \alpha\left[K_{ij}K^{ij} + 4\pi(\rho + S)\right]\,. \tag{1.37}$$

This is known as maximal slicing [33], and has a key advantage of singularity avoidance. This means that the condition does not allow the spatial hypersurfaces to come into contact with the physical singularity, as illustrated in Fig. 1.4. However, this slicing condition is not used due to two factors: 1) it is very numerically expensive in 3D due to it being an elliptical equation; and 2) to avoid collision with the singularity, the spatial slices become distorted and, as time progresses, this can result in a rapid growth of gradients around the singularity, which causes numerical codes to fail[8].

In the research that follows we use the Bono-Masso type slicing condition [39], which is designed to be "singularity avoiding". This is achieved via reducing the lapse in areas of high curvature and has the form

$$\partial_t \alpha = -\mu_1 \alpha^{\mu_2} K + \mu_3 \beta^i \partial_i \alpha\,, \tag{1.38}$$

where μ_1, μ_2 and μ_3 are constants, of which the specifics that are used in this thesis will be described in Sec. 1.4. Much like maximal slicing, this condition leads to slice stretching, and as such an appropriate shift condition is needed to counteract this.

For many scenarios, setting the shift, $\beta_i(t, x^i) = 0$ simply works. For other scenarios, setting the shift equal to 0 is a very poor coordinate choice. How to evolve the shift is far less understood then that of the lapse, however, slice stretching can give us some intuition as to how one can set the shift.

Slice stretching causes failure due to large gradients forming around the singularity. One way to counter this is to relabel spatial points such that they shift away from the singularity, and thus reduces the slice stretching effect. An effective way to achieve this is written in the BSSN formulation, and as such, shall be specified in the next section.

[8]This effect is actually a combination of two effects, slice sucking and slice wrapping. We direct the reader to [38] for more information.

1.2.6 BSSN formulation and shift condition

The ADM evolution equations are not unique as one can add arbitrary combinations of the Hamiltonian and Momentum constraint equations to them to obtain new evolution equations. Since the early 1990's, as researchers started to work with full 3D evolution codes, it was found that that ADM lacked the necessary stability properties for long-term numerical simulations[9] [20, p.82], and as such the ADM equations needed to be reformulated. In this section we will discuss a commonly used formulation known as BSSN [40–42], which is used for the numerical simulations conducted in this thesis.

We can first consider a conformal rescaling of the metric, such that

$$\gamma_{ij} = \psi^4 \tilde{\gamma}_{ij} \,, \tag{1.39}$$

where ψ is the conformal factor and $\tilde{\gamma}_{ij}$ is the conformal metric. As per [43], we choose that $\psi^4 = 1/\chi$, as when considering black hole spacetimes, χ goes to zero at the black hole singularity, whereas ψ has a $1/r$ singularity. We choose that $\det \tilde{\gamma}_{ij} = 1$, and that

$$\chi = (\det \gamma_{ij})^{-\frac{1}{3}} \,, \tag{1.40}$$

We demand that this relation remains satisfied throughout evolution. Using Eqn. (1.23), we find that the evolution equation for χ is

$$\partial_t \chi = \frac{2}{3}\alpha\chi K - \frac{2}{3}\chi\partial_k\beta^k + \beta^k\partial_k\chi \,. \tag{1.41}$$

The extrinsic curvature is decomposed into its trace, K, and its tracefree part, A_{ij}, such that

$$A_{ij} = K_{ij} - \frac{1}{3}\gamma_{ij}K \,. \tag{1.42}$$

The tracefree part of the extrinsic curvature is conformally rescaled of the form

$$A_{ij} = \frac{1}{\chi}\tilde{A}_{ij} \,. \tag{1.43}$$

Using the decomposition for the extrinsic curvature, and its conformal scaling, one

[9] This is related to the fact that the ADM evolution equations are only weakly hyperbolic. See [20] for an analysis of this.

can then find the evolution equations to be

$$\partial_t \tilde{\gamma}_{ij} = -2\alpha \tilde{A}_{ij} + \tilde{\gamma}_{ik}\partial_j \beta^k + \tilde{\gamma}_{jk}\partial_i \beta^k - \frac{2}{3}\tilde{\gamma}_{ij}\partial_k \beta^k + \beta^k \partial_k \tilde{\gamma}_{ij} \,, \tag{1.44}$$

$$\partial_t K = -\gamma^{ij} D_i D_j \alpha + \alpha \left(\tilde{A}_{ij}\tilde{A}^{ij} + \frac{1}{3}K^2 \right) + \beta^i \partial_i K + 4\pi G \alpha (\rho + S) \,, \tag{1.45}$$

$$\begin{aligned} \partial_t \tilde{A}_{ij} = {} & \left[-D_i D_j \alpha + \chi \alpha \left(R_{ij} - 8\pi G \alpha S_{ij} \right) \right]^{\mathrm{TF}} + \alpha (K \tilde{A}_{ij} - 2\tilde{A}_{il}\tilde{A}^l{}_j) \\ & + \tilde{A}_{ik}\partial_j \beta^k + \tilde{A}_{jk}\partial_i \beta^k - \frac{2}{3}\tilde{A}_{ij}\partial_k \beta^k + \beta^k \partial_k \tilde{A}_{ij} \,, \end{aligned} \tag{1.46}$$

where in the evolution equation for K, the Hamiltonian constraint equation has been used to eliminate the Ricci Scalar, D_i is the covariant derivative with respect to the physical metric, γ_{ij}, and $[...]^{TF}$ denotes the tracefree part of the expression within the brackets.

We introduce the conformal connections $\tilde{\Gamma}^i = \tilde{\gamma}^{jk}\,\tilde{\Gamma}^i{}_{jk}$ where $\tilde{\Gamma}^i{}_{jk}$ are the Christoffel symbols associated with the conformal metric $\tilde{\gamma}_{ij}$. As $\tilde{\Gamma}^i$ is considered an independent variable, we can then calculate the evolution equations for them as

$$\begin{aligned} \partial_t \tilde{\Gamma}^i = {} & 2\alpha \left(\tilde{\Gamma}^i_{jk}\tilde{A}^{jk} - \frac{2}{3}\tilde{\gamma}^{ij}\partial_j K - \frac{3}{2}\tilde{A}^{ij}\frac{\partial_j \chi}{\chi} \right) - 2\tilde{A}^{ij}\partial_j \alpha + \beta^k \partial_k \tilde{\Gamma}^i \\ & + \tilde{\gamma}^{jk}\partial_j \partial_k \beta^i + \frac{1}{3}\tilde{\gamma}^{ij}\partial_j \partial_k \beta^k + \frac{2}{3}\tilde{\Gamma}^i \partial_k \beta^k - \tilde{\Gamma}^k \partial_k \beta^i - 16\pi G \alpha \tilde{\gamma}^{ij} S_j \,, \end{aligned} \tag{1.47}$$

where the divergence of the of $\tilde{A}_{ij}$ has been replaced with the momentum constraint, as, without this substitution the equations are violently unstable. In the evolution equations for $\tilde{A}_{ij}$, we need to calculate the Ricci tensor associated with the physical metric, which can be separated as

$$R_{ij} = \tilde{R}_{ij} + R^{\chi}_{ij} \,, \tag{1.48}$$

where $\tilde{R}_{ij}$ is the Ricci tensor associated with the conformal metric

$$\tilde{R}_{ij} = -\frac{1}{2}\tilde{\gamma}^{lm}\partial_l \partial_m \tilde{\gamma}_{ij} + \tilde{\gamma}_{k(i}\partial_{j)}\tilde{\Gamma}^k + \tilde{\Gamma}^k \tilde{\Gamma}_{(ij)k} + \tilde{\gamma}^{lm}\left(2\tilde{\Gamma}^k_{(li}\tilde{\Gamma}_{j)km} + \tilde{\Gamma}^k_{im}\tilde{\Gamma}_{klj} \right) \,, \tag{1.49}$$

and R^{χ}_{ij} denotes additional terms that depend on χ. One should note that we now use the derivative of the evolved $\tilde{\Gamma}^i$ in the calculation of the Ricci tensor. The BSSN formulation turns out to be far more stable[10] then ADM in all cases studied until now [20, p.87], and it is the formulation which is used to conduct the numerical simulations throughout this thesis.

With the BSSN formulation introduced, one can now specify a shift condition

[10]This stability comes from the fact that the formulation is strongly hyperbolic, which was shown by Sarbach et al [44].

that reduces the slice stretching effect that was described in Sec. 1.2.5. Noting that, $\tilde{\Gamma}^i = -\partial_j \tilde{\gamma}^{ij}$, a strict criteria known as minimal distortion can be adopted that will minimise that change in volume elements during evolution. This was was first suggested by Dirac [45, 46], and is given by

$$\partial_t \partial_j \tilde{\gamma}^{ij} = 0\,. \tag{1.50}$$

In BSSN this is equivalent to $-\partial_t \tilde{\Gamma}^i = \tilde{\Gamma}^i = 0$ and is sometimes also referred to as "Gamma freezing". Enforcing this condition would lead to a set of coupled elliptical partial differential equations that are difficult to solve in 3D. As such, an alternative approach known as the Gamma driver condition [47] attempts to drive $\tilde{\Gamma}^i$ to 0 is given by

$$\partial_t \beta^i = \eta_1 B^i\,, \quad \partial_t B^i = \eta_2 \alpha^{\eta_3} \partial_t \tilde{\Gamma}^i - \eta_4 B^i\,, \tag{1.51}$$

where η_n are constants that are tuned to the scenario which you are trying to solve. Combing this condition with Eqn. (1.38), is known as the moving puncture gauge [43, 48], and allows one to achieve long term stability of black hole spacetimes[11].

In the work that follows, the technical knowledge presented throughout this section will be used, however the specific equations and gauge conditions used will be presented in Sec. 1.4. However, before this, in the next section we will provide some technical knowledge into cosmology, dark matter, and axions, which are the subject of some of the simulations in this thesis.

1.3 Cosmology, dark matter and axion stars.

From as early as 100,000 years ago, when cosmology was considered to be any daily experience outside of the norm[12], a period known as "Magic Cosmology" [50], through the rise of the awareness of the cosmological order in the Neolithic era [51], and subsequent continuation of the study of cosmology into the modern day, the urge to understand the world and universe around us has been a driving force of humanity. In this section, we will give the reader an understanding of modern cosmology, which naturally leads into a discussion on dark matter (DM). After commenting on different DM candidates, we focus on talking about the axion; specifically on the strong CP problem in which it is motivated, the origin of the axion, and how axions can be produced cosmologically. We finish the section by talking about axion stars, which if their corresponding GWs are detected, could provide direct evidence for dark

[11] The evolution of a black hole in this gauge is sometimes referred to as the "trumpet" solution [49].

[12] Examples of things considered to be outside of one's daily experience include: extreme weather, earthquakes and sharp changes in the environment.

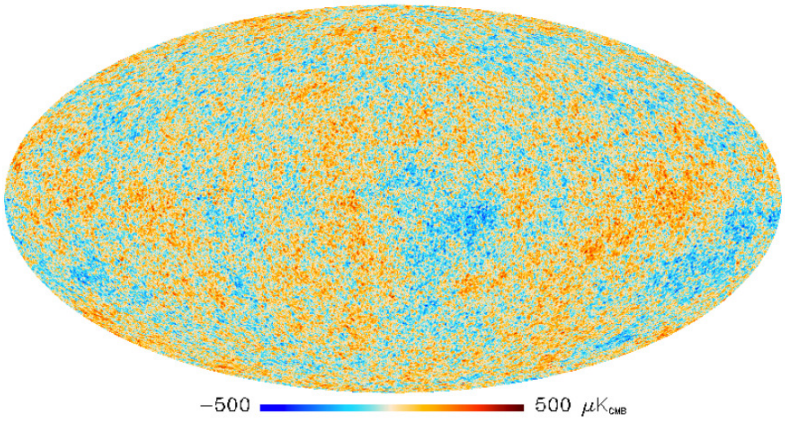

Figure 1.5: The Cosmic Microwave Background (CMB) as seen by the Planck mission. The CMB is radiation which accurately takes on the form of a black body with temperature, $T_0 = 2.725 \pm 0.001$ Kelvin [52, [p.75]. The CMB was produced at the surface of last scattering and gives a good representation of the structure of the universe at large scales. Small temperature fluctuations provide the seeds of structure formation in the universe. Image from [53]

matter.

1.3.1 The standard Cosmological model

The cornerstone of modern cosmology is that at the largest length scales, the universe is isotropic and homogeneous [16, p.319]. This cornerstone is known as the Cosmological Principle, and can be seen when one examines the cosmic microwave background (CMB), see Fig. 1.5. Our universe expanded from a dense hot beginning, *The Big Bang* (BB), and today, the universe is still expanding, as observationally confirmed by Lemaitre in 1927 [54] and Hubble in 1929 [55]. We call this model of the universe the "Hot Big Bang" model, and as such, we write the *metric of the universe* as

$$ds^2 = -dt^2 + a^2(t)\left(\frac{dr^2}{1-kr^2} + r^2 d\theta^2 + r^2 \sin^2(\theta) d\phi^2\right), \tag{1.52}$$

where $a(t)$ is the scale factor of the universe and k represents the curvature of the universe. This ansatz of the universe is known as the Friedmann-Lemaître-Robertson-Walker (FLRW)[13] metric, and can be used to solve the EFEs. We can modify the EFEs such that

$$G_{\mu\nu} + \Lambda g_{\mu\nu} = M_{pl}^{-2} T_{\mu\nu}\,, \tag{1.53}$$

[13]In the literature this is often referred to as both the Robertson-Walker (RW) and the Friedmann-Robertson-Walker (FRW) metric, although here we will refer to it as the FLRW metric.

where Λ is the cosmological constant. This term was originally introduced by Einstein to model the universe as being static, although now it serves a different purpose, which we will explain later. As the universe is isotropic and homogeneous, a reasonable approximation for it's energy-momentum (EM) tensor is that of a perfect fluid, such that

$$T^{\mu\nu} = (\rho + P)U^{\mu}U^{\nu} + Pg^{\mu\nu}\,, \tag{1.54}$$

where P is the pressure and ρ is the energy density of the fluid, and U^{μ} is the 4-velocity of the fluid with respect to the comoving frame. Using this EM tensor, as well as FLRW metric, we can solve the modified EFEs, Eqn. (1.53), such that

$$\left(\frac{\dot{a}}{a}\right)^2 = \frac{8\pi G}{3}\rho - \frac{k}{a^2} + \frac{1}{3}\Lambda\,, \tag{1.55}$$

$$\frac{\ddot{a}}{a} = -\frac{4\pi G}{3}(\rho + 3P) + \frac{1}{3}\Lambda\,, \tag{1.56}$$

where $\dot{a} = \partial_t a$, and where we define Eqn. (1.55) as the Friedmann equation and Eqn. (1.56) as the acceleration equation. By considering energy conservation, i.e $\nabla_{\mu}T^{\mu\nu} = 0$, we can show that the continuity equation is

$$\dot{\rho} = -3\left(\frac{\dot{a}}{a}\right)(\rho + P)\ . \tag{1.57}$$

Our universe contains many constituents components, and as such, we can obtain the scaling of the energy density for different classes of matter, by using the equation of state

$$P = \omega_i \rho\,, \tag{1.58}$$

where ω_i is some constant that depends on the class of matter. Using the equation of state, we can then solve the continuity equation, such that

$$\rho \propto a^{-3(1+\omega_i)}\,. \tag{1.59}$$

The cosmological constant is often referred to as dark energy[14], and currently dominates the universe, representing 69% of the total energy density. It can be described as the energy density of empty space, and little is understood about it. One can then rewrite the energy density, ρ_{Λ}, of the cosmological constant as

$$\rho_{\Lambda} = \frac{\Lambda}{8\pi G}\,. \tag{1.60}$$

[14]As this thesis does not concern dark energy, this description is sufficient such that the reader can understand the methodology of solving the Friedmann equations and the motivation for dark matter. The interested reader can refer to [56] for more information on dark energy.

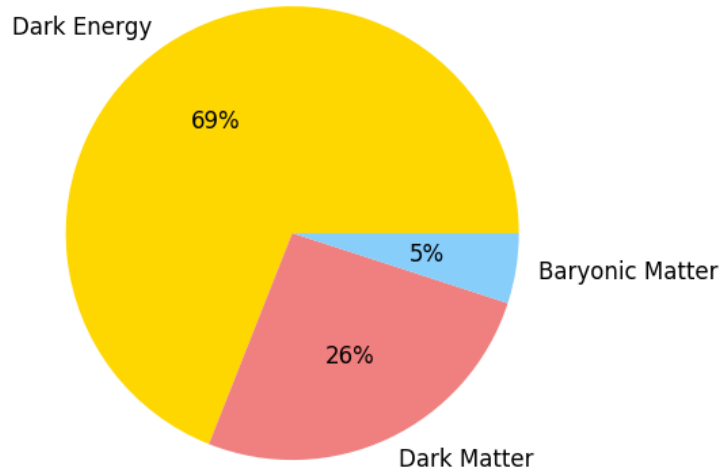

Figure 1.6: The constituent components of the universe. Notice that we only understand 5% of the known universe. Image generated from data provided in [57].

With the assumption that the cosmological constant, is indeed constant, and with the knowledge that the universe is currently expanding; and as dark energy dominates the universe, one can infer that dark energy has a negative equation of state; and with the further assumption that the universe is flat (which it is very close to being as per [57]), one can solve the Friedmann equations, and model the history of the universe, provided we know ω_i for each other matter class.

As stated before, the universe contains several constituent components, that as measured by the Planck collaboration [57], and in order of abundance are: dark energy (69%), dark matter (26%), baryonic matter (5%), and radiation (negligible). These abundances are illustrated in Fig. 1.6. We have already briefly described most of these components, however this thesis concerns itself with modelling dark matter in full GR, and as such, hopes to shed some light on the 26% of the universe that is unknown.

Before commenting on dark matter, and hence moving onto the next section, it should be noted that the BB model contains a number of problems, that one can address by having a period of inflation at the beginning of the universe. We refer the reader to [58] for a review of inflation. The BB model and this period of inflation together are collectively known as the standard cosmological model. For completeness, a diagram of the evolution of the universe is presented in Fig. 1.7.

1.3.2 Dark matter: evidence and candidates

There exists several pieces of evidence (see [60, 61] for a review) which indicate the existence of dark matter (DM). Often stated first, is that of Ford and Rubin's [62] discovery in the 1970's, and later evidence by Bosma [63] and Rubin et al [64],

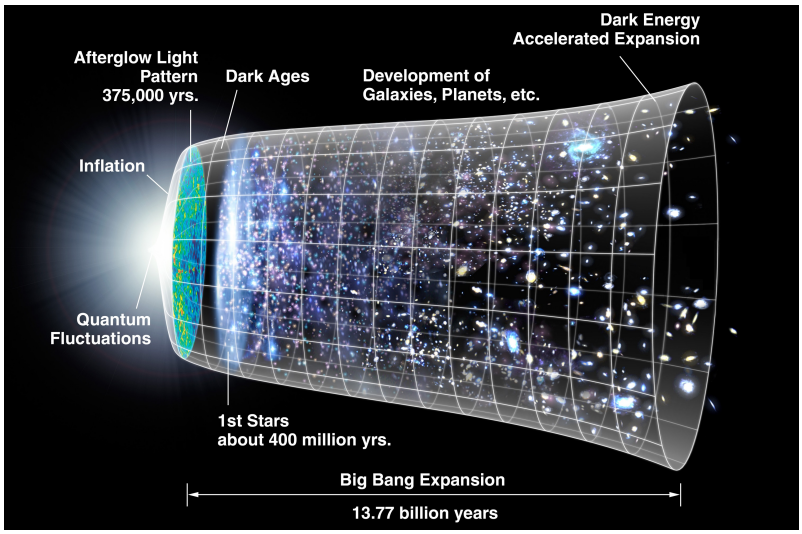

Figure 1.7: Here, the evolution of the universe is described from the beginning of the universe to today. It is thought that a big bang initiated the universe, with a period of inflation afterwards. Afterwards the universe evolved at large scales according to the Friedmann equations, with structure formation occurring at smaller scales. Image from [59].

that the rotation curves of galaxies are flat, rather than decreasing as a function of distance from the galactic centre as is expected. This implies that there must exist far more mass than can be explained by counting bright stellar objects, and that it could reside in massive dark halos around galaxies. One should note that this evidence is also sometimes used to justify a modified gravity approach as well, referred to as MOdified Newtonian Dynamics (MOND) [65], where DM does not exist, however we shall not elaborate on this further.

Gravitational lensing provides further evidence for the existence of DM; by using observations of bright, distant objects such as galaxies or quasars and by looking at the light from these objects that is *bent* via the existence of mass between the source and the observer, we can measure the amount of mass that cannot be seen aka, the DM. This is seen as sometimes multiple images of the same source, or images that are sheared or distorted. The Sloan Digital Sky Survey (SDSS) [66] provides one of the most comprehensive surveys which can be used to look at this effect, and has created 3-dimensional maps of more then 930,000 galaxies and 120,000 quasars.

Another piece of evidence is hot gas inside of clusters. Simply put, using x-ray emissions of hot gas within galaxy clusters (see [67] for an X-ray temperature map of the COMA cluster of galaxies which is often referred to when talking about this piece of evidence), one can calculate the amount of matter needed to form a potential well deep enough to stop the gas from escaping. The matter needed exceeds what can be observed, and can be explained by large amounts of dark matter within the galaxy.

There exists other pieces of evidence for the existence of DM including the bullet cluster [68], and the measurements from the CMB [57], however we hope that the evidence given serves sufficient motivation for its existence. There exists a number of potential candidates for DM:

- Primordial black holes (PBHs) - With the recent detections of gravitational waves from a black hole binary, there has been renewed interest in PBHs[15] [70–73] due to LIGO and Virgo being sensitive to ultra-compact black hole binaries. However, their are tight bounds on such objects [69, 74–78], and over the next several years, constraints from Advanced LIGO and Advanced Virgo are expected to improve by more then 2 orders of magnitude. Many of these bounds also place constraints of the abundance of massive compact halo objects (MACHOs) and ECOs.

- Weakly interacting massive particles (WIMPS) - Usually proposed as an extension to the standard model, and mediated by one of the Standard Model gauge interactions, these particles are experimentally favourable due to the scale of their interactions, and as such, one can probe them through a number of experiments including direct detection. See [79] for a review and for a summary of current constraints.

- Axions - Axions [80–93] where originally defined as the particle generated from the Peccei-Quinn (PQ) symmetry as a solution to the strong-CP problem in QCD, but now the concept has been extended to a class of objects known as axion-like particles (ALPs) with ultra-light masses [94]. See [95] for a review.

Although several models of dark matter are currently a possibility, within this thesis we choose the axion as the dark matter candidate for further investigation. In the following sections, we shall provide more details about axions, including further information about the motivation for them from QCD, the way in which they are produced cosmologically, and how we would model them in numerical relativity.

1.3.3 The strong CP problem and the axion

As stated in Sec. 1.3.2, axions where originally defined as the particle generated from the Peccei-Quinn (PQ) symmetry as a solution to the strong-CP problem in QCD. In the following we shall explain what the strong-CP problem is, and how the axion solves this. We will be following the presentation of the problem as per [95–98], and in particular, using the notation as per [95].

[15] See [69] for a review.

The strong-CP problem is due to the following term in the QCD Lagrangian:

$$\mathcal{L}_{\theta\text{QCD}} = \theta_{\text{QCD}} \frac{1}{32\pi^2} G\tilde{G}\,, \tag{1.61}$$

where G is the trace of the gluon field strength tensor, and $\tilde{G}$ is its dual. This term of the Lagrangian arises due to the $\theta-$vacua of QCD [95,99]. The phase term, θ_{QCD}, is CP violating, and gives rise to an electric dipole moment of the neutron (EDMN)

$$d_n \approx 3.6 \times 10^{-16} \theta_{\text{QCD}}\, e\,\text{cm}\,, \tag{1.62}$$

where e is the charge of an electron. The EDMN is constrained to $|d_n| < 2.9 \times 10^{-26}\, e\,\text{cm}$ [100] implying that $\theta_{\text{QCD}} \leq 10^{-10}$. The problem of why θ_{QCD} is extremely small is known as the strong-CP problem, especially since θ_{QCD} could obtain an $\mathcal{O}(1)$ [101] contribution from the observed CP-violation in the electroweak sector.

The QCD axion is the dynamical pseudoscalar field coupling to $G\tilde{G}$, proposed by Peccei and Quinn (PQ) [102], which dynamically sets $\theta_{\text{QCD}} = 0$ via QCD non-perturbative effects [103], and hence solves the strong-CP problem. Since there are several QCD axion models, including, but not limited to, the Peccei-Quinn-Weinberg-Welczeck (PQWW) [102,104,105], Kim-Shifman-Vainshtein-Zakharov (KSVZ) [106,107] and the Dine-Fischler-Srednicki-Zhitnitksy (DFSZ) [108,109], we will only sketch out how the problem is solved as per the description in [95].

The idea is that there exists an axion field, ϕ, that has some shift symmetry with only the derivatives of ϕ appearing in the action. One can take $\theta_{\text{QCD}} = \mathcal{C}\phi/f_a$, where f_a is the axion decay constant, and $\mathcal{C}$ is the colour anomaly. The colour anomaly is due to quantum effects violating classical symmetries, is an integer, and is often referred to as the domain wall number [95]. Within this thesis, we do not consider values which are not 1, and hence moving forwards we shall remove the term. There is a shift symmetry under $\phi \to \phi + c$, and as long as the shift symmetry violation is induced only by quantum effects, any contribution to θ_{QCD} can be absorbed in a shift of ϕ. The action only then depends on the field multiplying $G\tilde{G}$, then if the potential for the shifted field is minimised at $\phi/f_a = 0$, then the strong CP problem is solved.

The solving of the strong-CP problem is one of several motivations for the axion. As previously stated, the concept has been extended to a class of objects known as axion-like particles (ALPs) with ultra-light masses [94], and can be also be motivated in field theory and string theory. See [110, 111] for reviews. Within this thesis, we do not make any assumptions about the origin of the axion, and hence, we remain indifferent to the specific choice of theoretical motivation. Hence, we shall now discuss how the axion can be described in a model independent way, and how it is

produced cosmologically.

1.3.4 Axion cosmological production and scalar field dynamics

In what follows, we shall discuss the cosmological production mechanisms for the axion in a model independent way, and the relevant scalar field dynamics of the axion using the ADM metric that is used within this thesis.

Two important scales govern the production of the axion; a symmetry breaking scale, f_a, that we will refer to as the axion decay constant, which is a fundamental scale at which the PQ symmetry is broken; and $T_{SS} << f_a$, which is some temperature at which non-perturbative physics becomes relevant and provides a potential for the axion. The production mechanism is as follows:

We begin by considering the complex PQ-field, ψ, which has the potential

$$V(\psi) = \lambda_\psi \left(|\psi|^2 - \frac{f_a^2}{2} \right)^2 , \tag{1.63}$$

After PQ symmetry breaking, and writing the PQ field as $\psi = (\xi/\sqrt{2})e^{i\phi/f_a}$, the radial field, ξ, acquires a vacuum expectation value such that $\langle\psi\rangle = (f_a/\sqrt{2})e^{i\phi/f_a}$. The angular degree of freedom, the axion, ϕ, is a Goldstone boson of the broken symmetry. The axion has a shift symmetry, $\phi \to \phi + c$, as motivated in Sec. 1.3.3, however at some temperature, $T_{SS} << f_a$, and hence scale Λ_a, the shift symmetry is broken, and a potential for the axion is induced. This potential[16] is given by

$$V_a(\phi) = \Lambda_a^4 \left[1 - \cos\left(\frac{\phi}{f_a} \right) \right] \equiv m_a^2 f_a^2 \left[1 - \cos\left(\frac{\phi}{f_a} \right) \right] , \tag{1.64}$$

where $m_a = \Lambda_a^2/f_a$ is axion mass which is defined as the minimum of the potential when $\phi = 0$. Assuming that the symmetry breaking scale is small, the axion mass will also remain small, and due to the hierarchy of scales, the axion will be lighter than the radial field. This means that one can simulate the axion as a real valued scalar field with the axion potential just defined. Note that this potential has a discrete shift symmetry, $\phi \to \phi + 2\pi n/f_a$, where n is some integer.

In the limit of small angles, we can expand the axion potential in orders of (ϕ/f_a), and as such, we can approximate the axion potential, as a massive scalar

[16]The potential given here is not unique, and it cannot be without detailed knowledge of higher energy physics. However it is useful for studying axion self-interactions [95]. An example of another form of the potential is given in [112] where they use a form of construction $\cos^n \phi/f_a$.

field. Hence the potential is given by

$$V_O(\phi) = \frac{1}{2}m^2\phi^2\,, \tag{1.65}$$

where m is the scalar field mass, and we have omitted higher order terms. As within this thesis, we use potential V_O as an approximation for an axion potential, we can set $m = m_a$.

When the temperature reduces further such that $T < T_{SS}$ and the Hubble scale, H, is less than m_a, the axion field begins to oscillate around its potential minimum, and begins to behave like dark matter [113]. The dark matter then begins to cluster and forms structure in the universe. What happens next is then determined by the perturbations within the axion field, and that in turn depends on the scale at which PQ symmetry breaking occurred. If symmetry breaking occurs during inflation, then the axion field has small, almost scale-invariant isocurvature perturbations as well as dominant adiabatic curvature perturbations. If symmetry breaking occurs after inflation, then the adiabatic curvature perturbations are still present, but the isocurvature perturbations become $\mathcal{O}(1)$ over scales of order of the horizon size of symmetry breaking [114].

The two scales, f_a and m_a, can take a large range of values depending on what the chosen theory for the axion is. For the QCD axion, $\Lambda_a^4 \approx \Lambda_{\rm QCD}^3 m_u$ with $\Lambda_{\rm QCD}^3 \approx 200\,\text{MeV}$, with m_u being the up quark mass and the axion decay constant lies in the range $10^9\,\text{GeV} \leq f_a \leq 10^{17}\,\text{GeV}$. This implies that m_a is in the range $4\times10^{-10}\,\text{eV} \leq m_a \leq 4\times10^{-2}\,\text{eV}$. In string theory, f_a can take values near the GUT scale, $10^{16}\,\text{GeV}$, as well as at lower scales $10^{10-12}\,\text{GeV}$. In specific examples, one finds that $f_a \leq M_{pl}$, where M_{pl} is the Planck mass. For more information about these constraints, see [95].

To model the evolution of the axion field, with either potential, in full GR, we consider a single real minimally coupled scalar field, ϕ, with the following action

$$\mathscr{S}_\phi = \int d^4x\sqrt{-g}\left(\frac{1}{2}\nabla_\nu\phi\nabla^\nu\phi + V(\phi)\right)\,, \tag{1.66}$$

where $g = \det(g_{\mu\nu})$, and $V(\phi)$ is the potential of the scalar field. One can then obtain the Klein-Gordon equation in curved space

$$g^{\mu\nu}\nabla_\mu\nabla_\nu\phi = \frac{\mathrm{d}V}{\mathrm{d}\phi}\,, \tag{1.67}$$

where we remind the reader that $\nabla_\mu\phi = \partial_\mu\phi$. As we wish to model the scalar field numerically in full GR, using the ADM metric, Eqn. (1.18), we can decompose

Eqn. (1.67) into two first order equations using the variables ϕ and Π_M, such that

$$\Pi_M \equiv \frac{1}{\alpha}\left(\partial_t\phi - \beta^i\partial_i\phi\right) . \tag{1.68}$$

Using these variables, we define the evolution equations as

$$\partial_t\phi = \alpha\Pi_M + \beta^i\partial_i\phi\,, \tag{1.69}$$

$$\partial_t\Pi_M = \beta^i\partial_i\Pi_M + \alpha\partial_i\partial^i\phi + \partial_i\phi\partial^i\alpha + \alpha\left(K\Pi_M - \gamma^{ij}\Gamma^k_{ij}\partial_k\phi + \frac{dV}{d\phi}\right) , \tag{1.70}$$

where the Eqn. (1.69) is just a rearrangement of the definition of Π_M. We calculate the EM tensor for the scalar field as

$$T_{\mu\nu} = \nabla_\mu\phi\nabla_\nu\phi - \frac{1}{2}g_{\mu\nu}\left(\nabla_\zeta\phi\nabla^\zeta\phi + 2V\right) . \tag{1.71}$$

Combing the equations of motion, and the EM tensor, we now have all the information we need to evolve an axion field in full NR.

1.3.5 Axion stars

The equations of motions of a scalar field, defined in Eqn. (1.69) and Eqn. (1.70) whilst using the axion potential Eqn. (1.64), contain a solution for a quasi-stable, localised oscillating solution known as an axion star[17][18] [116]. These are related to a family of compact scalar field (pseudo)-solitons including Wheeler's "geons", boson stars, and oscillotons (OS) [117–121]. Here, we also define an OS as a massive scalar field with the potential defined in Eqn. (1.65). They provide a good approximation of an axion star where the leading order ϕ^4 interaction is negligible due to having a large axion decay constant, f_a, [114, 122, 123], as previously noted in Sec. 1.3.2. We refer the reader to Chap. 3 and Chap. 4 for more information about them, however for now one can think of them as a tool to model axion stars.

Solutions for spherically symmetric axion stars were first calculated numerically in [124], and where first studied using NR in [114]. It was found that three regions could be mapped onto an "axion stability diagram" (see Fig. 1.8), which were parametrised by the initial ADM mass of the star, M_{ADM}, and the axion decay constant f_a. These regions where defined as

1. Long-lived oscillating axion star solutions, with base frequency m_a, modulated by self-interactions

2. Collapse to a black hole

[17] See [115] for a review.

[18] In the literature these objects have also been referred to as Bose stars.

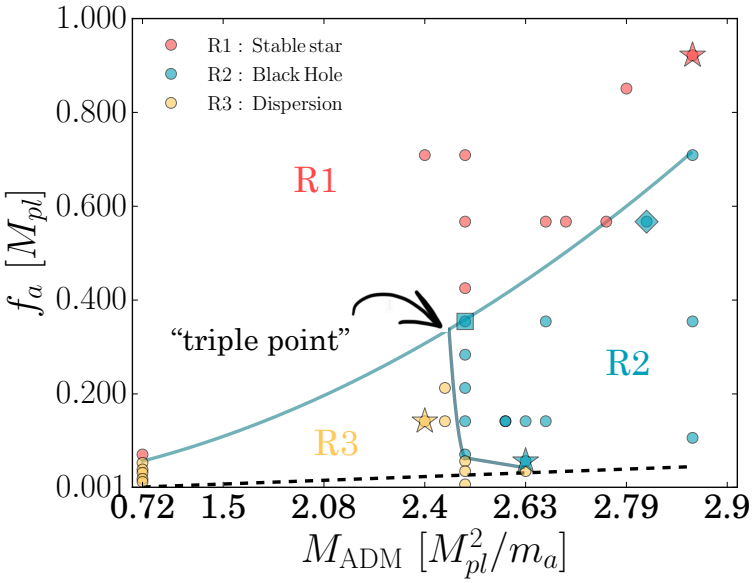

Figure 1.8: The "axion stability diagram" which shows 3 regions parametrised by the initial ADM mass of the star, M_{ADM}, and the axion decay constant f_a. These regions are: R1 - stable star, R2 - black hole collapse, and R3 - dispersion region. The dashed line indicates where the axion mass is negligible. Other symbols on the graph indicate [114] choose to explain these simulations in more depth. Image from [114].

3. Complete dispersal of the axion star via scalar radiation, sometimes referred to as an "axion star supernovae"

These boundaries intersect at an approximate triple point of approximately $(M_{TP}, f_{TP}) \approx (2.4\, M_{pl}^2/m_a, 0.3\, M_{pl})$. This triple point was later verified by [125] where they performed many numerical simulations in spherical symmetry, and commented that as one approaches the boundaries between regions, the line no longer "remains clean", and that there could exist special extra final states. We do not comment on these additional final states in this thesis due to the extreme cost of probing this region in full 3+1 NR. A similar stability diagram exists for OS, first studied in [126].

We do not assume all of the axions in the universe are contained with axion stars (see e.g. the compilations of PBH constraints in [69, 76, 77]). If these objects exist in our universe, there existence could be confirmed by the detection of gravitational waves from an axion star binary inspiral. This would be a smoking gun for the existence of axions, and would provide a clear direction for future research. Hence, with such a detection a possibility, within this thesis we will investigate some fundamental properties of axion stars, as well as make estimates for their gravitational wave emission. In [114], they also comment that for the case of ultralight axions, these objects could act as super-massive black hole seeds. This was also commented on in [127]. It is also thought that in axion stars could be the smallest DM structures

that can exist.

In Chap. 2 we study the formation of axion stars with high compactness, and with a toy model estimate the number densities and masses of axion stars. In Chap. 3 we study the head-on collisions of boosted equal mass OS for both the cases where the OS have equal phases or are maximally off-phase (anti-phase). In Chap. 4 we provide an in-depth explanation of the construction of initial data for a pair of boosted OS as well as the modifications needed during evolution, and comment on the potential for further study. All of these simulations were performed with GRChombo, and as such, in the following section we outline the code features of GRChombo.

1.4 GRChombo

There exists many Numerical General Relativity (NR) codes that have a variety of features. However, throughout this thesis, GRChombo was used to conduct numerical simulations. The aim of this section is to give the reader an overview of the key features of GRChombo, as well as specify the evolution and gauge conditions used within the code. For a more full discussion see [1, 128–130], and the GRChombo website at `http://grchombo.org`. The code is publicly available at `https://github.com/GRChombo`.

1.4.1 Numerical implementation

GRChombo is a multi-purpose NR code, which is built on top of the open source `Chombo` framework. `Chombo` is a set of tools developed by Lawrence Berkeley National Laboratory for implementing block-structured adaptive mesh refinement (AMR) in order to solve partial differential equations [131].

The key features of GRChombo are:

- *C++ class structure*: The code is written in the C++ language, which allows the use of the class structure to separate the various evolution and update processes.

- *Adaptive Mesh Refinement*: `Chombo` provides Berger-Oliger style [132, 133] AMR with Berger-Rigoutsos [134] block-structured grid generation. `Chombo` supports full non-trivial mesh topology. The user is required to specify regridding criteria, which is based on setting a maximum threshold for the gradient of a variable across a gridpoint. χ, K, and ρ are typically used as the variables.

- *MPI and OpenMP*: The use of MPI [135] and OpenMP [136], gives GRChombo the ability to scale efficiently to several thousand CPU-cores per run. `Chombo`

uses an inbuilt load-balancing algorithm, with Morton ordering to map grid responsibility to neighbouring processors in order to optimise processor number scaling.

- *Standardised Output and Visualisation*: `Chombo` uses the `HDF5` output format. The output files can then be used to restart the code, and due to the filetype, allow for easy analysis via both visualisation tools such as `VisIt` and post-processing tools such as YT [4].

- *BSSN formalism with moving puncture*: The EFEs are evolved using the BSSN formalism (see Sec. 1.2.6) with a scalar field being used as the matter source. The singularities of black holes are managed using the moving puncture gauge conditions [43, 48]. The evolution equations and gauge conditions are detailed in Sec. 1.4.2.

- *4th order discretisation in space and time*: GRChombo uses a Runge-Kutta 4th order (RK4) [137] time update and 4th order spatial stencils. In [1] it was shown that the convergence is approximately 4th order without regridding, but reduces to 3rd order convergence due to regridding effects.

- *Kreiss-Oliger dissipation:* Kreiss-Oliger dissipation [138] is used to control errors and a 4th Order method was implemented to ensure stability of the system.

- *Boundary conditions*: Both periodic and Sommerfeld boundary conditions [47] are implemented in GRChombo. Sommerfield boundary conditions allow outgoing waves to exit the grid with minimal reflections, however for most simulations, the AMR functionality allows one to set the boundaries far enough away such that reflections do not affect the results during simulation time.

- *Initial Conditions*: GRChombo does not solve the constraint equations for provided initial conditions, and thus as a user, one must provide appropriate initial data. However, GRChombo can be used to relax the Hamiltonian constraint for the value of χ where the other variables are assumed to solve the momentum constraint.

- *Diagnostics*: GRChombo permits the user to monitor the Hamiltonian and momentum constraint violation, as well to extract a variety of useful quantities such as gravitational waves.

GRChombo is constantly being updated by a team of dedicated developers, and as such, see `https://github.com/GRChombo` for the latest feature set.

1.4.2 Evolution equations and gauge conditions

GRChombo uses the BSSN formalism [40–42] to evolve the EFEs, with a scalar field as the matter source. The BSSN evolution equations are outlined in Sec. 1.2.6, and the scalar field matter evolution equations are outlined in Eqn. (1.69) and Eqn. (1.70).

GRChombo uses the puncture gauge [43, 48], which is a combination of the Bono-Masso type slicing condition [39] and the Gamma driver condition [47]. Hence, the evolution equations for the gauge conditions are

$$\partial_t \alpha = -\mu \alpha K + \beta^i \partial_i \alpha \,, \tag{1.72}$$

$$\partial_t \beta^i = B^i \,, \tag{1.73}$$

$$\partial_t B^i = \frac{3}{4} \partial_t \Gamma^i - \eta B^i \,, \tag{1.74}$$

where compared to Eqn. (1.38) and Eqn. (1.51), $\mu_1 = \mu$, $\eta_4 = \eta$, $\mu_2 = \mu_3 = \eta_3 = 0$, $\eta_1 = 1$, and $\eta_2 = \frac{3}{4}$. The constants η, of order $1/M_{ADM}$, and μ, of order 1, may be varied by the user to improve stability.

With GRChombo specified, this signals the end of the introductory chapter of this thesis. With the information provided, it is hoped that the reader has an understanding of the underlying technical details of the research described in this thesis. Any further introductory material required to understand a specific piece of research is provided at the beginning of the corresponding chapter.

Chapter 2

Formation of relativistic axion stars

"That's no moon... it's a space station." - In our case it's an Axion Star

---

Obi Wan Kenobi, Star Wars
Episode IV - A New Hope

This chapter is based on published work [2]. I would like to thank Thomas Helfer, David J. E. Marsh and Eugene Lim for their contributions towards this publication, and subsequently towards this chapter.

2.1 Introduction

The LIGO/Virgo collaboration has made historic measurements of gravitational waves (GW) from the binary coalescence of black holes (BH) [7–12] and neutron stars [13]. This paves the way for searches for signals from "exotic compact objects" (ECO; see e.g. [126, 139–144]). Axions and axion-like particles [80–93] (which we refer to collectively as simply "axions") can form such ECO, known as axion stars.

To have a strong GW signal in the LIGO/Virgo, the ECO must have mass and compactness,

$$\mathcal{C} \equiv \frac{GM_\star}{R}, \tag{2.1}$$

where $M_\star$ is the mass of the object, in a particular range [139]. Simulations have shown that there are known environments in dark matter halos in which non-relativistic axion stars form [145–149]. Any source of large (possibly primordial) density perturbations, or rapid merging and accretion could potentially grow such stars into the range of mass and compactness accessible to LIGO/Virgo, and even

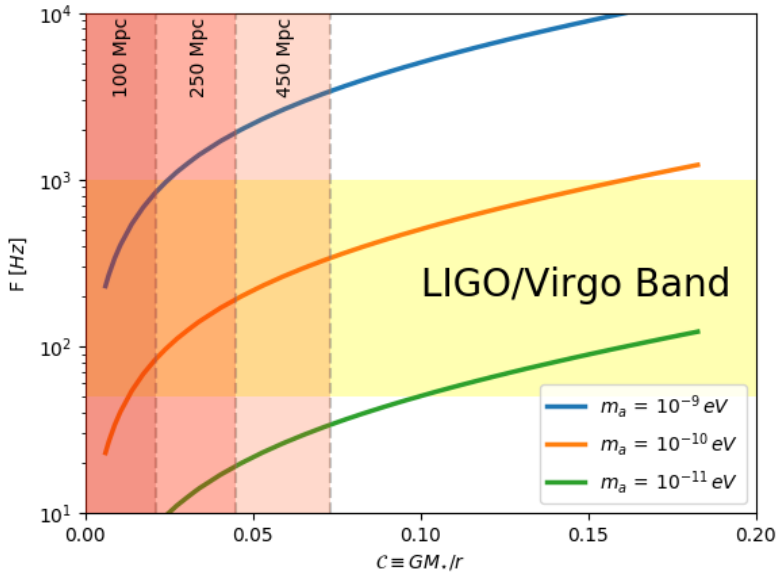

Figure 2.1: LIGO/Virgo frequency band for axion stars. The frequency is given by the ISCO frequency, Eqn. (2.6)). The compactness $\mathcal{C}(M)$ is for non-interacting oscillotons, which is a good description of stable axion stars. Assigning a luminosity distance to binaries, the minimum compactness is found from the results of [139]. Axion stars detectable by LIGO/Virgo must have $\mathcal{C} \gtrsim 0.02$ and axion mass $m_a \approx 10^{-10}$ eV.

beyond as they collapse to BH or disperse as novae [114]. However, there have not been simulations of the final stages of axion star formation in the full relativistic regime and beyond spherical symmetry, which are required to determine the fate of large axion densities.

In the following chapter we simulate the formation of compact axion stars and BH from some pseudo-random initial conditions using full (3+1) dimensional numerical relativity simulations with GRChombo [1]. Our results can be used to assess axion star formation given some input realisation of the axion density field. We demonstrate this for a toy model density field, using peak statistics to label compact axion stars and BH in the LIGO/Virgo frequency band.

We remain agnostic about the amount of dark matter (DM) that might be contained in compact axion stars, noting only that it must be relatively small, of order a few percent (see e.g. the compilations of primordial BH constraints in [69, 76, 77]). Given the theoretical uncertainties in formation mechanisms for compact axion stars from axion dark matter, such bounds can easily be consistent with all the dark matter being axions.

2.2 Gravitational waves from ECOs

In the following section, we review the description of GWs from ECOs given in [139]. An ECO is described by two parameters, the mass, $M_\star$, and the compactness, $\mathcal{C}$, which together determine the frequency and amplitude of GWs produced in a binary inspiral (the merger and ringdown phase contain more information requiring direct simulation). The orbital period, P, is related to the total binary mass, M_{tot} and semi-major axis, l, by Kepler's third law

$$P^2 = \frac{4\pi^2 l^3}{GM_{tot}}\,. \tag{2.2}$$

The frequency, f, of gravitational wave emission is twice[1] the orbital frequency, $\nu = 1/P$, and hence is given by

$$f = \sqrt{\frac{GM_{tot}}{\pi^2 l^3}}\,. \tag{2.3}$$

The innermost stable circular orbit, ISCO, determines the end of the inspiral phase, and the beginning of the merger phase. For a black hole binary, the ISCO is given by

$$R_{\rm BH}^{\rm ISCO} = 6GM_{tot}\,. \tag{2.4}$$

For an ECO, the ISCO is modified by the variable compactness:

$$R_{\rm ECO}^{\rm ISCO} = \frac{3GM_{tot}}{\mathcal{C}}\,. \tag{2.5}$$

Hence the typical frequency, $f_{\rm ECO}^{\rm ISCO}$, of two merging ECO is

$$f_{\rm ECO}^{\rm ISCO} = \frac{\mathcal{C}^{\frac{3}{2}}}{3^{\frac{3}{2}}\pi GM_{tot}}\,. \tag{2.6}$$

For black holes, the maximum frequency for gravitational wave emission at the end of the inspiral is given by numerical simulations of the waveform of BH mergers, and is defined as $f = (1+\Delta) f_{\rm BH}^{\rm ISCO}$. Δ is a correction term computed in post-Newtonian approximation [150], and is dependant of the mass ratio and spins of the black holes. In the parameter range where the post-Newtonian approximation is valid, it was found that $\Delta = \mathcal{O}(1)$, although we only expect this to hold for relatively compact objects with $\mathcal{C}$ within a factor of a few of BH. With this knowledge, for the discussion we deem it adequate to take Eqn. (2.6) as the typical frequency of gravitational wave emission.

[1] As both frequency, f, and orbital frequency, ν, contain factors of 2π we can cancel them for ease

The LIGO/Virgo noise-power spectral density is minimised between 50 Hz and 1000 Hz. Placing the frequency in Eqn. (2.6) in the LIGO/Virgo band gives the range of M and $\mathcal{C}$. For BH we find the benchmark mass for LIGO/Virgo of $M_\star \approx 10M_\odot$ stellar mass BH, while for LISA one finds sensitivity to supermassive BHs, $M_\star \approx 10^3 - 10^7 M_\odot$. [139] considered the signal to noise for ECO binary mergers in the LIGO/Virgo band, and found that for events within a given luminosity distance D_L there is a minimum value of $\mathcal{C}$ at any given mass to given an event with large signal to noise.

Fig. 2.1 shows the results of [139] for the minimum compactness for different luminosity distances together with the $\mathcal{C}(M)$ relation for axion stars determined from spherically symmetric numerical GR [114, 151]. Axion stars detectable by LIGO/Virgo must have $\mathcal{C} \gtrsim 0.02$ and axion mass $m_a \approx 10^{-10}$ eV, implying that the axion stars are of approximately solar mass.

2.3 Axion star formation

Axion stars giving rise to potential GW inspiral signals in LIGO/Virgo have high compactness, and are thus relativistic objects. If axion stars can reach such high compactness, they could also surpass their maximum stable mass, entering the unstable region in the "phase diagram" [114, 122, 125], either collapsing to a BH or dispersing in a nova, depending on the axion "decay constant", ${f_a}^2$.

2.3.1 Initial conditions

We consider an initial state of energy density in the axion field characterised by a single momentum scale, $k_\star$, in a superposition of waves in (x, y, z):

$$\phi = \varphi \left[\cos k_\star x + \cos k_\star y + \cos k_\star z\right] . \tag{2.7}$$

The waves have initially zero velocity, $\dot{\phi} = 0$. Choosing $k_\star = 2\pi/\tilde{L}$, where $\tilde{L}$ is the size of the computational domain, and imposing periodic boundary conditions, the superposition of waves results in 2 over-densities; one in the centre of the computational domain and one at *each corner*. Hence the initial condition is that of a superposition of waves that is not spherically symmetric, but possesses a 6-fold discrete permutation symmetry. This breaks spherical symmetry for the density peak, allowing us to investigate the effects of anisotropy while keeping the parameter space sufficiently small so that we can scan through them with available computational

[2] In general, we expect the value of $f_a < M_{pl}$, however this, and the related "weak gravity conjecture" is hotly debated with relation to axion inflation [114] See [110, 152–157] for more information

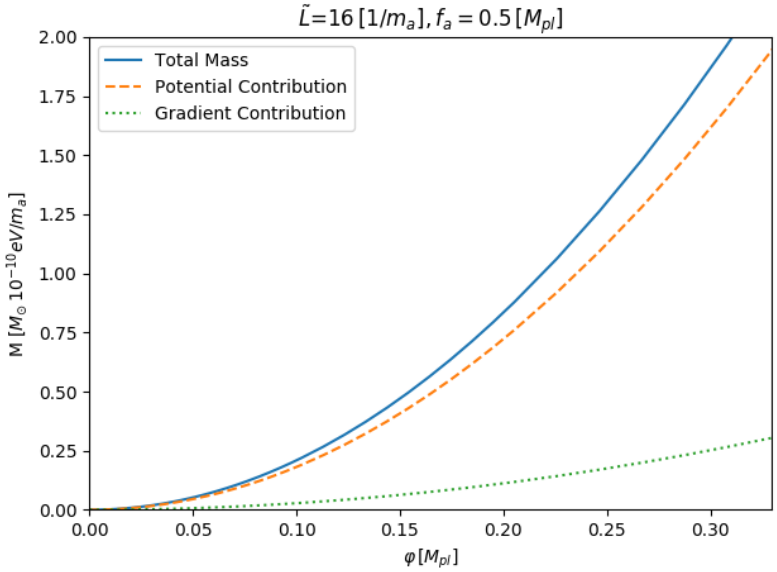

Figure 2.2: Using Eqn. (2.10) we calculate the total box mass, M, of our initial conditions for a box size of $\tilde{L} = 16\, m_a^{-1}$ and $f_a = 0.5\, M_{pl}$, as well as the contributions to M of the gradient term, $\frac{1}{2}(\partial_i \phi)^2$, and the potential term, $V(\phi)$. For the f_a simulated it can be seen that our initial mass is dominated by contributions from the potential term.

resources. This initial condition represents a locally overdense region dominated by the axion energy density, and hence is decoupled from the Hubble flow.

According to the results of [114] we expect collapse to be governed by two parameters: the total mass, M, in a single overdensity (this is half the total box mass due to there being two overdensities in the box), and the axion decay constant, f_a, defining a "phase diagram".[3] The total maximum mass in an overdensity is found by integrating the initial potential energy inside the box, and dividing by two (as we have two overdensities, and hence two objects will form due to symmetry):

$$\frac{1}{2}\int_V \rho \sqrt{\det \gamma_{ij}}\, dV\,, \tag{2.8}$$

with

$$\rho = n^\mu n^\nu T_{\mu\nu}\,, \tag{2.9}$$

where n^μ is the normal to the hypersurface and γ_{ij} the 3-D spatial metric. Assuming that the metric is conformally flat as our initial energy density has a small average

[3]This diagram has been explained by various arguments in Refs. [123, 158]. The phase boundaries have been accurately determined using spherically symmetric simulations by [125]. See also the simulations of [122] who study the regime of low f_a and low curvature leading to axion emission.

density, then using Eqn. (2.22)

$$M = \frac{1}{2}\int_{-L/2}^{L/2} \mathrm{d}x\ \mathrm{d}y\ \mathrm{d}z \left(\frac{1}{2}(\partial_i\phi)^2 + V(\phi)\right) , \tag{2.10}$$

where $L \equiv 2\pi/k_*$ is the physical size of the periodic domain. The axion potential energy is given by

$$V(\phi) = m_a^2 f_a^2 \left[1 - \cos\left(\frac{\phi}{f_a}\right)\right] . \tag{2.11}$$

By a choice of units, the axion mass m_a can be scaled out of all our simulations; units can be easily restored to set the physical mass of the compact objects formed. To achieve this scaling, we chose

$$M = 0.27\tilde{M}\left(\frac{10^{-10}\ \mathrm{eV}}{m_a}\right) M_\odot \tag{2.12}$$

where $M_\odot$ is the solar mass. Meanwhile, for small $\tilde{L} < (\varphi/f_a)$ the gradient term dominates. Fig. 2.2 shows the initial conditions for the smallest $\tilde{L}$ we simulated and for $f_a = 0.5\, M_{pl}$. All of our numerical simulations had initial conditions where potential energy dominated.

Finally, we can compute the average energy density of the simulation domain via

$$\bar{\rho} = \frac{M}{L^3} , \tag{2.13}$$

and hence the "local" Hubble constant $H^2_{\mathrm{local}} = (1/3M_{pl}^2)\bar{\rho}$ which is $H_{\mathrm{local}} \sim m_a$. We emphasise that this is not related to the "global" Hubble constant, since we are simulating a local overdense region.

Our simulations begin at an arbitrary dimensionless time, and we should ask how this is related to the cosmic time. In our simulations, we are evolving an axion dominated overdense local patch that is much smaller than the current Hubble radius, thus it is assumed that the expansion of the Universe and the presence of any fluctuation in energy density of non-axion components can be neglected. Thus, a fluctuation of any amplitude in our simulations will collapse, and cosmologically we cannot relate this to the collapse threshold for a given redshift.

A perturbation mode of *co-moving* wave number k with frequency $\omega^2(a) = (k/a)^2 + m_a^2$ will begin to evolve when $\omega(a) > H(a)$. Consider a co-moving mode k_{cm} which re-enters the horizon at time a_{ret}, $k_{\mathrm{cm}} = a_{\mathrm{ret}}H(a_{\mathrm{ret}})$. Furthermore, if $H(a_{\mathrm{ret}}) < m_a$, then the mode will collapse only at time $a_{\mathrm{osc}} > a_{\mathrm{ret}}$ where $H(a_{\mathrm{osc}}) \approx m_a$, i.e. when the mode is subhorizon. In our simulations, our box size is set to $\tilde{L} = 2\pi m_a/k_\star$ where $k_\star$ is a *physical scale* and related to the co-moving wave vector k_{cm} by an arbitrary scale factor a.

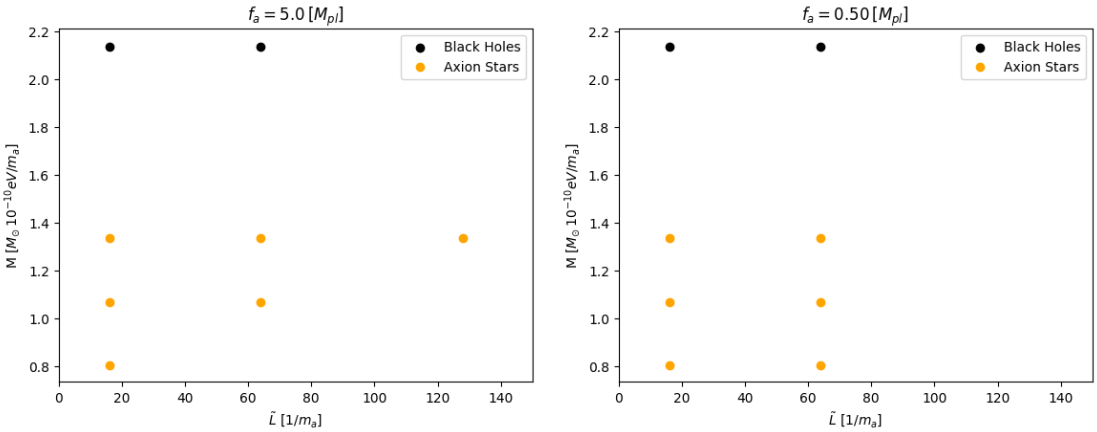

Figure 2.3: These plots are a summary of all numerical simulations performed. Black circles indicate that black holes where formed from the initial conditions and yellow circles indicate that axion stars were formed. We emphasise that the y-axis labels the *initial total mass* of the simulation initial conditions, not the final mass of the formed objects. No dispersion cases were obtained, and the reason for this is outlined in Sec. 2.3.9. The results presented here mirror that of [114,125], so when discussing the likely structure formation we will use the "phase diagram" constructed there.

From our choice of dimensionless units, this means that the physical length $k_\star^{-1} = (\tilde{L}/2\pi)m_a^{-1}$. As will be described in Sec. 2.3.2, we take $\tilde{L} = \mathcal{O}(16 \sim 128)$ in our simulations, and hence $k_\star < m_a$, which satisfies the condition above for subhorizon collapse.

2.3.2 Numerical simulations

We simulated collapse of a massive scalar field, ϕ, with an axion potential in numerical relativity, using GRChombo [1]. Details of the numerical scheme can be found in Sec. 1.4, with specific information to these simulations being provided in-situ. We probed a three dimensional "phase diagram", summarised in Fig. 2.3, to investigate how collapse differed whilst varying initial mass M, length scale of the axion waves $\tilde{L}$, and decay constant f_a. In the following sections we will explore the different types of structure that can be formed according to the parameters of the "phase diagram", as well as commenting on the technical limitations that we faced.

To explore the possible "phase diagram" of initial conditions for axion star collapse, we choose three length scales of the axion waves $\tilde{L} = 16, 64, 128\ m_a^{-1}$, two decay constants $f_a = 5.0, 0.5\ M_{pl}$ and four initial total box masses $M = 2.14, 1.34, 1.07, 0.80\ M_\odot\,(10^{-10}\text{eV}\ m_a^{-1})$. These initial conditions were chosen so that we can form a range of final structures; axion stars and black holes, like those found in [114, 125]. We fix our boundary conditions to be periodic.

2.3.3 Constructing initial data

We construct our initial data in the same was as in [159], however the key details of the method are reproduced here for convenience. We choose $\alpha = 1$ and $\beta_i = 0$ and hence on the initial hypersurface the initial gradient energy is

$$\rho_{grad} \equiv \frac{1}{2}\gamma^{ij}\partial_i\phi\partial_j\phi \tag{2.14}$$

We also introduce the notation for the kinetic term

$$\eta = \frac{1}{\alpha}\left(\partial_t\phi - \beta^k\right) \tag{2.15}$$

Which is zero on our initial hypersurface. Hence initially

$$\rho = \frac{1}{2}\gamma^{ij}\partial_i\phi\partial_j\phi + V \tag{2.16}$$

Our constraint equations become

$$\tilde{D}^2\chi - \frac{5}{4\chi}\tilde{\gamma}^{ij}\tilde{D}_i\chi\tilde{D}_j\chi + \frac{\chi\tilde{R}}{2} + \frac{K^2}{3} - \frac{1}{2}\tilde{A}_{ij}\tilde{A}^{ij} = 8\pi G\rho\,, \tag{2.17}$$

and

$$\tilde{D}_j\tilde{A}^{ij} - \frac{3}{2\chi}\tilde{A}^{ij}\tilde{D}_j\chi - \frac{2}{3}\tilde{\gamma}^{ij}\tilde{D}_jK = 8\pi G\eta\tilde{\gamma}^{ij}\partial_j\phi\,. \tag{2.18}$$

Next we want to specify the initial conditions for the metric γ_{ij} and the extrinsic curvature K_{ij}. We can make the simplifying assumption that the metric is conformally flat and the traceless part of the extrinsic curvature K_{ij} is zero everywhere on the initial hyperslice

$$\tilde{\gamma}_{ij} = \delta_{ij}\,, \tag{2.19}$$

and

$$\tilde{A}_{ij} = 0\,. \tag{2.20}$$

We now need to specify the values of K and χ on the initial hyperslice. Eqn. (2.18) is trivially satisfied for $K = const$, however, in order to satisfy Eqn. (2.17), and the periodic boundary conditions or χ, $K^2/24\pi$ needs to lie close to the average initial energy density for the hypersurface. Therefore for simplicity we choose it equal to the average initial energy density, approximating the metric to be Euclidean

$$K = -\sqrt{24\pi G\langle\rho\rangle}\,, \tag{2.21}$$

with

$$\rho = \frac{1}{2}(\partial_i\phi)^2 + V(\phi)\,, \tag{2.22}$$

where $\langle X \rangle = \mathcal{V}^{-1} \int X \, d\mathcal{V}$ indicates the average over the spatial volume $\mathcal{V}$ of the quantity X. Once K is chosen, the initial field profile and the Hamiltonian constraint then fully determine the conformal factor χ. The conformal factor, χ, was calculated using a relaxation procedure until we reached a relative Hamiltonian constraint violation, $\mathcal{H}$

$$\mathcal{H} \equiv \frac{H_{center}}{16\pi G \rho_{center}}\,, \tag{2.23}$$

of $\mathcal{O}(0.1\%)$[4]. The larger the length scale of the axion waves, the more numerically expensive the simulations were to perform due to an increase in the time scale of collapse, and a need for more refinement layers to track formation and the evolution of the resulting structure.

Black hole formation is identified using a spherical horizon finder and the formation of an axion star was identified using an "axion star location" script, detailed next.

2.3.4 Axion star location

To confirm the that a resulting object was an axion star, and to track its subsequent evolution, an "axion star finder" script was written, and ran in post-processing. The finder would look at the central density in the simulation, and locate the value and location of it's maximum, ρ_{max}. The radius in which the value of ρ had dropped to 5% of ρ_{max} was calculated, and then the total mass was defined as the integrated density within a sphere of that radius. The radius of the object was adjusted for expansion.

In Fig. 2.6, there are some points that can be considered to be outliers. When the script looks for the maximum value and location of ρ, if at that point in time there are two maximum points in the central region, it causes the script to not return the true radius of the object, and hence the calculated mass will also not be correct. This was not a frequent occurrence, and the cause of it is easily confirmed.

2.3.5 AMR condition

All simulations shared a coarsest grid of 64^3. Locally, the expansion of our spacetime is roughly

$$a \equiv \frac{1}{\sqrt{\chi}}. \tag{2.24}$$

Since the timescale of formation of objects varies, this means that the physical length scales of the problem do not necessarily track the grid, and hence requires a

[4]During the relaxation routine the value of H and ρ at the centre of the simulation was also the max value of those variables

rescale regridding threshold. We set our threshold to be triggered by high gradients in K and a scaled version of the gradients of ρ. These conditions track gravitational collapse in our simulations. For $\tilde{L} = 16$ we scaled our regridding of the gradients of ρ as

$$\rho_t \frac{\nabla \rho}{\sqrt{\chi}},$$

where ρ_t is a numerical regridding threshold set at the beginning of the simulation. It was set to a value of $20\rho^{star}_{max}$, where ρ^{star}_{max} is the maximum value of ρ that a star of half total box mass would have. If half the total box mass was greater then the most stable axion star, then ρ^{star}_{max} was set to be the for the highest stable axion star. For $\tilde{L} = 64$ and $\tilde{L} = 128$ we found that this condition was not enough for optimum regridding. Below an amount of layers (3 for 64, and 4 for 128), we added an additional regrid condition

$$\rho_a \frac{\nabla \rho}{\chi^{\frac{3}{2}}},$$

where ρ_a is an additional regridding threshold. ρ_a was chosen to be $10\rho^{box}_{max}$, where ρ^{box}_{max} is the maximum value of ρ in the simulation at $t = 0$. Once the correct thresholds where chosen, these regrid conditions would effectively follow the gravitational collapse in the simulations.

2.3.6 Convergence and stability

We use the following to measure the volume averaged Hamiltonian constraint violation:

$$L^2(H) = \sqrt{\frac{1}{V}\int_V |\mathcal{H}^2| dV}, \tag{2.25}$$

where V is the box volume with the interior of the apparent horizon excised. As can be seen in Fig. 2.4, we have good control over the constraint violation throughout the simulation.

We test the convergence of our simulations with the formation of an Axion Star with initial total mass of $M = 1.34\ M_\odot\, 10^{-10}\text{eV}\ m_a^{-1}$, $f_a = 5.0\ M_{pl}$ and $\tilde{L} = 16\ m_a^{-1}$. We use a fixed grid for the convergence test with resolutions of $0.25\ m_a^{-1}$, $0.125\ m_a^{-1}$ and $0.0625\ m_a^{-1}$. The results are shown in Fig. 2.5, where we obtain an order of convergence between 3rd and 4th order on average. The variation in the convergence test is due to the methodology, where we extract values of ϕ at the centre of the grid. ϕ passes through 0 during the evolution, that causes the spikes present in the convergence test.

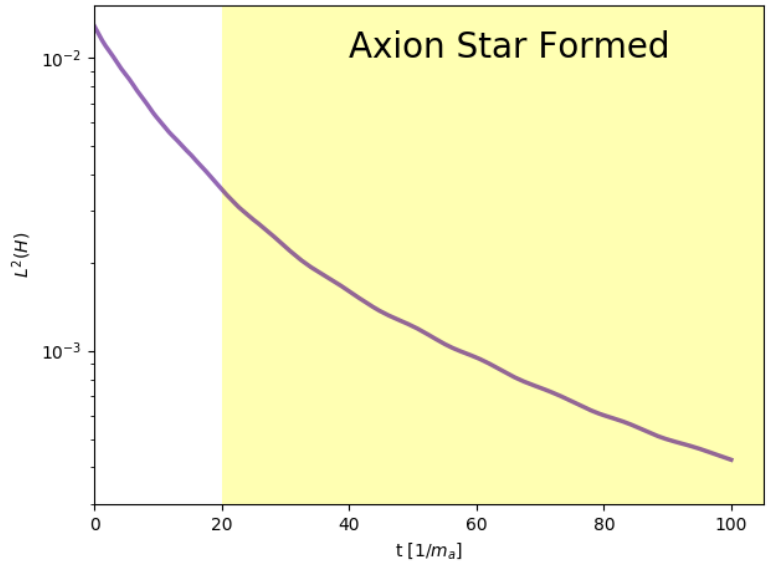

Figure 2.4: The plot shows the L^2 norm Eqn. (3.5) of the Hamiltonian constraint violation over time for a simulation that forms an axion star, with an initial total mass of $M = 1.34\ M_\odot\ 10^{-10}\text{eV}\ m_a^{-1}$, $f_a = 5.0\ M_{pl}$ and $\tilde{L} = 16\ m_a^{-1}$. The spikes in the plot are due to the regridding in the simulation and are rapidly damped.

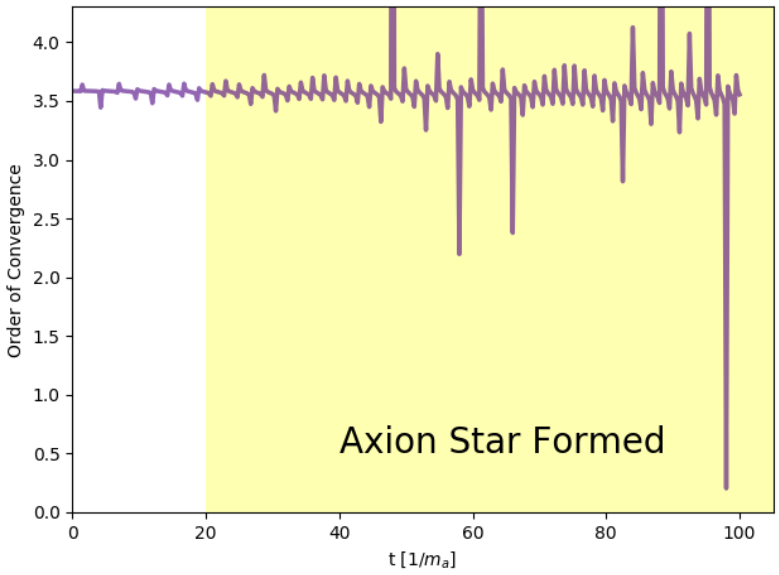

Figure 2.5: Convergence test for ϕ_{center} showing a convergence between 3rd and 4th order. The convergence test is done with a fixed grid with three different resolutions of 0.25 m_a^{-1}, 0.125 m_a^{-1} and 0.0625 m_a^{-1}. Our evolution scheme is 4th order and the variation in the convergence is due to ϕ passing through 0 during the evolution.

2.3.7 Axion star formation and evolution

Our simulations with initial conditions $M \leq 1.34\, M_\odot\, 10^{-10}\text{eV}\, m_a^{-1}$ resulted in axion star formation (see Fig. 2.3). To compute the mass, $M_\star$, of the axion stars, we use Eqn. (2.8), with the radius R computed to be such that $\rho(R) = 0.05\rho_{max}$ – this is a good approximation since we observed that the axion star sphericalises rapidly.

During the course of the evolution the axion stars were found to be stable (i.e. they do not disperse nor collapse into a BH), sphericalising rapidly leaving only a dominant radially perturbative mode[5] (see Fig. 2.6). Fig. 2.7 shows the variation of the radius of axion stars over time generated from spherically symmetric initial data [114,151]. The in the spherically symmetric case is long lived, and the computational cost of evolving the stars to their final end-state (presumably an unexcited star) is prohibitive. For $f_a = 5.0\, M_{pl}$ the radial variation presented in Fig. 2.6 is negligible for both masses shown. When lowering f_a to $0.5\, M_{pl}$ it can be seen that the more massive axion star collapses to a black hole, however for the less massive axion star a radial variation with a period of $300\, m_a^{-1}$ develops. The radial variation shown here has a longer period compared to the most massive case for $\tilde{L} = 16$, and shorter compared to $\tilde{L} = 64$. We conclude that the variation in radius of the stars from our formation process comes dominantly from decaying radially perturbative modes.

As has been shown in [126], ground state axion stars span a family parameterised by the compactness parameter $\mathcal{C}$. When studying the compactness of axion stars formed by our collapse process vs this family, it can be seen that these formed stars oscillate around this family, hence represents stable stars. This can be seen in Fig. 2.6.

Finally, we compute the efficiency of the axion star formation process, which is defined as

$$\text{Efficiency} \equiv \frac{\text{Total Initial Mass}}{\text{Mass captured in AS}}\,. \tag{2.26}$$

This is measured to range from 0.5 for $\tilde{L} = 128$ to 0.8 for $\tilde{L} = 16$. In other words, a large fraction of the initial mass forms the axion star. Since our simulation domain is periodic, and hence "free scalar field energy" has no place to disperse, we might worry that this may be due to a significant reabsorption. We observed that the axion star formed in $\mathcal{O}(10)$ "box crossing" times and if reabsorption of the scalar field was big, we should see a modulation in ϕ at 10 times that frequency, which we do not. Hence we surmise that reabsorption is small and expect that while in a dispersive environment the efficiency will be lower, it will not be significantly lower.

[5]The author wants to emphasise that we are referring to a radially perturbative mode of the axion star.

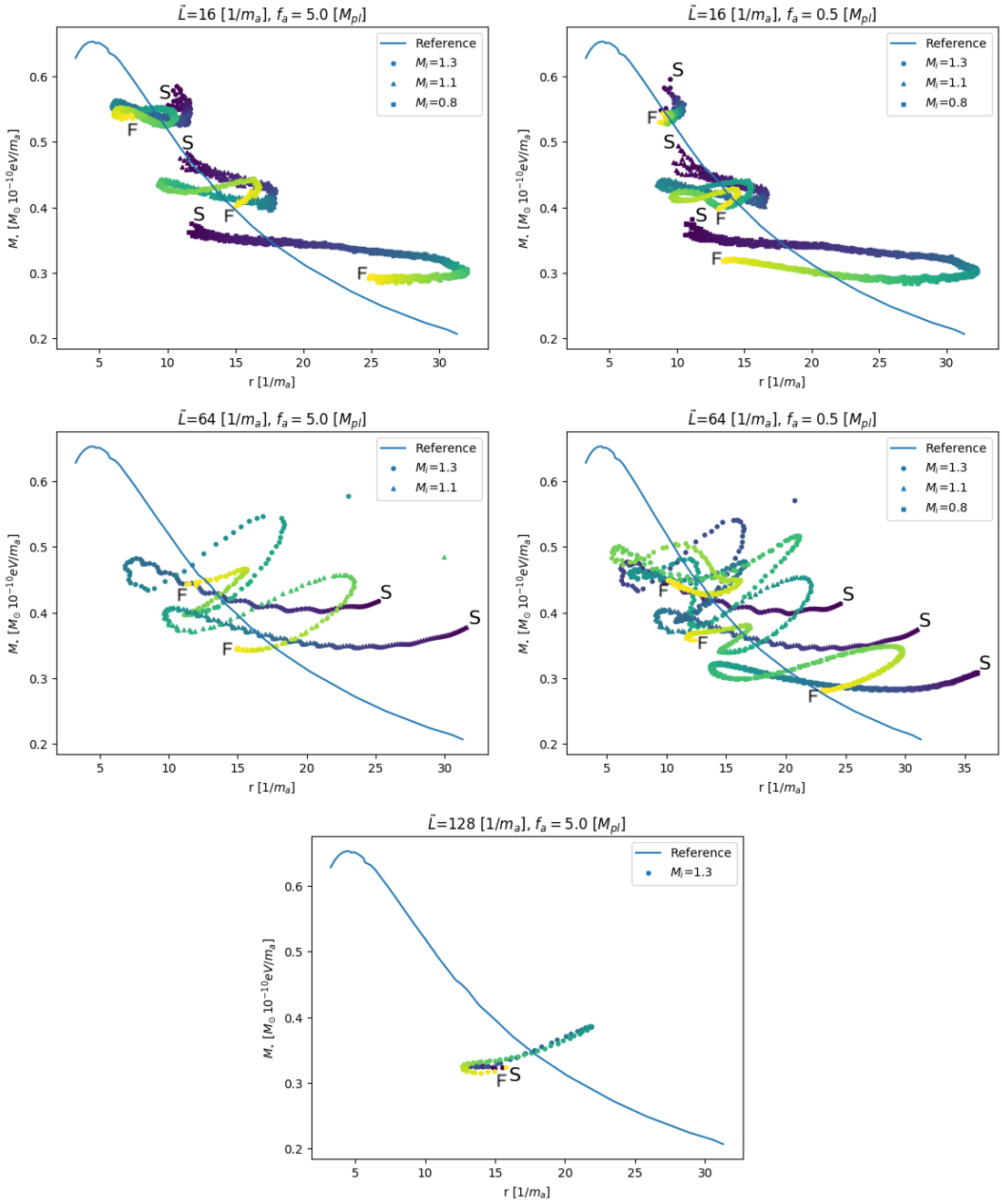

Figure 2.6: Evolution of the mass-radius relation of all simulations whose end state was identified as an axion star. The reference line in the plots is the mass radius relation for an unexcited axion star, and the points on top indicate the evolution of the observed star forming. The evolution in time of the mass-radius relation is indicated by the colour of the point, with the darkest points being the earliest in the evolution and the lightest points being the end of the evolution. Additionally the start point of the evolution is indicated by an 'S' and the end point with 'F'. The mass radius relation fluctuates significantly over time, varying in a decaying way around the unexcited star value. This process is attributed to the formed stars having radial perturbative modes. Outliers on these graphs are due to the axion star finder, outlined in Sec. 2.3.4

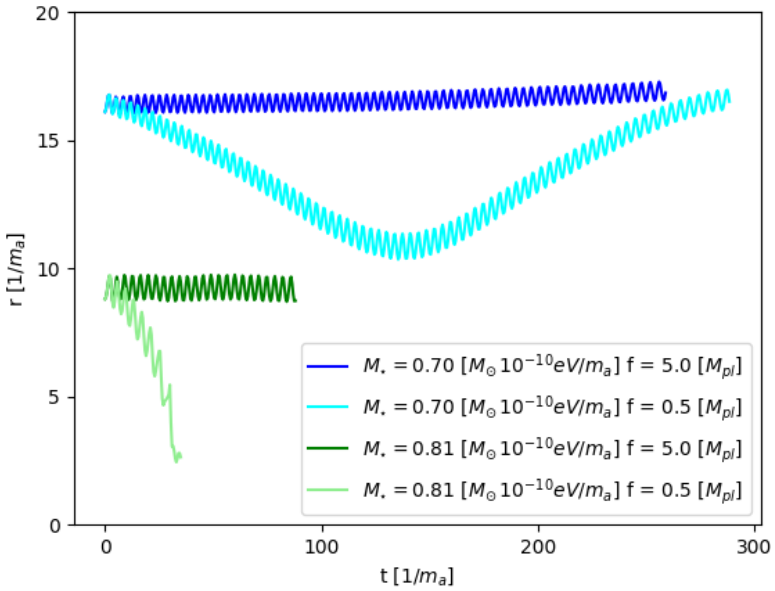

Figure 2.7: Variation of the axion star radius over time for spherically symmetric initial data [114, 151]. For $f_a = 5.0\, M_{pl}$ the radial variation is negligible for both masses shown. When lowering f_a to $0.5\, M_{pl}$ it can be seen that the more massive axion star collapses to a black hole, however for the less massive axion star a radial variation with a period of $300\, m_a^{-1}$ develops. The radial variation shown here has a longer period compared to the most massive case for $\tilde{L} = 16$, and shorter compared to $\tilde{L} = 64$.

2.3.8 Black hole formation

Meanwhile, our simulations show that initial conditions with $M = 2.14\, M_\odot\, 10^{-10}\text{eV}\, m_a^{-1}$ resulted in black hole formation (see Fig. 2.3). This is consistent with the "phase diagram" presented in [114, 125]. Similar to the axion star formation process, we found that the efficiency of black hole formation was $\mathcal{O}(1)$.

2.3.9 Dispersion regime

As shown in the phase diagram constructed in [114, 125], there exists "dispersal regions" where the axion star is not stable and disperses into scalar radiation. This occurs in regions with sufficiently low f_a and M. Due to the periodic domain, dispersed scalar fields will eventually fall back into a (possibly dispersing axion star), and hence we cannot probe this possibility. Instead we use the phase diagram constructed in [114, 125] for the analysis that follows.

2.4 Axion stars and gravitational waves

Relativistic axion stars with high compactness can emit sufficiently strong GW signals which makes them possible targets of gravitational wave detectors. In this

section, we will explore this possibility.

The phase diagram of [114] suggests that, for each value of f_a below the "triple point", $f_{\rm TP} \approx 0.2 M_{pl}$, there are three phases of axion star: low mass stars are stable; those above a first critical mass, $M_{\rm disp.}$ are unstable to emission of relativistic axion waves; those above a second critical mass, $M_{\rm BH}$, collapse to BHs. Above the triple point, the dispersal phase no longer exists, and compact objects form for all masses. Our numerical simulations have verified that this same picture applies to the "cosmological" initial conditions of Eqn. (2.7).

2.4.1 Cosmological formation of axion stars

Axion stars are the (quasi-)stable end point of gravitational collapse of the axion field, and in simulations of dark matter structure formation have been observed to form in diverse conditions [147–149]

Non-relativistic axions stars are observed to form in simulations with coherent initial conditions, where they condense via monolithic collapse as the first generation of axion DM halos, with a population expected to inhabit the centres of all halos [127, 147, 148]. These axion stars form from the small ($\zeta \approx 10^{-5}$) amplitude adiabatic curvature fluctuations which dominate the Universe on large scales, with the coherent initial conditions provided if Peccei-Quinn symmetry is broken during inflation. Cosmological simulations of this formation mechanism have only been performed for ultralight axions with $m_a \approx 10^{-22}$ eV. The corresponding axion stars in dwarf galaxies are too heavy to be relevant for LIGO/Virgo. The formation mechanism, however, is expected to be operative for all axion masses in all dark matter halos [160], potentially leading to relativistic cores in some region of parameter space.

Recently, axions stars were also shown to condense from highly incoherent initial conditions [149]. This mechanism is expected to be active in axion "miniclusters" [161–164], and indeed throughout any axion dark matter halo, potentially leading to spontaneous axion star formation. [149] proposes a growth rate that could make these axion stars reach relativistic masses if it does not quench. Mergers of such axion stars could also lead to mass increase.

Non-relativistic simulations like these provide realisations of the axion field with axion star locations. Dense peaks of this field will require individual relativistic simulations, and the evolution should resemble the cases that we have studied in the present work. In this model, the axion star population builds up over time in an astrophysical way, just as ordinary stars and BH do.

It is also possible that relativistic axion stars could form directly in the early Universe from large amplitude primordial fluctuations, a possibility we discuss in

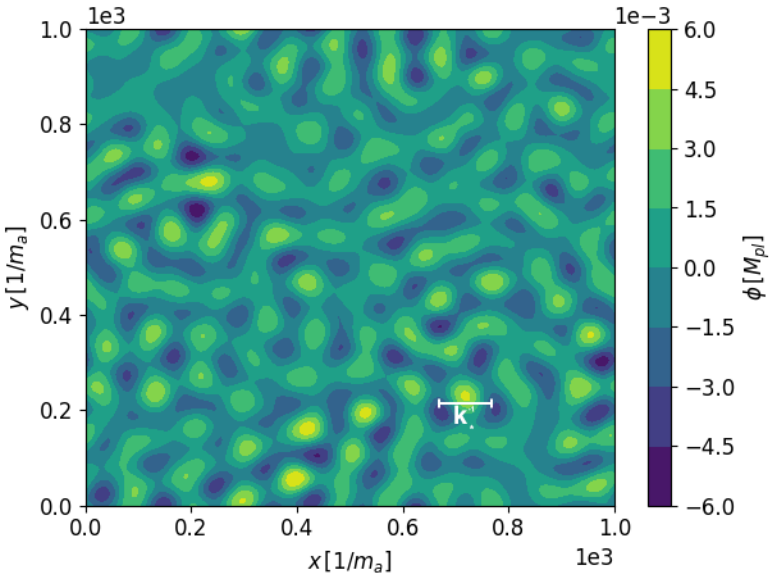

Figure 2.8: A toy model realisation of the axion density field that can be filtered to locate candidate compact axion stars.

more detail in Sec. 3.4. In this case also, dense peaks of the axion field will evolve to relativistic axion stars as studied above. In this model, the axion star population resembles primordial BH.

2.4.2 Peak statistics

Simulating a cosmological volume of initial conditions for the axion field with numerical relativity is not feasible. Instead we consider our simulations as representing isolated peaks in the density field.

We consider a toy model for an axion density field containing large amplitude peaks that can be described by our numerical simulations. A simple mechanism to form massive, dense, primordial AS in the LIGO/Virgo band is to enhance the axion power spectrum by a Gaussian bump on small scales:

$$P_{\delta\phi} \equiv A \exp\left[\frac{-(k-k_\star)^2}{2\sigma_k^2}\right], \tag{2.27}$$

where A is the amplitude, $k_\star$ the central mode, and $\sigma_k \ll k_\star$ the width. The amplitude has units $M_{pl}^2 m_a^{-3}$. Fig. 2.8 shows the toy model for the axion density field with k_*^{-1} roughly equal to the size of a peak described by our numerical simulations. For any axion density field like this toy example (e.g. density field and axion star location inside a DM halo), we can calculate the mass distribution of axion stars and BH formed by the extreme peaks by analogy to the theory of critical collapse for BHs, and to the Press-Schechter theory of cosmological structure formation.

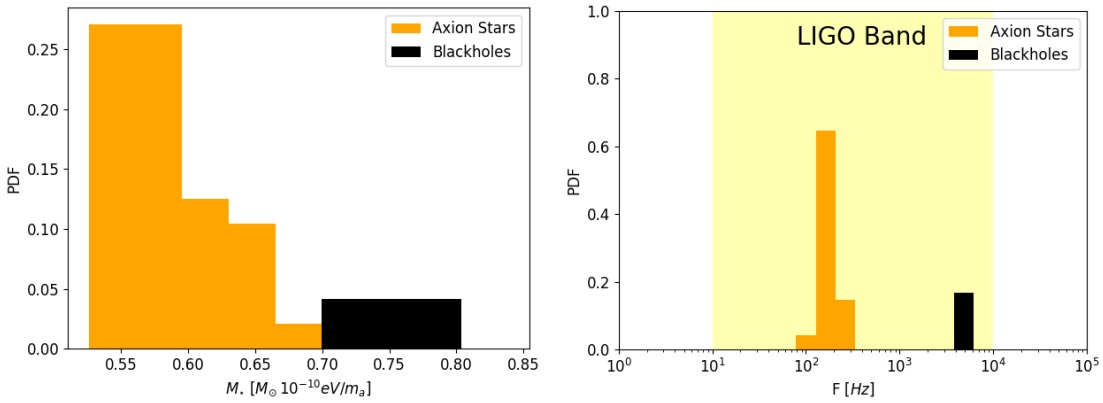

Figure 2.9: Left panel: Peaks of the toy model density field are assigned masses as axion stars and black holes according to the location on the phase diagram with $f_a = 0.5\ M_{pl}$. Right panel: Using Eqn. (2.6) and the $\mathcal{C}(M)$ relation for axion stars, we calculate the gravitational wave frequencies for axion star and BH equal mass binary mergers.

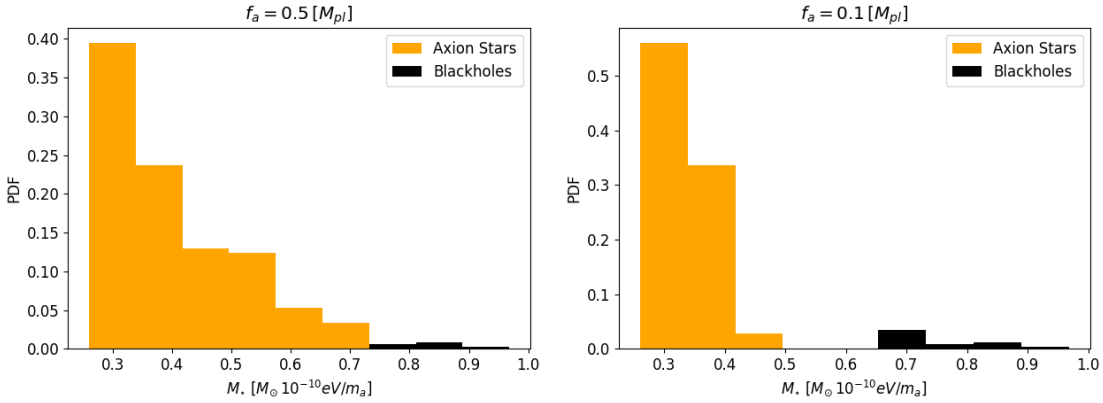

Figure 2.10: Peaks of the toy model density as Fig. 2.9 with $f_a = 0.5\ M_{pl}$ (left panel) and $f_a = 0.1\ M_{pl}$ (right panel). Note that as f_a dips below the triple point [114], a dispersal gap appears between the formation of black holes and axion stars.

The peak statistics are determined by thresholding the field, and are classified using a two pass connected component clustering algorithm, see Sec. 2.4.3. We partition the distribution for $\tilde{M}_\star(f_a)$ according to the critical masses $M_{\rm disp.}$ and $M_{\rm BH}$ in the phase diagram [114]. In our numerical simulations, due to the construction with periodic boundary conditions and an isolated fluctuation, fluctuations of all amplitudes leading to axion stars with radius smaller than the box size will eventually collapse under self-gravity. Thus we cannot determine the critical threshold for axion star collapse. However, we are only interested phenomenologically in the densest, and thus most massive stars, and so we threshold our field for a minimum compactness of the final axion star assuming that at least these most compact objects successfully collapse.

Fig. 2.9 and Fig. 2.10 apply such a thresholding and labelling to a statistically representative realisation of the toy model field of Fig. 2.8, taking only the one percent densest peaks. The labelled peaks span from axion stars, to a mix of axion stars and black holes, to primarily black holes depending on the field variance. Lowering f_a below $f_{\rm TP}$ results in the formation of a mass gap of objects. In particular, as f_a dips below the triple point at $f_{\rm TP} = 0.2M_{pl}$, a mass gap appears between the masses of formed axion stars and black holes. This mass gap is a characteristic feature of axion stars, hence the observation of a mass gap in the power spectrum of compact objects is a potential method of alluding to the existence of axions in the universe.

We can also estimate the frequency of gravitational waves emitted by an axion star-axion star or BH-BH binary merger using Eq. (2.6). Assuming binary mergers from the density field simply takes the field statistics as representative: no merger rate is calculated. Fig. 2.9 shows the frequencies with an axion mass of $m_a \approx 10^{-10}$eV. We observe that, for this distribution of peaks, axion star binary coalescence, as well as BH-BH binary coalescence from collapsed axion stars fall in the LIGO/Virgo band.

2.4.3 Two pass connected component labelling

The connected component labelling (CCL) procedure assigns a unique label to a set of connected target pixels in a binary image [165]. We can construct a binary image from an 2D array, in our case the energy density of the ϕ field generated by our toy power spectrum, by assigning a 0 to all elements in the array that are below a cutoff threshold, and a 1 to all those that are above. A subset of the binary image is called connected if for any two points P and Q of the subset there exists a sequence of points $P = P_0, P_1, P_2..., P_{n-1}, P_n = Q$ such that P_i is a neighbour of P_{i-1} [166]. The definition of a connection relies on that of a pixel's neighbourhood, if this includes 4 neighbours it is said to be 4-connected, and if it includes 8 neighbours it is said

to be 8-connected [167].

We use a specific group of CCL, known as two-pass algorithms, to label peaks. Two pass complete labelling in two scans: during the first scan they assign provisional labels to pixels and record label equivalencies. Label equivalencies are the resolved during or after the first scan. During the second scan, all equivalent labels are replaced by their representative label [168, 169]. We use a two-pass algorithm that use 4-connected to define a connection. Algorithmically, we did the following:

```
loop p
    if  p > 0 then
        if p above !=0 and p left =0 then
            pl = pl above
        else if  p above =0 and p left !=0 then
            pl = pl left
        else if  p above !=0 and p left !=0 then
            pl = min(pl above, pl left)
            record pl dependancy
        else
            pl = new label
```

where p is a pixel, pl is a pixel label, and min is a function that chooses the minimum of two values. The label equivalencies were then processed such that consecutive labels where generated, and then a second pass would the replace all equivalent labels. This algorithm provides a description of how the peaks where labelled. The Numpy [5] CCL algorithm was used for the analysis presented in this paper.

2.5 Discussion

It is an intriguing possibility that even if only a small fraction of the DM density is contained in axion stars and primordial BH, some GW events detectable by LIGO/Virgo might be due to primordial BH, and the distribution of GW events could be used to confirm this [170], and similarly, GW events and their distribution could confirm the existence of a fraction of DM in axion stars and BH formed from their collapse [171, 172].

Recent work with scalar compact objects head on mergers [140, 142, 151, 173] indicates distinctions in the gravitational wave signal with respect to black holes. If these distinctions also exist in binary coalescence (see [174–176] for boson star inspirals), a single GW event could be a smoking gun for the existence of axion stars. The end state mass spectrum from a number of such events could be used to determine the axion decay constant.

One possible mechanism to form compact axions stars in the early Universe is to enhance the axion power spectrum, $\langle \delta\phi(k)\delta\phi(k')\rangle$, on small scales, similarly to production methods for primordial black holes (see [177] and references therein). Such enhanced axion fluctuations on small scales arise generically in models of inflation in which the radial mode of the Peccei-Quinn field evolves as a spectator, leading to a strongly blue axion spectrum [178, 179].

Unfortunately, under standard cosmological assumptions such a power spectrum cannot form compact axion stars. A fluctuation in the axion field at early times is isocurvature (since the axions are subdominant compared to the radiation). During the radiation epoch, the linear transfer function of isocurvature overdensities is close to unity [180]. This implies that, between the time the axion field becomes non-relativistic, $H(a_{\rm osc}) \approx m_a$, and matter-radiation equality, $a_{\rm eq}$, the field fluctuation is redshifted as $\delta\phi \sim a^{-3/2}$. For the axion masses of interest, $m_a \approx 10^{-10}$ eV $\Rightarrow$ $a_{\rm osc}/a_{\rm eq} \approx 10^{-14}$, giving huge redshift factors.

Collapse of primordial fluctuations could occur during a putative early matter dominated phase [181, 182] (as expected in supersymmetric models, e.g. Refs. [183, 184]), or during reheating if the equation of state is in the correct regime. Study of collapse of axion stars during such a period, or from primordial curvature perturbations in the radiation era, requires additional simulations that account for the background fluid in addition to the axion scalar field. This interesting possibility, incorporating fluids into GRChombo, will be the subject of future study.

An axion star in the LIGO/Virgo band requires $m_a \approx 10^{-10}$ eV. The QCD axion with this mass has $f_a \approx 10^{16}$ GeV, which could possibly be detected directly by ABRACADABRA [185] or CASPEr [186]. However, with this low value of f_a axion stars cannot reach the required high compactness before becoming unstable. This leads to the interesting conclusion that any future observation of GWs from axion stars would imply the existence of contributions to the axion spectrum beyond QCD, and could thus lend support to the idea of a "String Axiverse" [94] or other non-standard axion scenarios [187].

Chapter 3

Black hole formation in relativistic oscilloton collisions

"Things are only impossible until they're not."

Jean-Luc Picard,
Star Trek: The Next Generation

This chapter is based off published work [3]. Details of the construction of the initial conditions, and modifications to the gauge conditions for the work that follows are given in Chap. 4. I would like to thank Thomas Helfer and Eugene Lim for their contributions towards this work.

3.1 Introduction

Self gravitating scalar field (pseudo)-solitons are known to have highly compact cores [121, 188, 189] and provide a family of candidates that can be defined as ECOs including Wheeler's "geons" [190, 191], boson stars [117], and oscillatons [117–121]. As previously stated in Sec. 1.3.5, these objects are closely related to a family of objects known as axion stars [2, 80–91, 93, 95, 114], in which further work has been done to understand ECOs.

Recent work with scalar compact objects head on mergers [140, 142, 151, 151, 173] as well as mixed mergers [192–194], indicates distinctions in the gravitational wave signal with respect to black holes. If these distinctions also exist in binary coalescence (see [174–176] for boson star inspirals), a single GW event could be a smoking gun for the existence of ECOs.

In this chapter, we study the relativistic head-on collisions of a class of real relativistic scalar fields solitons called oscillatons (OS) [121] using full (3+1) dimensional

numerical relativity simulations with GRChombo [1]. OS are stable on cosmological time scales [195] and could be realised as an axion star where the leading order ϕ^4 interaction are negligible due to having a high axion decay constant, f_a. Formation of such objects have been studied in both non-relativistic [196, 197] and relativistic cases [2] (see Chap. 2).

One of the key features of an OS is that it's scalar field configuration is not static. Instead it oscillates with the characteristic frequency $\omega \sim m$ where m is the effective mass of the field which is inversely related to the axion decay constant $m \propto 1/f_a$. Thus the interactions of any pair of OS will depend not only on their respective masses and the geometry of the interactions, but also on their *relative phase* $\Delta\theta$.

In the case of relativistic OS where gravity is strong, the OS can exhibit very high compactness on the order of tens of percent of the Schwarzschild radius. In this regime, it is expected that the linear regime is no longer valid, as gravity back-reacts strongly on the configuration of the scalar field. Indeed, at this regime, sufficiently compact OS can interact to form black holes. In [151], it was showed that the head-on collisions of such OS in this regime can produce gravitational wave signals that are distinct and more energetic than equivalent equal mass black hole mergers.

In this chapter, we extend the work of [151] into two different regimes. First, we consider the collisions of OS with different phases, in particular collisions in which their relative phase is maximal $\Delta\phi = \pi$, dubbed "anti-phase" OS collisions. We will show that anti-phase OS collisions experience a mutual repulsive force. Secondly, we consider the collisions of *boosted* OS, with relativistic initial center of mass frame velocities, for both equal phase and anti-phase pairs of OS. While at high initial velocities, black holes formed as expected from the hoop conjecture argument [173, 198, 199], surprisingly and counter-intuitively, we show that at low velocities, collisions are *less likely to form black holes* when compared to the equivalent configuration with zero initial velocity. This effect is seen in both equal and anti-phase cases, indicating the possible existence of a "critical point" (see Fig. 3.1).

3.2 Oscillotons

Consider a massive scalar field minimally coupled to gravity with the action

$$S = \int d^4x\sqrt{-g}\left[\frac{R}{16\pi G} - \frac{1}{2}\partial_\mu\phi\partial^\mu\phi - \frac{1}{2}m^2\phi^2\right] \tag{3.1}$$

where g is the determinant of the metric, R is the Ricci scalar and m is the mass of the real scalar field ϕ. Self-gravitating quasi-stable equilibrium configurations are known as oscillotons (OS) [121], and it has been shown in [126] that vacuum spherical symmetric solutions span a one-parameter family most conveniently represented by

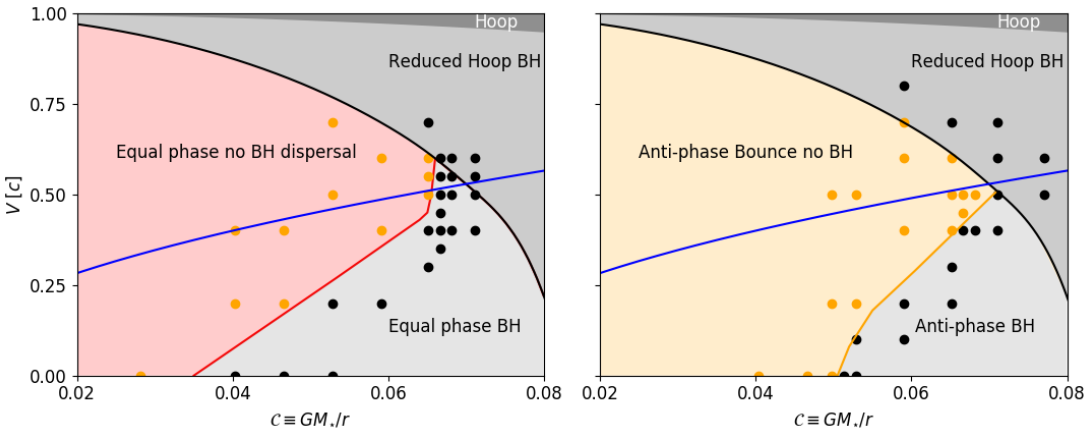

Figure 3.1: Final states of equal mass head-on OS-OS mergers as a function of compactness $\mathcal{C}$ and boost velocity v, for equal phase (left) and anti-phase cases (right). Shown are approximate regions indicating the final states of the collisions for the given initial conditions. The black line is the reduced hoop conjecture line Eqn. (3.4), while the red (equal phase) and orange (anti-phase) lines are numerically determined estimates where black holes do not form. In both cases, there exists a "stability band" between the black lines and the red/orange lines, in which the OS either disperse (equal phase) or bounce (anti-phase) post-collision. Comparing the free fall time and interaction times of the collision yields the blue line ($v \approx \mathcal{C}^{1/2}$), which converges with the reduced hoop conjecture line of $v \approx \sqrt{1-144\mathcal{C}^2}$ at $\mathcal{C} \approx 0.07$.

its compactness[1], $\mathcal{C}$, defined as

$$\mathcal{C} \equiv \frac{GM_*}{R} \tag{3.2}$$

where M_* is the total mass and R is the radius. Note that for a given $\mathcal{C}$ the radius $R(M_*)$ of unexcited OS is completely determined by its mass M_*. It has also been shown in [126] that low compactness OS with $\mathcal{C} < 0.14$ are stable and typically migrate to other stable $\mathcal{C} < 0.14$ when strongly radially perturbed. On the other hand, high compactness OS with $\mathcal{C} > 0.14$ are unstable, and under perturbations may either migrate to a stable lower mass OS with $\mathcal{C} < 0.14$ via scalar radiation or collapse into a black hole (see Fig. 3.2).

A key property of OS is that it oscillates along a characteristic frequency $\omega \sim m$, and thus interactions of OS depend on their relative phase difference $\Delta\theta$. In particular, the field configuration $\phi(x,t)$ of a head-on collision of equal phase $\Delta\theta = 0$ (anti-phase $\Delta\theta = \pi$) OS is *symmetric* (*anti-symmetric*) at the plane of collision parallel to the axis of motion. In between these two limits $0 < \Delta\theta < \pi$, the collisions are said to be "off-phase". Fig. 3.3 illustrates this further.

The special case for initially static, equal phase $\Delta\theta = 0$ head-on collisions of OS was investigated in [151]. There, it was showed that for equal phase $\Delta\theta = 0$ OS

[1]Note that this is the same definition given earlier in Eqn. (3.2), but we repeat it here for convenience.

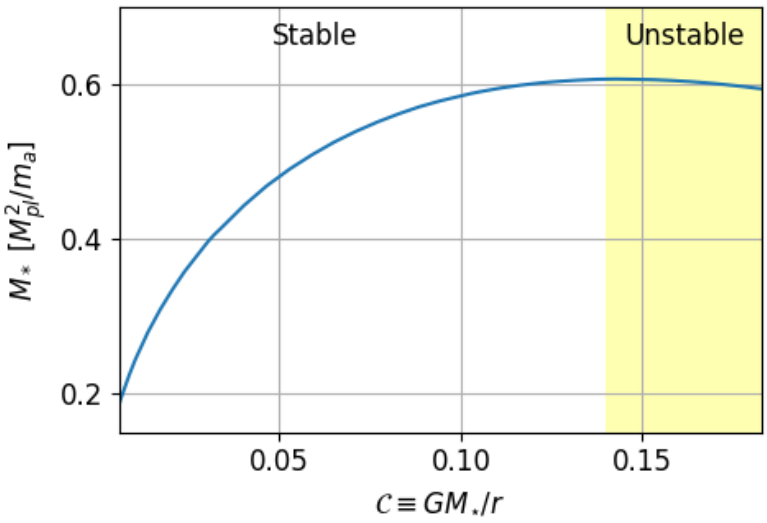

Figure 3.2: Spherically symmetric unperturbed OS solutions are spanned by a single parameter, here chosen to be the compactness $\mathcal{C} = GM_*/R$, as found in [126]. OS with $\mathcal{C} > 0.14$ are unstable to perturbations, with perturbations either dissipating leading to a final state of $\mathcal{C} < 0.14$ or collapsing into a black hole.

collisions, the end state of any such collision depends on the compactness $\mathcal{C}$. For $\mathcal{C} < 0.035$ ("subcritical" collisions), the collision results in an excited more massive oscillaton, while for $0.035 < \mathcal{C} < \mathcal{C}_*$ ("critical" collisions), the collision results in the formation of a black hole. For $\mathcal{C} > \mathcal{C}_*$ ("degenerate" collisions), since the OS are in the unstable branch (Fig. 3.2), mutual perturbations cause the OS to collapse into individual black holes before merging as a standard head on black hole collision.

In this chapter, we will study both equal phase and anti-phase boosted head-on OS collisions.

3.3 Boosted OS collisions

According to the hoop conjecture [200], a quantity of matter/energy E compressed into a spherical region such that a hoop of proper circumference $2\pi R$ completely encloses the matter in all directions, will form a black hole if the corresponding Schwarzschild radius, $R_s = 2GE$ is greater then R. The collisions of two solitons with individual rest mass M_* boosted to $\gamma = (1 - v^2)^{-1/2}$ will result in a system with an effective mass of $E = 2\gamma M_*$ in the center of mass frame. Applying the conjecture, if $R_s > R_0$ where R_0 is the rest frame radius of the soliton, then a black hole will form. Using Eqn. (3.2), we obtain the following condition for black hole formation

$$\gamma \geq \frac{1}{4\mathcal{C}} \ . \tag{3.3}$$

Such relativistic collisions of scalar solitons have been studied numerically before

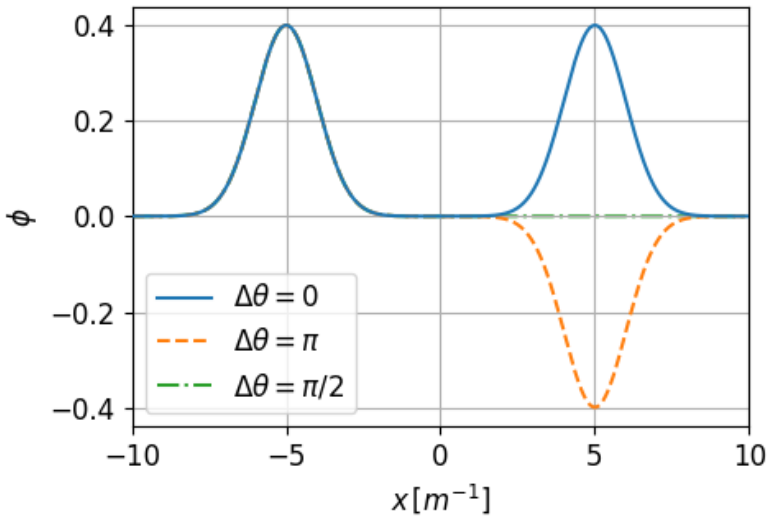

Figure 3.3: One dimensional plot of the ϕ profile along the axis of collision of two OS for three different phases shown at fixed t when the amplitude of ϕ for the left OS is maximised, with $x = 0$ being the point of collision. The symmetry and anti-symmetry of the equal phase pair of OS ($\Delta\theta = 0$) and an anti-phase pair of OS ($\Delta\theta = \pi$) respectively are constants of motion.

in the context of "boson stars[2]" of $\mathcal{C} = 0.025$ [173] and fluid packets of $\mathcal{C} = 0.0125$ [198]. In both cases, it was found that black hole formation occurs at the "reduced" hoop conjecture condition

$$\gamma \geq \gamma_h \equiv \frac{1}{12\mathcal{C}} \ , \tag{3.4}$$

which is roughly about 1/3 of what is predicted by the hoop conjecture. As we will soon see, we find this to be consistent with our simulations of relativistic OS collisions.

3.3.1 Numerical simulations

We simulated the collisions of two equal mass and hence equal $\mathcal{C}$ OS in numerical general relativity, using GRChombo [1] for both equal phase and anti-phase cases. Their initial separation are set at $d = 60m^{-1}$. We vary the initial velocities of the OS from $v = 0$ to $v = 0.8$ relative to the rest frame, with corresponding Lorentz factors $\gamma = 1$ to $\gamma = 1.4$ (see Chap. 4 for the details of the construction of initial data as well as the modifications needed for evolution – we note that it is important to construct the OS such that they are initially *unexcited*). In all cases except for $v = 0$, the initial velocities are sufficiently high that the OS are not initially bounded.

We track the OS position following [2] (see Sec. 2.3.4 for more details) by locating

[2]Boson stars are configurations of a complex scalar field with a $U(1)$ potential. In contrast with the real scalar field OS which are stabilized by field oscillations, boson stars are stabilized by their charges. For a review please see [201].

the value and location of maximum density $\rho_{\max}$, which we identify as its center. The velocity of the OS was calculated using OS position data across multiple timesteps. While the OS started out initially spherical, during the collision process the OS becomes an ellipsoid. The major and minor axes of the ellipsoid are then identified by the distance from the center to the point where the density is 5% of ρ_{center}. Black hole formation is identified with a horizon finder. The results of our simulations is presented in Fig. 3.1.

As before (see Eqn. (3.5)), we use the following to measure the volume averaged Hamiltonian constraint violation:

$$L^2(H) = \sqrt{\frac{1}{V}\int_V |\mathcal{H}^2| dV}, \tag{3.5}$$

where V is the box volume with the interior of the apparent horizon excised. The volume averaged Momentum constraint violation is calculated in a similar manner:

$$L^2(M) = \sqrt{\frac{1}{V}\int_V |\mathcal{M}^2| dV}, \tag{3.6}$$

We have good control over the constraint violation throughout our simulations, with a bouncing unboosted antisymmetric OS collision achieving a maximum value of $\mathcal{O}(10^{-6})$ at the beginning of the simulation and then decaying throughout the remainder of the simulation.

We test the convergence of our simulations by measuring the value of ρ along the collision axis of an unboosted antisymmetric OS pair with initial compactness of $\mathcal{C} = 0.028$, that results in a bounce. The spatial coordinates for the value to be measured at was chosen such that the OS passes through it before and after it bounces. We used fixed grid for the convergence test with resolutions of 1.0 m^{-1}, 0.5 m^{-1} and 0.25 m^{-1}. Fig. 3.4 shows the value of ρ for this test, and when calculated we obtain an order of convergence between 3rd and 4th order.

For the simulations presented we use a combination of fixed mesh and adaptive mesh refinement (AMR). A cuboid of fixed mesh of resolution 0.5 m^{-1} is constructed along the collision axis. We use AMR for blackhole formation that is triggered by a regridding threshold. We set our threshold, ρ_t, K_t, to be triggered by high gradients, ∇, in K and ρ;

$$\rho_t \nabla\rho + K_t \nabla K\,, \tag{3.7}$$

where ρ_t was set to be 20 times the maximum amplitude of the initial OS, ρ_{OS}^{max}, and K_t was set to a constant value.

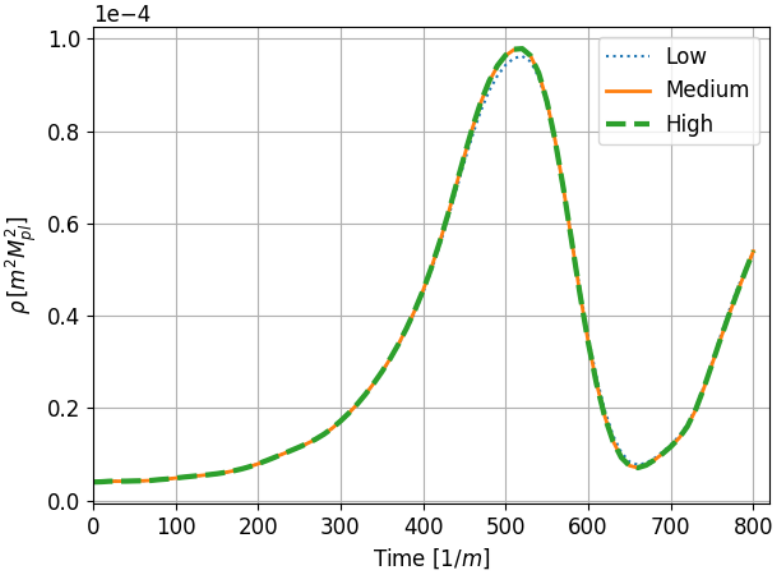

Figure 3.4: The value of ρ for a point along the collision axis of an antisymmetric OS pair that bounces. The test was done with fixed grid with three different resolutions of 1.0 m^{-1}, 0.5 m^{-1} and 0.25 m^{-1}. We obtain an order of convergence between 3rd and 4th order for this test.

3.3.2 Equal phase $\Delta\theta = 0$ collisions

For equal phase $\Delta\theta = 0$ case, at $v = 0$ we recover the result of [151] whereby black hole formation occured when $\mathcal{C} \geq 0.035$. At sufficiently high v, black holes form due to the additional energy imparted by the boost, as we expected. We found that they roughly obey the "reduced" hoop conjecture argument Eqn. (3.4) (as opposed to Eqn. (3.3)), providing another data point to add to those of [173, 198, 199].

However, at low v, intriguingly, black hole formation occurs only at *higher* compactness. For example, for $\mathcal{C} = 0.04$, black holes will form at $v = 0$ but will *not* form at $v > 0.2$ (until it meets the hoop conjecture line). In other words, *initial non-zero velocities hinder the formation of black holes.* The velocity required to prevent black hole formation increases with increasing $\mathcal{C}$, with the curve of transition sloping upwards until it meets the line defined by the "reduced" hoop conjecture argument Eqn. (3.4), at the "critical" point $\mathcal{C} \approx 0.068$ and $v \approx 0.55$. Beyond this point $\mathcal{C} > 0.068$, black holes form regardless of velocities. In Fig. 3.5, we show the black hole formation process of $\mathcal{C} = 0.065$ OS collisions for the $v = 0.7,\ 0.5,\ 0.3$ cases.

The existence of this "stability band" for non-black hole end states can be explained by the fact that higher collisional velocities imply a shorter collision timescale. Since the boosted OS are not energetic enough to form black holes from the hoop conjecture alone, they must interact during the collision to form a sufficiently deep gravitational potential well to generate infall for a collapse into a black

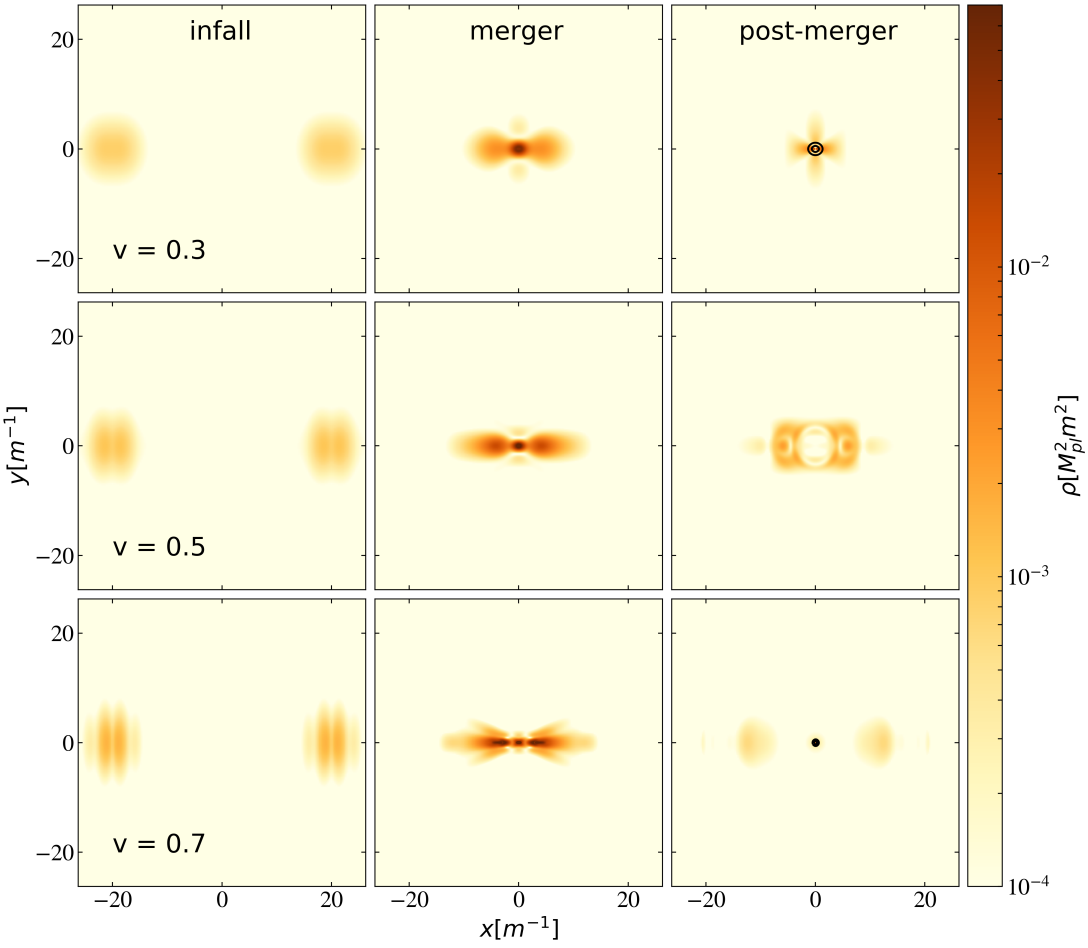

Figure 3.5: **In-phase $\Delta\theta = 0$ collisions :** Three different slices of energy density ρ with $\mathcal{C} = 0.065$ with $v = 0.3$, 0.5 , 0.7 from top to bottom. The slices for the (i) infall, (ii) merger and (iii) post-merger. Black holes form in the $v = 0.3$ (top) and $v = 0.7$ (bottom) cases, with black lines indicating curvature contours at $\chi = 0.2$ and $\chi = 0.4$. In the $v = 0.5$ (middle) case, the OS "pass through" each other and then dissipate. Link to movies [202–204].

hole – this defines an interaction/collapse timescale (see Eqn. (3.8) and Eqn. (3.9) for estimates). However, in a sufficiently relativistic collision, the collision timescale may be shorter than the interaction/collapse timescale, resulting in the two OS "passing through" (or bouncing off) albeit with large perturbations to their initial configuration and at a slower velocity due to the inelastic nature of the collisions.

This collision timescale *vs* interaction timescale behaviour has been seen in non-linear dynamics without gravity in the studies of relativistic collisions of non-linear solitons [205–207], where the relative coherence of the solitons post-collisions can be explained by the fact that the collision timescale is much shorter than the interaction timescale. We will discuss this in greater detail in the following section 3.4.

We find that the *initial* formation of black holes is more efficient for the $v = 0.3$ case when compared to the $v = 0.7$ case [3] – the black hole mass grow more rapidly for the $v = 0.3$ case during the collision. This could be due to the fact that the collision is "messier" when collisions are more energetic, and hence it takes longer for the excited debris to fall back into the nascent black hole. Unfortunately, our initial conditions are not sufficiently precise to enable long term tracking of the apparent horizon, leading to instabilities first seen in [208].

3.3.3 Anti-phase $\Delta\theta = \pi$ collisions

At high v, black hole formation again occurs beyond the reduced hoop conjecture line Eqn. (3.4) – reinforcing the point that in this regime "matter does not matter" and it is the gravitational dynamics that dominate [173]. Similar to the equal phase case above, at low v black hole formation is impeded, although the transition line do not coincide, but is shifted slightly to the right (towards higher compactness). This line meets the reduced hoop conjecture line at the "critical point" $\mathcal{C} = 0.071$ and $v = 0.5$, indicating that there is an additional "repulsion" between the two OS when compared to the equal phase case. This repulsion is particularly notable in the $v = 0$ case, where the transition from no black hole formation to black hole formation occurs at $\mathcal{C} \approx 0.05$ (compared to $\mathcal{C} \approx 0.035$ for equal phase collisions).

This repulsion can be explained as follows. Crucially, for anti-phase collisions, the anti-symmetry of the ϕ configuration is a constant of motion, and hence at the point of collision $\phi(x_*, t) = 0$ at all times where x_* is the plane of anti-symmetry. This is in contrast with the equal phase pair where $\phi(x_*, t)$ is free to evolve as the two OS approach each other – the symmetry of this case imposes the condition $\partial_x \phi(x_*, t) = 0$ instead. In particular, in [148, 197, 212], it was shown that in the weak gravity and non-relativistic limit, OS will "bounce back" instead of merging

[3] The mass extracted from the apparent horizon is a gauge-dependent measure, but since we are using the same gauge-evolution (see Eqn. (4.38) and Eqn. (4.37)) we can make a fair comparison.

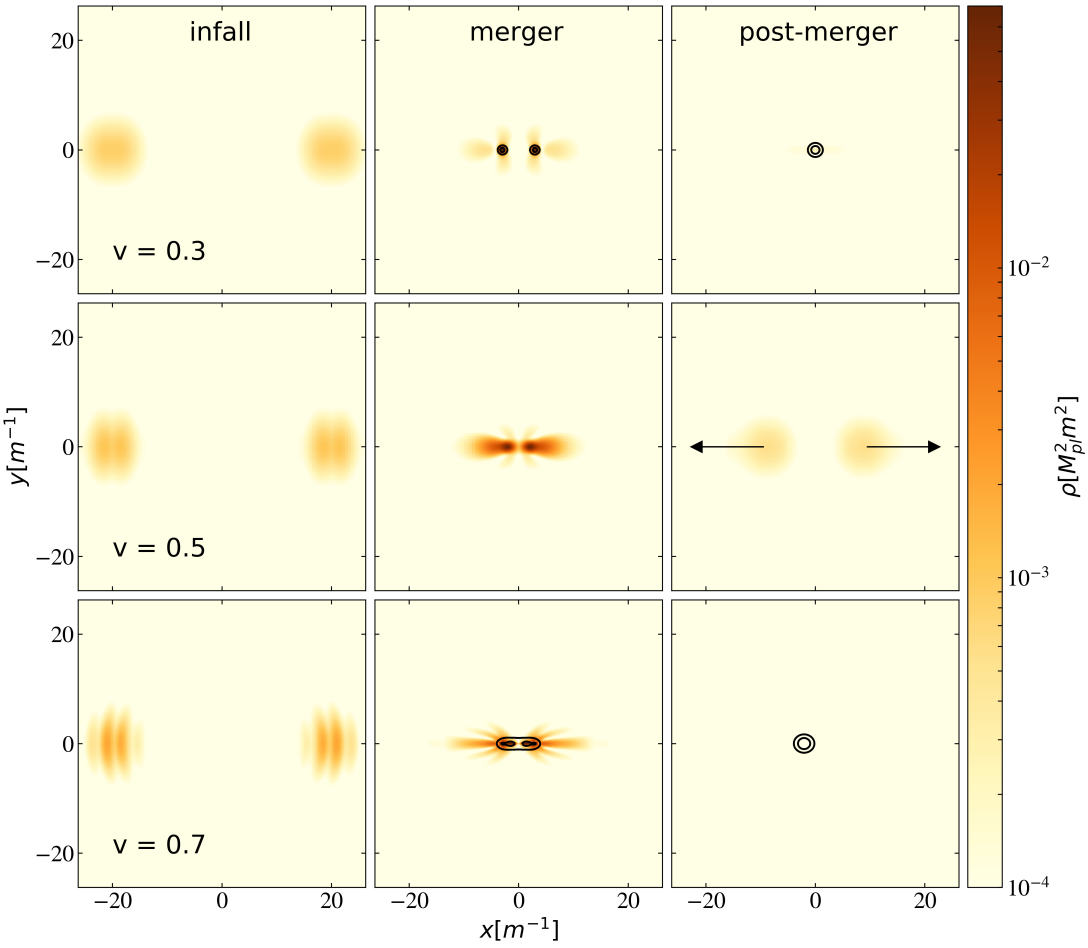

Figure 3.6: **Anti-phase $\Delta\theta = \pi$ collisions :** Three different slices of energy density ρ with $\mathcal{C} = 0.065$ with $v = 0.3$, 0.5 , 0.7 from top to bottom. The slices for the (i) infall, (ii) merger and (iii) post-merger. Black holes form in the $v = 0.3$ (top) and $v = 0.7$ (bottom) cases, with black lines indicating curvature contours at $\chi = 0.2$ and $\chi = 0.4$. In the $v = 0.5$ (middle) case, the OS "bounces back" post-collision (with black arrows indicating the direction of travel). Notice that in the $v = 0.3$ case, the OS collapse into black holes before merging. Link to movies [209–211].

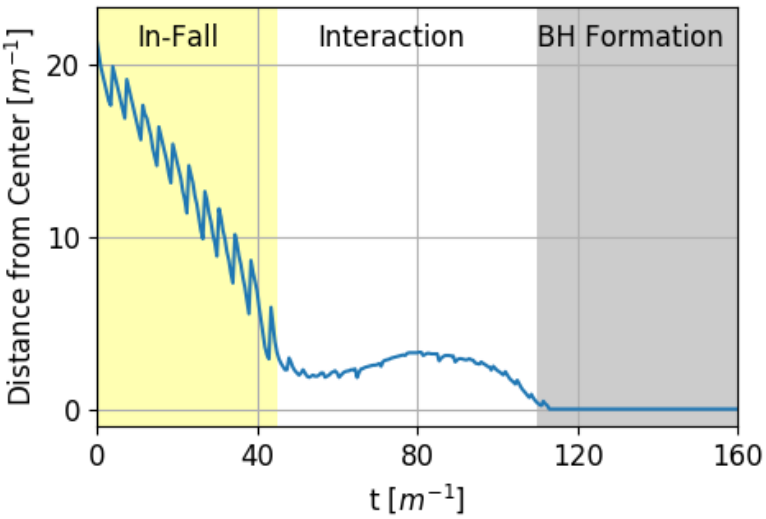

Figure 3.7: The central location of a OS/BH vs time for an anti-phase OS collision with $\mathcal{C} = 0.068$ and $v = 0.4$. The repulsiveness of the anti-phase OS rapidly slows the initial velocity down to a full stop, before rebounding slightly at $t \sim 80m^{-1}$ and then collapsing into a BH. The location of the center of the OS is taken to be the point of maximum density.

for $\Delta\phi < 7\pi/8$ [148]. In this limit, [148] argues that the oscillaton equation of motion is linear, and hence in equal phase (anti-phase) collisions, the OS tend to constructively (destructively) interfere, at least at the collision plane x_*.

In strong gravity, gravitational back-reaction is non-linear, muddling this picture somewhat. Nevertheless, the anti-symmetry of the field configuration is still conserved, so $\phi(x_*, t)$ and its time derivative $\dot{\phi}(x_*, t)$ both remain at zero for all t. This means that the time averaged (over a period of oscillation) kinetic energy density of the field configuration $\langle E_K \rangle \sim (1/2)\dot{\phi}^2$ must vanish as $x \to x_*$. As the OS approach each other, energy conservation forces the time averaged gradient energy $\langle E_G \rangle \sim (1/2)(\nabla\phi)^2$ to absorb this energy, resulting in a rapid increase in the gradient energy and thus a spiking of the scalar field spatial configuration[4]. Note that the metric and stress tensor remain symmetric in the diagonal components and anti-symmetric in the off-diagonal components throughout for both equal phase and anti-phase cases, which means that gravitational energy can still dominate near x_*.

To check this dependence, we ran a series of collisions with $\mathcal{C} = 0.028$ with zero boost for both OS, and an initial separation of $d = 40m^{-1}$. For this compactness, it was previously shown in [151] that their mergers will lead to a highly excited OS in the limit of $\Delta\theta = 0$, and hence we do not expect any black hole formation.

Since these are initially bound states, we expect that due to loss to scalar and

[4]While it is natural to describe this repulsion as a force, its behaviour is not described by a $1/r$ potential nor is it conservative. The anti-symmetric origin of the repulsion is reminiscence of the degenerate pressure of the anti-symmetric wavefunctions of fermions.

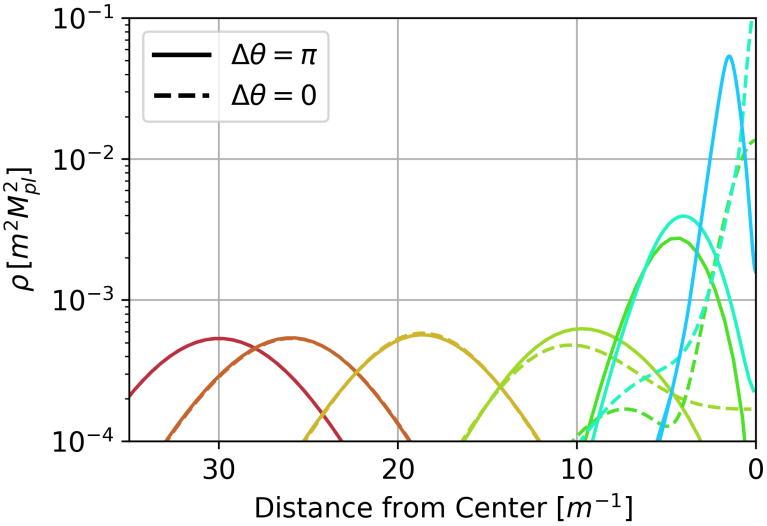

Figure 3.8: The time evolution of the profile of the energy density ρ measured along the axis of collision for both equal phase (dotted line) and anti-phase (continuous line) collisions of OS with $\mathcal{C} = 0.053$. The time evolution is indicated by colour, chronologically increasing from blue to deep red. Note that anti-phase collisions experience a repulsion due to the anti-symmetry of the field configuration, and the centers (i.e. maximum density point) of the OS remain distinct. As a result, the OS experience a compression which may lead to individual formation of black holes before final merger, or the OS "bouncing back".

gravitational wave radiation, the final state of such collisions will be a merged oscillaton. The key question is whether this merger occurs in the first collision as in the equal phase case, or will the off-phase repulsion generate pre-merger "bounces". We scan through $\Delta\theta = [0, \pi/8, \pi/4, 3\pi/8, \pi/2, 5\pi/8, 3\pi/4, 7\pi/8, 15\pi/16, \pi]$, and found that only for the cases of $\Delta\theta \geq 7\pi/8$, the OS bounces once before merger – in agreement with [148] that this repulsion is only dominant when the phase difference is near maximal.

Fig. 3.8 illustrates the comparison of the energy densities of equal phase and anti-phase collisions. At large distances, the two cases evolve similarly as they do not yet interact strongly. Their evolution begin to deviate around $d \sim 15m^{-1}$, as the OS begin to overlap and interact with each other. In the equal phase case, the OS merge and form a large central density spike at $d = 0$. On the other hand, in the anti-phase case, the OS repulse each other – note that the energy density drop at $d = 0$ – "compressing" to a smaller size but higher energy densities before bouncing back.

This repulsion and subsequent compression leads to a dramatically different black hole formation process when compared to the equal phase case. Instead of BH forming from the collapse of scalar matter after merger, the repulsion stops the motion of the OS and prevents the direct merger of the OS from occurring. The

accompanying compression of both OS leads to a subsequent *individual* collapse of the OS into separate black holes. These distinct black holes, shorn of the repulsive scalar field, then gravitate towards each other and finally form a final black hole. This general mechanism is seen in both the high velocity (i.e. above the reduced hoop conjecture line) and low velocity BH formation processes (see Figs. 3.7 and 3.8).

In between these two velocity limits, again as in the equal phase case, the collision does not yield a final black hole. Instead, it results in the two OS bouncing back, and then dispersal. While the OS experience compression during the bounce, the compression is not sufficient to push the OS into an unstable regime that led to collapse – instead it led to a dispersion of the OS into scalar waves. While oscillatons have been shown to be stable under large spherically symmetric (and shell-like) perturbations [126], the perturbations that OS here experience post-bounce are both highly asymmetric and non-shell-like. Thus our results strongly suggests that there exist unstable *non-radial* perturbation modes of OS even at low compactness, although a more detailed study is needed to confirm this conjecture.

3.4 Discussion

The most striking result of our simulations is the existence of a "stability band" of velocities whereby collisions of OS do not form black holes. We can gain a qualitative understanding as follows. The free fall time scale is given by $\tau_{\rm ff} \sim 1/\sqrt{G\rho}$, and using $\rho \sim M/R^3$ combined with Eqn. (3.2) gives

$$\tau_{\rm ff} \sim \frac{GM}{\mathcal{C}^{3/2}} \ . \tag{3.8}$$

Meanwhile the interaction timescale can be estimated by the time the two OS overlap since the scalar field configuration of the OS drop off exponentially away from its characteristic size R. If we assume that OS "pass through" (or bounce back after contact), then roughly the interaction timescale is

$$\tau_{\rm int} \sim \frac{2R}{\gamma v} = \frac{2GM}{\gamma v \mathcal{C}} \ . \tag{3.9}$$

This a conservative (i.e. *lower*) bound on $\tau_{\rm int}$ since interactions do slow down the collision – as we saw especially in the anti-phase case the repulsion slows the collision down significantly, saturating only in the high v limit.

To prevent black hole formation, as we argued in Section 3.3 the interaction timescale has to be shorter than the free-fall timescale $\tau_{\rm int} > \tau_{\rm ff}$. At low v, $\gamma \sim 1$,

we obtained the following bound

$$v > 2\mathcal{C}^{1/2} \ . \tag{3.10}$$

Since $\tau_{\rm int}$ is an underestimate, we expect Eqn. (3.10) to be a lower bound on v. Combining this with the reduced hoop conjecture limit at high gamma Eqn. (3.4), we obtain the following bound when BHs will not form

$$2\mathcal{C}^{1/2} < v < \sqrt{1 - 144\mathcal{C}^2} \ . \tag{3.11}$$

The two lines intersect at $\mathcal{C} \sim 0.07$ or $v \sim 0.5$, which is what we found numerically (see Fig. 3.1). On the other hand, the lower bound does not track the numerical results accurately – this is not surprising since such timescales arguments do not capture the full range of physics involved.

An interesting question is whether this point is a "critical point", in the sense that the two different regimes $v > 2\mathcal{C}^{1/2}$ and $v < \sqrt{1 - 144\mathcal{C}^2}$ constitute different phases and this point is where they meet as they transition into the final black hole phase. We have already seen that these two regimes exhibit different post collision behaviour, but are their end states the same or are they different? In other words, is there a transition in the endstates between the high v BH formation and low v BH formation in the black hole phase when $\mathcal{C} \gtrsim 0.07$? The natural end state for these collisions are spherical, non-rotating black holes, hence the no-hair theorem implies that their end states are fully quantified by their final BH masses. To obtain these values require running the simulations to sufficiently long timescales to achieve these final states in addition to removing the unwanted reflection of scalar and tensor waves from the boundary of the simulation domain. We are currently exploring absorptive boundary conditions to overcome this problem. We will leave this, and the computation of gravitational waves signal from such collisions to future work.

Chapter 4

Boosting oscillotons

"If the warp drive fails to activate,
the results could be... unfortunate."

Lieutenant Commander Data,
Star Trek: The Next Generation

This chapter comprises of the technical details for constructing initial data for a boosted, equal mass, head on merger of two oscillotons (OS) as well on the modifications needed during evolution. The initial conditions detailed were used as the basis for published work, [3], and Chap. 3 which describes it within this thesis. I would like to thank Thomas Helfer and Eugene Lim for their contributions towards this work. These initial conditions are also currently being used for a second paper in prep with Thomas Helfer, Eugene Lim, Marcos A.G. Garcia, and Mustafa A. Amin. That work will be discussed in Sec. 4.5. I would also like to acknowledge the contributions of Ricardo Becerril, who provided the code that generates the Fourier coefficients used to generate a single, unboosted OS. The code that was provided is detailed in [213].

4.1 Introduction and review of the construction of a single oscilloton

We wish to study the boosted head-on collisions of a class of real scalar fields solitons called oscillotons (OS) [121] using full (3+1) dimensional numerical relativity. The knowledge of how to boost OS is vital if we wish to study OS-OS binary coalescence, and hence study their corresponding GW signals. OS are stable on cosmological time scales [195], and are an interesting type of "exotic compact object", (ECO), especially since they could be a good approximation of an axion star where the leading order ϕ^4 interaction is negligible due to having a large axion decay constant,

f_a, [114, 122, 123]. These objects could therefore detected by LIGO/Virgo[1], and provide some clue into what comprises the dark matter in our universe. We direct the reader both to Sec. 1.3.5 and Chap. 3 for more information on both OS and axion stars.

To accomplish our goal of studying the boosted head-on collision, the construction of the initial data was split into 3 distinct phases:

1. Construct initial data for an equilibrium configuration of a single OS; something that has been accomplished before, notably in [121, 126, 214, 215], and will be reviewed in the remainder of this section

2. Lorentz Boost a single OS; theoretically simple to do but technically involved. This will be explored in Sec. 4.2

3. Superimpose two OS; non-trivial and first done for a non-boosted case in [151]. This will be explored in Sec. 4.3

Once testing had begun, it was clear that additional steps would have to be undertaken for the evolution to be successful. We talk about these additional steps in Sec. 4.4. For what remains of this section, we shall now review how one generates the initial data for a single OS.

We construct our initial data by solving for a single OS profile as outlined in [121, 126, 214–216]. The key details of these methods[2] are reproduced here.

To obtain the radial OS profiles we use the ansatz for the spherically symmetric line element:

$$ds^2 = -\alpha(r,t)^2 dt^2 + a(r,t)^2 dr^2 + r^2(d\theta^2 + \sin^2(\theta)d\phi^2), \tag{4.1}$$

where $\alpha(r,t)$ is the lapse function, $a(r,t)$ is the radial metric function and where we use the polar areal gauge (i.e we force the line element to have the chosen form at all times, so that the area of the sphere with $r = R$ is always equal to $4\pi R^2$. Therefore $\partial_t \gamma_{\theta\theta} = \partial_t \gamma_{\phi\phi} = 0$ [217, 218]).

The complete evolution of the scalar field and the spacetime is described by the Klein-Gordon equation, Eqn. (1.26), the Hamiltonian constraint Eqn. (1.67) and Momentum constraint equations Eqn. (1.29).

To solve the Klein-Gordon equation, Eqn. (1.67), it is useful to introduce the auxiliary scalar field variables $\psi = \partial_r \phi$ and $\Pi = a\partial_t(\phi)/\alpha^3$. It is also useful to introduce the following dimensionless quantities, $r = \lambda/m$ (here we change convention

[1] See Chap. 2, and more specifically Fig. 2.1 for the LIGO/Virgo frequency band for axion stars.

[2] Although all methods in [121, 126, 214–216] are valid, the notation presented throughout this chapter is specifically from [126]

[3] It useful to remind ourselves that although we define Π here, when solving in 3+1 Π is defined as in Eqn. (1.68)

from [126] to avoid confusion later), $t \to t/m$, and $\phi \to \phi/m$. The Klein-Gordon equation become

$$\partial_t \phi = \frac{\alpha}{a}\Pi, \tag{4.2}$$

$$\partial_t \Pi = \frac{1}{\lambda^2}\partial_\lambda \left(\frac{\lambda^2 \alpha \psi}{a}\right) - a\alpha\psi, \tag{4.3}$$

$$\partial_t \psi = \partial_\lambda \left(\frac{\alpha \Pi}{a}\right). \tag{4.4}$$

Eqn. (4.3) has a form that can cause our entire numerical scheme to become unstable, due to the error introduced from the finite differencing method (see [20] for an in-depth description of this problem). Using a simple trick, $\partial_\lambda/\lambda^2 = 3\partial_{\lambda^3}$, first introduced in [219], we can transform Eqn. (4.3) into the following form

$$\partial_t \Pi = 3\frac{\mathrm{d}}{\mathrm{d}\lambda^3}\left(\frac{\lambda^2 \alpha \psi}{a}\right) - a\alpha\psi. \tag{4.5}$$

This form of Eqn. (4.3) is now numerically stable and is said to be regularised. The Hamiltonian constraint equation becomes

$$\frac{\partial_\lambda a}{a} = \frac{1-a^2}{2\lambda} + \frac{\lambda}{4}\left(\psi^2 + \Pi^2 + a^2\phi^2\right), \tag{4.6}$$

and thanks to the polar areal slicing condition, the momentum constraint equations take the form

$$\frac{\partial_\lambda \alpha}{\alpha} = \frac{\partial_\lambda a}{a} + \frac{a^2-1}{\lambda} - \lambda a^2 \phi^2. \tag{4.7}$$

In order to construct the initial data for a single OS, it is useful to define $A = a^2$ and $C = \frac{a^2}{\alpha^2}$. Our equations become

$$\partial_\lambda A = \frac{A\lambda}{2}\left(C\left(\partial_t\phi\right)^2 + \left(\partial_\lambda\phi\right)^2 + A\phi^2\right) + \frac{A}{\lambda}\left(1-A\right), \tag{4.8}$$

$$\partial_\lambda C = \frac{2C}{\lambda}\left(1 + A\left(\frac{1}{2}\lambda^2\phi^2 - 1\right)\right), \tag{4.9}$$

$$C\partial_t^2\phi = -\frac{1}{2}\partial_t C \partial_t \phi + \partial_\lambda^2\phi + \partial_\lambda\phi\left(\frac{2}{\lambda} - \frac{\partial_\lambda C}{2C}\right) - A\phi, \tag{4.10}$$

$$\partial_t A = \lambda A \partial_t\phi\partial_\lambda\phi. \tag{4.11}$$

Eqn. (4.10) has a non-linearity, $\frac{\partial_\lambda C}{2C}$, which is difficult to deal with. However as we redefined our variables, we can now combine Eqn. (4.10), and Eqn. (4.9) to remove this, and hence the instability present in our system of equations is removed [126, 216]. Solutions are then obtained by expanding the metric functions and the

scalar field in their Fourier components:

$$\phi(t,\lambda) = \sum_{j=1}^{j_{\max}} \phi_j(\lambda)\cos(j\omega t)\,, \tag{4.12}$$

$$A(t,\lambda) = \sum_{j=0}^{j_{\max}} A_j(\lambda)\cos(j\omega t)\,, \tag{4.13}$$

$$C(t,\lambda) = \sum_{j=0}^{j_{\max}} C_j(\lambda)\cos(j\omega t)\,, \tag{4.14}$$

where ω is a coherently oscillating base frequency and $j_{\max}$ is the maximum order in the Fourier expansion to which the solution is obtained. Using the boundary conditions of asymptotic flatness, and regularity, the Fourier coefficients, and ω, can be found numerically, provided the initial values $\phi_i(0)$ and $C_i(0)$.

In the sections that follow, we used the code of [213] to generate solutions for large $j_{\max}$ using a shooting technique. As the numerical domain of the shooting technique is small, we truncate the field at a finite radius, and set $\phi = 0$, and match the solution to Schwarzchild solution. It was this initial data that was Lorentz boosted and superimposed.

4.2 Lorentz boosting a single oscilloton

The initial data generated using the methodology outlined in Sec. 4.1 is described in the 1+1 dimensional, spherically symmetric coordinates, (t,λ). To transform between the 1+1 dimensional spherically symmetric coordinates, and a 3+1 Cartesian coordinate system, we can use the standard definition that $\lambda = \sqrt{x^2+y^2+z^2}$. $A(t,\lambda)$, $C(\lambda,t)$ and $\phi(\lambda,t)$ have no θ,Φ dependence due to being spherically symmetric, and hence our definition of λ in Cartesian coordinates is sufficient for now. When calculating boosted metric variables in Sec. 4.2.2 the full coordinate system will be defined. Here we want to emphasise that we are talking about an unboosted system still, and that as we will be constructing data for 3+1, we will be using the scalar field evolution equations defined in Sec. 1.3.2.

The objective of this section is to how to apply a boost in the x direction for a single OS. We denote (t,x,y,z) as the "lab" frame coordinates (the coordinates that relate to the Cartesian coordinates in GRChombo, and ultimately what we construct our initial conditions in), and (t',x',y',z') as the coordinates in the OS "rest" frame.

To apply a boost in the positive x-direction, with some velocity, v, we can define

a Lorentz transformation of

$$\begin{aligned} t &= \gamma(t' + vx'), \\ x &= \gamma(x' + vt'), \\ y &= y', \\ z &= z', \end{aligned} \tag{4.15}$$

where γ is the Lorentz factor of defined as $\gamma \equiv (1-v^2)^{-\frac{1}{2}}$. As y and z are unaffected by the transformation we shall drop the prime notation for them when referring to them in the OS frame. The inverse Lorentz transformation is

$$\begin{aligned} t' &= \gamma(t - vx), \\ x' &= \gamma(x - vt). \end{aligned} \tag{4.16}$$

Due to the technicalities of boosting an OS, we will describe the boosting procedure systematically, firstly how to boost the static profile Sec. 4.2.1 and then how to construct the metric and the ADM decomposition required Sec. 4.2.2.

4.2.1 Boosting the OS profile

In this section we will discuss how to boost the scalar field profile. We begin by considering the boosted OS, in the OS frame, where we are using the shorthand that $\lambda' = \sqrt{x'^2 + y^2 + z^2}$

$$\phi'(t', \lambda') = \sum_{j=1}^{j_{\max}} \phi'_j(\lambda') \cos(j\omega t') \,. \tag{4.17}$$

Scalar fields are invariant under a Lorentz transformation, which implies that

$$\phi'(t', \lambda') \equiv \phi(\gamma(t - vx), \tilde{\lambda}) \equiv \tilde{\phi}, \tag{4.18}$$

where we are using $\tilde{\lambda}$ as shorthand for $\sqrt{\gamma^2(x - vt)^2 + y^2 + z^2}$ and shortened the expression again to use $\tilde{\phi}$. As the OS will have a non-zero initial velocity, and potentially a non-zero initial time, we need to calculate Π_{3+1}, defined in Eqn. (1.68), which will be used in the 3+1 scalar field evolution equations. I want to emphasise that this is different from the auxiliary variable defined for the 1D case, however for compactness reasons, from this point onwards we will drop the $3+1$ subscript on Π and not refer to the old definition.

The definition of Π contains spatial and time derivatives of ϕ in the lab frame. It also contains metric components, that we will demonstrate how to calculate in

Sec. 4.2.2. We calculate the derivatives in the lab frame as

$$\partial_t\tilde{\phi} = \sum_{j=1}^{j_{\max}} \Big(\partial_t\phi_j(\tilde{\lambda})\cos\left(j\omega\gamma(t-vx)\right) - \phi_j(\tilde{\lambda})j\omega\gamma\sin\left(j\omega\gamma(t-vx)\right)\Big)\,, \quad (4.19)$$

$$\partial_x\tilde{\phi} = \sum_{j=1}^{j_{\max}} \Big(\partial_x\phi_j(\tilde{\lambda})\cos\left(j\omega\gamma(t-vx)\right) + \phi_j(\tilde{\lambda})j\omega v\gamma\sin\left(j\omega\gamma(t-vx)\right)\Big)\,, \quad (4.20)$$

$$\partial_y\tilde{\phi} = \sum_{j=1}^{j_{\max}} \partial_y\phi_j(\tilde{\lambda})\cos\left(j\omega\gamma(t-vx)\right)\,, \quad (4.21)$$

$$\partial_z\tilde{\phi} = \sum_{j=1}^{j_{\max}} \partial_z\phi_j(\tilde{\lambda})\cos\left(j\omega\gamma(t-vx)\right)\,. \quad (4.22)$$

All of the derivatives of $\phi_j(\tilde{\lambda})$ can be calculated using a radial derivative of the initial data generated for a static solution via both the invariance of a scalar field under coordinate transformation, and the chain rule. For example

$$\partial_t\phi_j(\tilde{\lambda}) \equiv \partial_t\phi_j(\lambda') = \frac{\partial\phi_j(\lambda')}{\partial\lambda'}\frac{\partial\lambda'}{\partial t} \quad (4.23)$$

In the implementation of the code for GRChombo second order finite differencing was used to calculate the radial derivatives as the spatial resolution of the input data was far higher then that of any simulation that could be feasibly run with GRChombo. The derivatives of λ' are as follows

$$\partial_t\lambda' = -\frac{\gamma v x'}{\lambda'},\ \partial_x\lambda' = \frac{\gamma x'}{\lambda'},\ \partial_y\lambda' = \frac{y}{\lambda'},\ \partial_z\lambda' = \frac{z}{\lambda'}. \quad (4.24)$$

Using Eqn. (4.24) and the chain rule, one can then calculate the derivatives of ϕ needed in the lab frame. With the metric components calculated in the next section, these derivatives allow us to fully calculate Π.

Beyond the numerical domain that can be obtained for the static solution, we set $\tilde{\phi} = 0$ as before, as well as setting the time and spatial derivatives equal to 0. This implies that outside of the numerical domain, Π is also defined as being equal to 0.

4.2.2 Calculating the metric and the ADM decomposition

In order to fully determine the initial data, we must determine the effect of the Lorentz boost on the metric, and subsequently calculate the ADM decomposition. To achieve this, their are 3 steps that need to be considered

1. Transform the metric, Eqn. (4.1), into Cartesian coordinates

2. Boost the metric that is now in Cartesian coordinates in the x-direction, using a Lorentz boost, defined in Eqn. (4.15)

3. Calculate the ADM decomposition

Before we describe each of these steps systematically, it is very useful to remind ourselves that to transform the coordinates of a metric, as well as to boost a metric (which is a transformation again), we can use the following

$$g_{\lambda\delta}(x^\tau) = \frac{\partial x'^\mu}{\partial x^\lambda}\frac{\partial x'^\nu}{\partial x^\delta} g'_{\mu\nu}(x'^\tau) \tag{4.25}$$

where the primed coordinates are the coordinate system that you are changing into. With this reminder, we can now proceed to generate our initial data.

To transform from spherical to Cartesian coordinates, we can define the following spherical coordinate system

$$\begin{aligned} t &= t, \\ x &= \lambda \cos(\Phi) \sin(\theta), \\ y &= \lambda \sin(\Phi) \sin(\theta), \\ z &= \lambda \cos(\theta), \end{aligned} \tag{4.26}$$

where Φ is the inclination, θ is the azimuthal angle and $\lambda = \sqrt{x^2+y^2+z^2}$ (as before). For technical reasons, we used a modified line element

$$ds^2 = -\alpha(r,t)^2 dt^2 + A(r,t)dr^2 + r^2(d\theta^2 + \sin^2(\theta)d\phi^2), \tag{4.27}$$

where compared to Eqn. (4.1), we have used $A(r,t) = a^2(r,t)$. This is to simplify our calculations later on. As before, in what follows we will use the dimensionless units $r = \lambda/m$, and $t \to t/m$. Using Eqn. (4.25), we now proceed with our coordinate transform form into Cartesian coordinates. We omit $\frac{\partial x'^\mu}{\partial x^\lambda}$, also referred to as the Jacobian for compactness reasons. Under the coordinate transformation, our metric becomes

$$g_{\mu\nu} = \begin{pmatrix} -\alpha^2 & 0 & 0 & 0 \\ 0 & \frac{Ax^2+y^2+z^2}{\lambda^2} & \frac{(A-1)xy}{\lambda^2} & \frac{(A-1)xz}{\lambda^2} \\ 0 & \frac{(A-1)xy}{\lambda^2} & \frac{x^2+Ay^2+z^2}{\lambda^2} & \frac{(A-1)yz}{\lambda^2} \\ 0 & \frac{(A-1)xz}{\lambda^2} & \frac{(A-1)yz}{\lambda^2} & \frac{x^2+y^2+Az^2}{\lambda^2} \end{pmatrix}, \tag{4.28}$$

where for compactness reasons, we are using the short-hands of $\lambda = \sqrt{x^2+y^2+z^2}$ by definition, $\alpha = \alpha(\lambda, t)$ and $A = A(\lambda, t)$.

Following our coordinate transform, we can apply a Lorentz boost in the x-

direction, defined in Eqn. (4.15). For completeness, we can define $\frac{\partial x'^{\mu}}{\partial x^{\lambda}}$ as

$$\frac{\partial x'^{\mu}}{\partial x^{\lambda}} \equiv \Lambda^{\mu}{}_{\lambda} = \begin{pmatrix} \gamma & -v\gamma & 0 & 0 \\ -v\gamma & \gamma & 0 & 0 \\ 0 & 0 & 1 & 0 \\ 0 & 0 & 0 & 1 \end{pmatrix}, \tag{4.29}$$

where $\Lambda^{\mu}{}_{\lambda}$ is the Lorentz group. Again, using Eqn. (4.25), Eqn. (4.28) is transformed into the OS boosted frame, accomplishing step 2 of our list to successfully construct our initial data. We do not show the full boosted metric here, but instead present the metric in the ADM decomposition. Starting with the spatial metric, $\tilde{\gamma}_{ij}$,

$$\tilde{\gamma}_{ij} = \begin{pmatrix} \gamma^2\left(\frac{y^2+z^2+\bar{A}x'^2}{\lambda'^2} - v^2\bar{\alpha}^2\right) & \frac{y\gamma\left(\bar{A}-1\right)x'}{\lambda'^2} & \frac{z\gamma\left(\bar{A}-1\right)x'}{\lambda'^2} \\ \frac{y\gamma\left(\bar{A}-1\right)x'}{\lambda'^2} & \frac{\bar{A}y^2+z^2+x'^2}{\lambda'^2} & \frac{yz\left(\bar{A}-1\right)}{\lambda'^2} \\ \frac{z\gamma\left(\bar{A}-1\right)x'}{\lambda'^2} & \frac{yz\left(\bar{A}-1\right)}{\lambda'^2} & \frac{y^2+x'^2+z^2\bar{A}}{\lambda'^2} \end{pmatrix}, \tag{4.30}$$

where we are using the shorthand of λ' previously defined. We are also using $\bar{\alpha} = \sqrt{\bar{A}/\bar{C}}$ defined as

$$\bar{A} \equiv A(t', \lambda') = \sum_{j=0}^{j_{\max}} A_j(\lambda') \cos\left(j\omega t'\right), \tag{4.31}$$

$$\bar{C} \equiv C(t', \lambda') = \sum_{j=0}^{j_{\max}} C_j(\lambda') \cos\left(j\omega t'\right), \tag{4.32}$$

which are the initial conditions generated from the 1D unboosted case, however with the coordinates now in the OS frame. The boosted shift vector, $\tilde{\beta}_i$, is

$$\begin{aligned} \tilde{\beta}_1 &= \gamma^2 v\left(\bar{\alpha}^2 - \frac{\bar{A}x'^2 + y^2 + z^2}{\lambda'^2}\right), \\ \tilde{\beta}_2 &= -\frac{\gamma v y\left(\bar{A}-1\right)x'}{\lambda'^2}, \\ \tilde{\beta}_3 &= -\frac{\gamma v z\left(\bar{A}-1\right)x'}{\lambda'^2}, \end{aligned} \tag{4.33}$$

and boosted lapse, $\tilde{\alpha}$,

$$\tilde{\alpha} = \sqrt{-\frac{\gamma^2\left(v^2-1\right)^2\bar{\alpha}^2\bar{A}\lambda'^2}{v^2\bar{\alpha}^2x'^2 - \bar{A}\left(\lambda'^2 - v^2\bar{\alpha}^2\left(y^2+z^2\right)\right)}}. \tag{4.34}$$

To finish our constructing our initial data, we can calculate K_{ij} as per Eqn. (1.23). As this calculation is simple, rather lengthy, and hence uninstructive, the resultant

form of K_{ij} has been omitted. It should be noted that our derivatives are taken in the lab frame, and as such we get derivatives of $\bar{A}$ and $\bar{C}$. These can be calculated using the chain rule much like we did before for ϕ.

Finally, we should note that much as before, we must prescribe the initial data for α and A that lie beyond the numerical domain of the shooting used to calculate the unboosted 1D OS. This can simply be done by matching to Schwarzchild, and boosting appropriately.

4.3 Superimposing two oscillotons

We have demonstrated how to construct the initial data for a boosted OS. In this section, we will explain how to superimpose two OS such that one can construct the initial conditions for a variety of potential simulations. The technique that will demonstrated is based on [151], but has been modified for boosted OS.

Given a single boosted OS, we can generate OS-OS initial data by superimposing two single boosted OS:

$$\begin{aligned}
\phi_{\rm tot} &= \phi|_{x'-x'_0} + \phi|_{x'+x'_0} \\
\Pi_{\rm tot} &= \Pi|_{x'+x'_0} + \Pi|_{x'-x'_0} \\
\alpha_{\rm tot} &= \alpha|_{x'+x'_0} + \alpha|_{x'-x'_0} \\
\beta_{i,\rm tot} &= \beta_i|_{x'+x'_0} + \beta_i|_{x'-x'_0} \\
\gamma_{ij,\rm tot} &= \gamma_{ij}|_{x'+x'_0} + \gamma_{ij}|_{x'-x'_0} - h_{ij} \\
K_{ij,\rm tot} &= K_{ij}|_{x'+x'_0} + K_{ij}|_{x'-x'_0}
\end{aligned} \quad , \tag{4.35}$$

where $\pm x'_0$ are the locations of the centres of the two OS, and h_{ij} is a constant metric. Note that we have dropped the tilde notation on α, β_i and γ_{ij}.

Naively one would define $h_{ij} = \delta_{ij}$[4], which would make the asymptotic values the same for a single OS. However, at the centre of each OS the volume element is distorted by its companion with respect to a single OS, and as commented on in [151], this induces significant excitations in each OS, which can lead to premature collapse of the OS, and changes in the gravitational wave energy of a head on collision. The distortion of the volume element can easily be seen in Fig. 4.1.

Thus the solution to this problem prescribe h_{ij} such that the change in the volume element at the centre of each star due to its companion is minimised. This

[4]We remind the reader that δ_{ij} is the Kronecker delta and for 3D is defined as $\delta_{ij} = diag(1, 1, 1)$

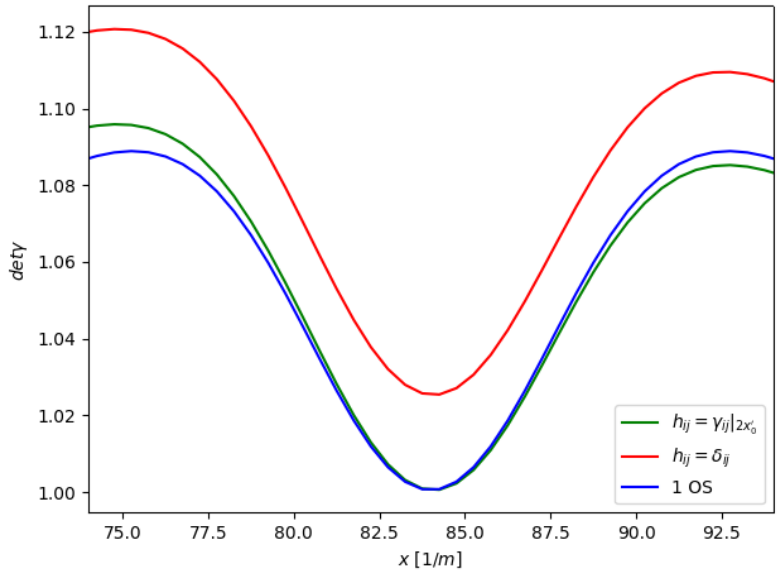

Figure 4.1: We present three scenarios for $det\,\gamma$, $\mathcal{H}$; $h_{ij} = \delta_{ij}$, and $h_{ij} = \gamma_{ij}|_{2x'_0}$ i.e the "unfixed" and "fixed" cases, for two equal compactness, $\mathcal{C} = 0.049$, symmetric unboosted OS, where one of the stars in centred on $x = 84$, as well as a single OS. It can be seen that as we use the "fixed" version of h_{ij}, the volume element of the star mirrors that of a single star.

can be done in practise by defining

$$h_{ij} = \gamma_{ij}|_{2x'_0} = \begin{pmatrix} \gamma^2\left(\frac{y^2+x'^2\bar{A}|_{2x'_0}}{\rho'^2} - v^2\bar{\alpha}^2|_{2x'_0}\right) & \frac{y\gamma\left(\bar{A}|_{2x'_0}-1\right)x'}{\rho'^2} & 0 \\ \frac{y\gamma\left(\bar{A}|_{2x'_0}-1\right)x'}{\rho'^2} & \frac{y^2\bar{A}|_{2x'_0}+x'^2}{\rho'^2} & 0 \\ 0 & 0 & 1 \end{pmatrix}, \tag{4.36}$$

where we have set $z = 0$ as we are assuming that the OS will be positioned on a $x-y$ plane taken at $z = 0$, $\rho' = \sqrt{x'^2 + y'^2}$, and $\bar{\alpha}^2|_{2x'_0}$ and $\bar{A}|_{2x'_0}$, are the initial values of $\bar{\alpha}$ and $\bar{A}$ with $z = 0$ from Eqn. (4.31) and Eqn. (4.32) chosen at $2x'_0$, where $2x'_0$ is the separation between the OS. Defining h_{ij} in this way can be seen in the reduction of the distortion in Fig. 4.1, which results in a reduction in the Hamiltonian constraint violation, Fig. 4.2, by an order of magnitude. The Momentum constraint violation is also similarly reduced when a boost is applied to the system. The prescribed method for reducing the distortion, eliminates the excitations in each OS.

One can now also prescribe the relative "phase", $\Delta\theta$, between the stars by modifying Eqn. (4.35). A full definition of the phase of an OS can be found in Chap. 3, however here it is sufficient to say that the phase is defined due to the symmetry of the ϕ profiles of the OS, with a symmetric, $\Delta\theta = 0$, set-up corresponding to $\phi|_{x'-x'_0} = \phi|_{x'+x'_0}$ and an antisymmetric, $\Delta\theta = \pi$, configuration corresponding to $\phi|_{x'-x'_0} = -\phi|_{x'+x'_0}$. "Mixed phase", sometimes referred to as "off-phase",

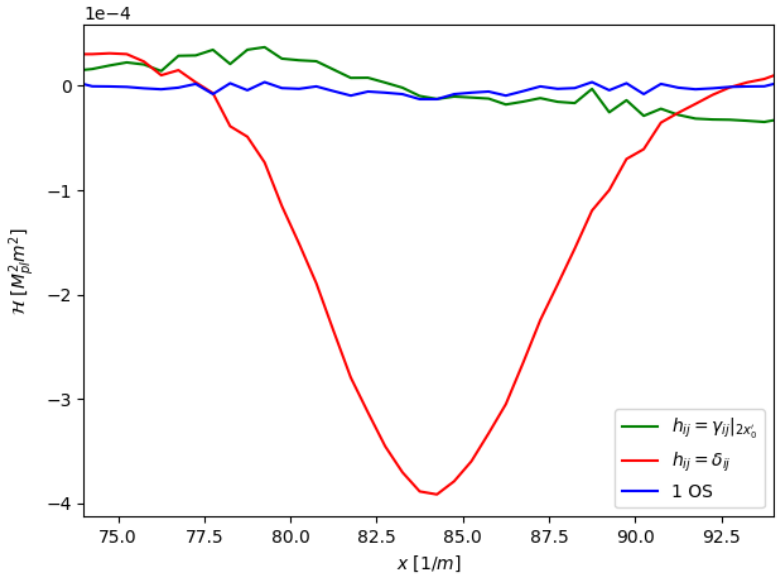

Figure 4.2: We present three scenarios for the Hamiltonian constraint violation, $\mathcal{H}$; $h_{ij} = \delta_{ij}$, and $h_{ij} = \gamma_{ij}|_{2x'_0}$ i.e the "unfixed" and "fixed" cases, for two equal compactness, $\mathcal{C} = 0.049$, symmetric unboosted OS, where one of the stars in centred on $x = 84$, as well as a single OS. It can be seen when we modify h_{ij} such that we reduce the distortion of the volume element at the centre of an OS, $\mathcal{H}$ is dramatically reduced. A similar picture can also be constructed for the Momentum constraint violation, $\mathcal{M}_i$.

$0 < \Delta\theta < \pi$, correspond to $\phi_1 = A\phi_2$, where A is some constant between $-1, 1$. It is important to note that we are talking about equal compactness, $\mathcal{C}$, in this definition, and that, if t is chosen on the initial hypersurface is equal to 0, then the OS pair constructed will have a symmetric configuration.

Equal $\mathcal{C}$, antisymmetric boosted OS, can be constructed by modifying Eqn. (4.35) such that $\phi|_{x'+x'_0} \to -\phi|_{x'+x'_0}$ and $\Pi|_{x'+x'_0} \to -\Pi|_{x'+x'_0}$ with t being chosen as 0 on the initial hypersurface. Equal $\mathcal{C}$, unboosted, "mixed phase" OS can be constructed by not modifying Eqn. (4.35), but instead choosing a different t for each OS that is constructed before superposition such that for OS 1, $t = 0$ and for OS 2, $t = \frac{\Delta\theta}{\omega}$. In this work we do not discuss how to construct equal $\mathcal{C}$, "mixed phase" boosted OS.

One final comment about constructing initial data; for low v boosts our initial data produces low relative Hamiltonian constraint violation and momentum constraint violation ($\mathcal{O}(0.8)\%$ for a boost of $v = 0.6$). When boosting to higher velocities, we use a relaxation scheme to lower both of these relative constraint violations.

4.4 Evolution

Following the prescription laid about above, one can fully construct initial data for a pair of boosted OS. For low velocity boosts it was sufficient to use the evolution scheme, and gauge conditions outlined in Sec. 1.4, however for higher velocity boosts, without modification, gauge artefacts are present. The gauge artefacts manifested themselves in two effects:

1. χ "bumps" - In the region where each OS was initially set-up, the value of χ would grow slowly after the OS has moved from this region. This effect did not effect evolution, or gravitational wave extracted as per [151].

2. K "waves" - Thin bands of $\mathcal{O}(1)$ values of K would propagate in the direction of the boost from each OS. This effect caused unwanted AMR, and needed to be removed.

Fig. 4.3 shows the K "wave" effect for a single boosted OS. We will now comment on each effect and explain how to modify the gauge conditions to remove them. The χ "bumps " do not effect the evolution of a pair of OS for head on collisions, or their gravitational wave signatures due to them being purely gauge effects. This was verified in [151] by comparing degenerate OS-OS head on collisions, which collapse to BH before collision, with BH-BH head on collisions. Due to these initial conditions potentially being used for OS-OS inspirals (which we will comment on in Sec. 4.5), as a precaution we removed the χ "bumps " by modifying the shift gauge conditions, presented in Eqn. (1.73) and Eqn. (1.74) to

$$\partial_t \beta^i = \frac{3}{4}\Gamma^i - \eta\beta^i \,. \tag{4.37}$$

Mirroring an idea presented in [220,221], we have integrated Eqn. (1.74) with respect to time and set the integration constants, $\Gamma^i(t=0)$ and $\beta^i(t=0)$, to zero. This has been done, as $\Gamma^i(t=0)$ and $\beta^i(t=0)$, contain an impression of the original location of each OS, and if not set to zero, the original impression would "freeze" in (using the terminology of [220, 221]). Thus once the integration constants has been set to zero, the impression will also be removed.

To avoid having undesirable gauge effects, i.e, K "waves" we can introduce friction terms into Eqn. (1.72), such that it becomes

$$\partial_t \alpha = \underbrace{-\mu\alpha K + \beta^i \partial_i \alpha}_{\text{as in Eqn. (1.72)}} - \begin{cases} A(\alpha - \alpha_{analytical}(t)) & t < t_{merger} \\ B(\alpha - \alpha_{constant}) e^{-\left(\frac{t-t_{merger}}{t_{decay}}\right)^2} & t \geq t_{merger} \end{cases} , \tag{4.38}$$

where A and B are constants, $\alpha_{analytical}(t)$ is the analytical version of $\tilde{\alpha}$ generated

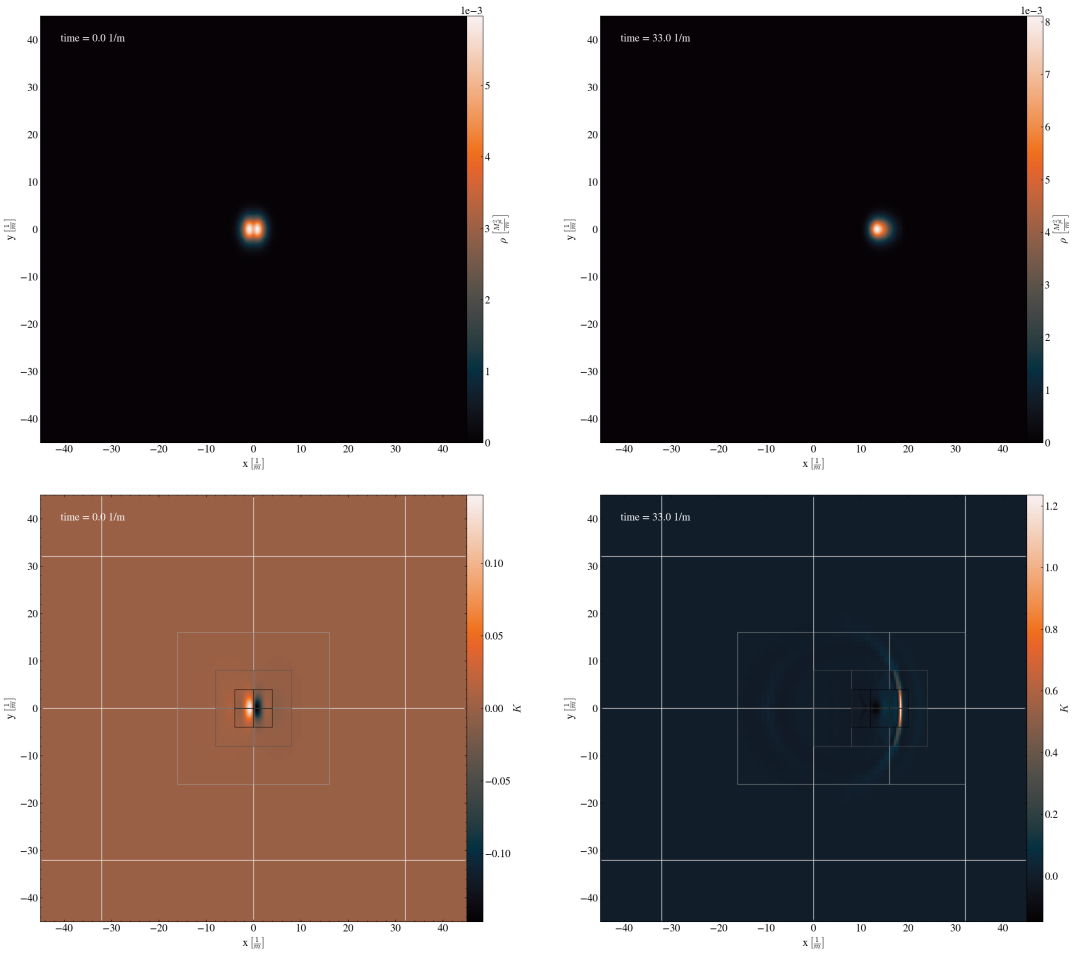

Figure 4.3: An OS with initial boost $v = 0.5$ and compactness, $\mathcal{C} = 0.137$. Top panel) The energy density, ρ, for the OS at $t = 0$, (left), and $t = 33$, (right). Bottom panel) The trace of the extrinsic curvature, K, for the OS at $t = 0$, (left), and $t = 33$, (right). It can be seen that the value of K grows from $\mathcal{O}(0.1)$ to $\mathcal{O}(1)$ as simulation progresses. This is realised as a K "wave" propagating along the axis in which the OS was boosted, and is a gauge effect.

in the initial conditions for a boosted star, Eqn. (4.34), but evaluated at current time t, $\alpha_{constant}$ is a constant, t_{merger} is the time in which the OS take to merge, and t_{decay} is another constant. $\alpha_{analytical}(t)$ provides a good approximation for the OS as they begin to collide, and hence, when the OS collide at t_{merger}, it's no longer valid as a good approximation. In the work done in Chap. 3, $A = B = \alpha_{constant} = 1$ and $t_{decay} = 7$.

The addition of the terms in Eqn. (4.38) cause two different effect depending on t. If $t < t_{merger}$, the friction term pulls α towards the analytic gauge calculated in Eqn. (4.34), and thus will eliminate the K "waves". If $t \geq t_{merger}$, and importantly a black hole would form, we allow our friction term to decay as it no longer provides a good approximation for the system. However, after a black hole has formed, sometimes K "waves" can form[5], so the decay of the friction term is tuned with t_{decay} such that we can still remove the K "waves" , but that it decays fast enough such that it allows the puncture gauge, Eqn. (1.72), to be used, and our evolution to remain stable.

4.5 Discussion and future work

In this chapter, we have demonstrated how the initial conditions for a pair of boosted OS can be constructed, with variable phase, and explained how to modify the gauge conditions such that there are no gauge artefacts during evolution. These initial conditions have already been used in the study of head-on boosted equal mass oscillotons (OS) collisions for both the cases where the OS have equal phases or are maximally off-phase (anti-phase) (see Chap. 3 and [3]), and currently are being used in a paper in preparation with Thomas Helfer, Eugene Lim, Marcos A.G. Garcia, and Mustafa A. Amin about colliding equal $\mathcal{C}$ OS with an impact parameter.

The work involving colliding OS with an impact parameter aims to study two effect: 1) Is it possible to create OS as the result of a collision that have a defined angular momentum, similar to those constructed in [222], and 2) when colliding two OS such that there resulting product is a spinning black hole, if one increases the initial boost of each OS, what happens to the formation of the black hole? Without the boost code presented in the above chapter, these questions could not be answered.

Another useful question that can be asked, is what is the gravitational wave signature that is expected from an OS-OS inspiral? The initial conditions presented here allow this question to be answered, and simulations to answer this question have been performed. However, due to the large amount of orbits required, and the

[5]This was seen for equal $\mathcal{C}$ OS collisions with an impact parameter.

high resolution required to study the gravitational wave output from the resulting collision, we did not pursue this avenue of research due to computational and time limitations. It is hoped that, in the future someone will be able to perform these simulations, especially with the sensitivity in LIGO expected to increase in the coming years [223]. A GW from an OS-OS signal would be a smoking gun for new physics.

Chapter 5

Spherically symmetric collapse in Khronometric theory

"Like they say in the Temporal Mechanics Department, there is no time like the present."

Future Admiral Kathryn Janeway,
Star Trek: Voyager

This chapter comprises of the research done on spherically symmetric collapse in Khronometric theory, which is based on unpublished work with Eugene Lim, Diego Blas and Enrico Barausse. This work proved extremely challenging, and we were not able to derive any firm results. However, a number of avenues were explored and we obtained a greater understanding of their respective problems. We will describe the various approaches taken, and suggest directions for future research. As noted in the introduction, due to the topic of this research, this chapter is self contained and includes all relevant introductory material.

5.1 Introduction

General Relativity (GR) is beautiful. From the very first tests of GR, like the perihelion precession of Mercury's orbit, to the recent detections of gravitational waves from from the binary coalescence of black holes (BH) [7–12] and neutron stars [13], GR presents itself to be ***the*** theory governing gravity. One may ask why we should continue studying "alternative" or "modified" theories of gravity[1], when no evidence for violations of general relativity in the genuinely strong-field regime of

[1]See [224] for a comprehensive pre-LIGO review of modified theories of gravity

gravity have been found [225, 226]. What could motivate this seemingly misguided study?

Quantum. In the earliest moments of our universe, in the singularities of black holes and at high energies GR breaks down. Indeed, even Einstein himself argued that gravity would needed to be modified for quantum effects to be taken into account [227, 228]. We can try to treat this problem by unifying GR and Quantum Field Theory (QFT) in the hope that where GR breaks down, this new "Quantum Gravity" will take over.

How would one construct such a theory? A simple idea would be to reconsider some of the fundamental ideas that knit together GR. In this chapter we will consider the violation of one of these key ideas, local Lorentz Invariance. Much work has been carried out in this field, however we will consider Khronometric Theory (sometimes referred to as T-Theory), the low energy limit of the Horava Gravity. Horava Gravity is power counting renormalisable [229], so one expects it to be a viable candidate for Quantum Gravity.

Black holes exist in nature. A fundamental test of any theory of modified gravity is whether it can produce black holes such that they look like the ones we observe. Spherically symmetric static black hole solutions have been found in Khronometric Theory [230], however the formation mechanism for them has not yet been tested.

In this chapter, we will present the research undertaken to model spherically symmetric collapse in Khronometric Theory, and document the various approaches we undertook. In Sec. 5.2 we discuss Lorentz-Violating gravity, and more specifically Khronometric Theory. We also comment on the connection between Khronometric Theory and Einstein-Aether Theory, the latter already having successful spherical collapse simulations [231, 232]. In Sec. 5.3 and Sec. 5.4 we explore our work of Gravitational Collapse in Khronometric theory, where we discuss our theoretical and numerical set-up. Sec. 5.5 concerns itself with the results from the initial approach, and details some methodology that can be used to explain the outcome of the simulations. Sec. 5.6 describes an attempt at regularising our system of equations, and shows results from an in-depth testing of the regularisation. Lastly, in Sec. 5.7 we discuss our findings, and its implications for future work in this field.

5.2 Lorentz-Violating gravity and Khronometric theory

In this section we introduce Lorentz-violating gravity and, in particular, Khronometric theory. We consider the Arnowitt-Deser-Misner (ADM) decomposition for

the metric

$$ds^2 = (-N^2 + N_i N^i)dt^2 + 2N_i dx^i dt + \gamma_{ij} dx^i dx^j \,, \tag{5.1}$$

where we foliate spacetime into spacelike hypersurfaces of constant time coordinate. We define N as the lapse, N_i as the shift vector and γ_{ij} as the spatial metric. It should be noted that this is the same decomposition as in Eqn. (1.18), however with the lapse relabelled from $\alpha \to N$ and the shift relabelled $\beta_i \to N_i$. Khronometric Theory violates Lorentz symmetry by introducing a vector field (Aether field), u^μ, of everywhere unit magnitude that introduces a "preferred direction" [233]. We require the vector field to be orthogonal to hypersurfaces of constant time, T [230][2]. With this requirement, the vector field becomes

$$u_\mu = \frac{\partial_\mu T}{\sqrt{g^{\mu\nu}\partial_\mu T \partial_\nu T}} = N\delta^T_\mu \,. \tag{5.2}$$

T is a scalar field, and is known as the Khronon [235]. It should be emphasised, that unlike in GR, the lapse is no longer a gauge choice, and is a spin 0 mode that is an excitation of the foliation structure of spacetime [236], which in turn, sets the global time. The action of Khronometric theory [229, 237] is

$$S_H = \frac{1-\beta}{16\pi G}\int dT d^3x N\sqrt{\gamma}\left(K_{ij}K^{ij} - \frac{1+\lambda}{1-\beta}K^2 + \frac{1}{1-\beta}{}^{(3)}R + \frac{\alpha}{1-\beta}a_i a^i\right) \,, \tag{5.3}$$

where ${}^{(3)}R$ is the Ricci Scalar associated with the spatial metric γ_{ij}, $a_i = \partial_i \ln N$ is the acceleration of the lapse, α, β and λ are dimensionless coupling constants, and the extrinsic curvature K_{ij} is defined as

$$K_{ij} = \frac{1}{2N}\left(\partial_t \gamma_{ij} - D_i N_j - D_j N_i\right) \tag{5.4}$$

where D_i is the three dimensional covariant derivative associated with the spatial metric, γ_{ij}. G is defined as the "bare" gravitational constant, related to the Newtonian gravitational constant

$$G_N = \frac{2G}{2-\alpha} \,. \tag{5.5}$$

Eqn. (5.3) is also the low-energy limit of Horava gravity, which is a proposed ultraviolet (UV) complete theory for gravitational interaction [229, 237], with the action

$$S = \frac{1-\beta}{16\pi G}\int dT d^3x N\sqrt{\gamma}\left(\mathcal{L}_2 + \frac{1}{M_*^2}\mathcal{L}_4 + \frac{1}{M_*^4}\mathcal{L}_6\right) \,, \tag{5.6}$$

[2] In the literature this is also known as the St*ü*ckelberg formalism, and where the St*ü*ckelberg field, $\phi = const$ and is written in the gauge where the field coincides with $\phi = T$. This choice of the formalism is referred to as the "unitary" gauge [234].

where

$$\mathcal{L}_2 = K_{ij}K^{ij} - \frac{1+\lambda}{1-\beta}K^2 + \frac{1}{1-\beta}{}^{(3)}R + \frac{\alpha}{1-\beta}a_i a^i \,. \tag{5.7}$$

$\mathcal{L}_4$ and $\mathcal{L}_6$ contain terms that are that are fourth and sixth order in the spatial derivatives respectively. M_* is some new mass scale, and suppresses $\mathcal{L}_4$ and $\mathcal{L}_6$ at low energies, but allows these terms to dominate in the UV. The presence of sixth order terms in the spatial derivatives is crucial for power counting renormalisability [229, 238]. M_* is bounded from below to be greater than 10^{10} GeV by looking at the matter sector, and is bounded from above to be less than 10^{16} GeV to allow the theory to remain perturbative on all scales [236, 239]. In what follows, the form of $\mathcal{L}_4$ and $\mathcal{L}_6$ will not be considered as we will be working exclusively in Khronometric Theory.

The allowed parameter space for Khronometric theory is small, and is constrained by a number of theoretical and observational constraints, which have been collected in [240, 241], and reproduced here. Theoretical constraints require that the scalar mode of our theory is neither a ghost or a tachyonic field [236, 237]. This yields

$$0 < \alpha < 2, \quad \beta > 0 \tag{5.8}$$

Observationally a number of constraints bind our parameter space, including current constraints from parameterized post-Newtonian (PPN) parameters, Big Bang nucleosynthesis (BBN), binary pulsar, binary black hole observations and gravitational waves [235, 239–245]. This results in

$$0 \leq \alpha \leq 10^{-5}, \quad 0 \leq \beta \leq 10^{-15}, \quad \lambda \leq 10^{-1} \,. \tag{5.9}$$

Further constraints will come from extreme mass inspirals gravitational wave emission [239], as well as further gravitational wave observations. Before continuing, it should be noted that the parameter space was larger when this research was undertaken in 2016, and hence, parameters will be used that do not meet observational constraints.

Khronometric theory has many similarities to a theory known as Einstein-Aether Theory in which spherical collapse simulations have been achieved [231, 232] (see [246] for a comparison of collapse in both theories). We can define Einstein-Aether theory by introducing a vector field u^μ (dubbed the Aether field as before), of everywhere unit norm. However we do not make the requirement that the Aether field is hypersurface orthogonal unlike in Khronometric Theory. Up to quadratic terms in first derivatives of the field, the most generic action is [238]

$$S = \frac{1}{16\pi G}\int d^4x\sqrt{-g}\left(R + M^{\delta\sigma}_{\mu\nu}\nabla_\delta u^\mu \nabla_\sigma u^\nu\right) \,, \tag{5.10}$$

where G is the bare gravitational constant in Einstein-Aether Theory, R is the Ricci Scalar, g is the determinant of the metric and

$$M^{\delta\sigma}_{\mu\nu} = c_1 g^{\delta\sigma} g_{\mu\nu} + c_2 \delta^\delta_\mu \delta^\sigma_\nu + c_3 \delta^\delta_\nu \delta^\sigma_\mu + c_4 u^\delta u^\sigma g_{\mu\nu} \,, \tag{5.11}$$

where c_i are the four coupling constants of the theory. A spherically symmetric static Aether field is always surface orthogonal [238], and as hypersurface orthogonal solutions of Einstein-Aether Theory are solutions of Khronometric Theory [247], we expect the solutions of spherically symmetric static black holes in Einstein-Aether Theory to be solutions in Horava gravity. However it is not known if non-static spherically symmetric solutions match in the two theories, which implies that we do not know if spherical collapse in the two theories are identical or lead to the same end state [246].

To finish this section, we will present the field equations for Khronometric Theory as per [248, 249]. The variation of Eqn. (5.3) with respect to the lapse N results in

$$\frac{{}^{(3)}R}{1-\beta} - K^{ij}K_{ij} + \frac{1+\lambda}{1-\beta}K^2 + \frac{\alpha a_i a^i}{1-\beta} - \frac{2}{1-\beta}\alpha a^2 - \frac{2}{1-\beta}D_i(\alpha a^i) = 0 \,, \tag{5.12}$$

the variation with respect to the shift N_i yields

$$D_j\left(K^{ij} - \frac{1+\lambda}{1-\beta}\gamma^{ij}K\right) = 0 \,, \tag{5.13}$$

and finally, the variation with respect to the spatial metric γ_{ij} gives

$$\begin{aligned}
&\frac{1}{1-\beta}\left({}^{(3)}R^{ij} - \frac{1}{2}{}^{(3)}R\gamma^{ij}\right) + \frac{1}{N}D_t\left(K^{ij} - \frac{1+\lambda}{1-\beta}\gamma^{ij}K\right) \\
&+ \frac{2}{N}D_k\left(N^{(i}(K^{j)k} - K\frac{1+\lambda}{1-\beta}\gamma^{j)k})\right) + 2K^{ik}K^j_k \\
&- \frac{1+\beta+2\lambda}{1-\beta}K^{ij}K - \frac{1}{2}\gamma^{ij}\left(K^{kl}K_{kl} + \frac{1+\lambda}{1-\beta}K^2\right) \\
&- \frac{1}{(1-\beta)N}\left(D^iD^jN - \gamma^{ij}D_kD^kN\right) + \frac{1}{1-\beta}\alpha a^i a^j - \frac{\alpha a_i a^i}{2(1-\beta)}\gamma^{ij} = 0 \ ,
\end{aligned} \tag{5.14}$$

where D_i denotes the covariant derivative compatible with γ_{ij}, and $D_t \equiv \partial_t - N_k D^k$. Comparing these equations to GR, Eqn. (5.14) is a modified evolution equation, Eqn. (5.12) is a modified Hamiltonian constraint, and Eqn. (5.13) is a modified momentum constraint. Unlike in GR, Eqn. (5.12) needs to be solved on every time step as the lapse is not a gauge choice [248].

5.3 Black holes and collapse in Khronometric theory

In this section we will give an overview of black holes in Khronometric theory, and then show the equations of motion, boundary conditions, and initial conditions for gravitational collapse.

One of the defining characteristics of a black hole is the presence of an event horizon[3]. Classically we can define an event horizon to be a surface in which particles can never escape to infinity [17, p.222], or alternatively, as per a more beautiful definition in [20]:

"Once an object has crossed r =horizon, the advance of time becomes equivalent to a decrease in r, that is, the object must continue towards smaller values of r for the same reason that time must flow to the future. As nothing can stop the flow of time, there is not force in the Universe capable of preventing the object from reaching the singularity."

This definition uses radial coordinates, and places the singularity at $r = 0$. For all its beauty of the definition provided by [20], an alternative wording that will serve us better is that an event horizon is a causal boundary that separates the interior and exterior of the black hole [238]. As you will see in the upcoming section, the definition of a horizon will become blurred when talking about Lorentz-Violating gravity.

In Horava gravity, massive particles contain higher-order momentum terms

$$E^2 = c_n^2 p^2 + \frac{a_n p^4}{M_*^2} + \frac{b_n p^6}{M_*^4} \tag{5.15}$$

where E and p are the energy of the particle and its spatial momentum, and c_n, a_n and b_n are coefficients of order one depending on the particle species n [252]. As $p \to \infty$ the group and phase velocities become unbounded [253], and hence the theory can have excitations whose velocity exceeds that of light, and thus escape from inside GR horizons. These modes could even probe the immediate vicinity of the singularity [252]. So what does this mean for the existence of black holes?

In Khronometric Theory we can still define a black hole as there still exists causal boundaries in which particles with infinitely large velocities cannot escape [253]. The boundary of the causally connected region is known as the "universal horizon", and

[3]Although this definition lacks precision, it provides us with a good viewpoint moving forwards. An object without a horizon, is sometimes referred to as naked singularity, or a "massless" black hole and this type of object is expected to not exist in nature due to the cosmic censorship hypothesis [250]. However in [251], via "extreme" fine tuning, it was found that these could be formed in scalar field collapse, dubbed Choptuik collapse.

in terms of foliation this horizon corresponds to a leaf which is disconnected from spatial infinity [230, 246, 252, 254].

Static spherically symmetric black holes in Khronometric Theory have been studied in [230, 238, 252] and solutions calculated numerically. In terms of collapse processes, none have been studied so far, except for in Einstein-Aether Theory where [246] argues that in the collapse simulation of [231], a universal horizon was formed, however it is again prudent to emphasise that even though the end-states of the theory coincide, it is not known if the collapse process is the same. It seems that our task is to perform gravitational collapse in Khronometric theory, and to hopefully reach an end-state where we have formed a universal horizon. It should be emphasised that we will not be considering any matter as in [231], but instead the collapse of the Khronon field.

As a first step to study gravitational collapse in spherical symmetry, we consider a purely vacuum spacetime. Choosing a gauge such that $N_i = 0$, we can write

$$N = A(t,r)^2\,, \tag{5.16}$$

$$\gamma_{ij}dx^i dx^j = F(t,r)^2\mathrm{d}r^2 + B(t,r)^2 r^2 \mathrm{d}\Omega^2\,. \tag{5.17}$$

$N_i = 0$ ensures that once a set of spatial coordinates is chosen on some initial $T =$ constant hypersurface, then spatial coordinates are fixed in the whole spacetime. However you are free to choose any set of coordinates on the initial hypersurface. One way to get rid of the residual gauge freedom is to impose that r matches the areal radius at $t = 0$, such that $B(t = 0, r) = 1$.

Using the constraint equations, Eqn. (5.12) and Eqn. (5.13), and by introducing the variables $X \equiv \partial_t F/A^2$, $Y \equiv \partial_t B/A^2$, $F_r \equiv \partial_r F$ and $B_r \equiv \partial_r B$, the evolution equations, Eqn. (5.14), can be put in the form

$$\partial_t \boldsymbol{u} + \boldsymbol{M}\cdot\partial_r \boldsymbol{u} = \boldsymbol{S}\,, \tag{5.18}$$

$$\partial_r^2 A = R\,, \tag{5.19}$$

where $\boldsymbol{u} = (X, Y, B_r, F_r)$, $\boldsymbol{M}$ is the characteristic matrix

$$\boldsymbol{M} = \begin{pmatrix} (\beta+\lambda)AB^2Fk_1 & 2(\lambda+1)ABF^2k_1 & \frac{2(\alpha-2)(\lambda+1)A^2}{\alpha(\beta-1)(\beta+3\lambda+2)BF} & 0 \\ (\beta+\lambda)AB^2Fk_2 & 2(\lambda+1)ABF^2k_2 & -\frac{(\alpha-2)(\beta+\lambda)A^2}{\alpha(\beta-1)(\beta+3\lambda+2)F^2} & 0 \\ 0 & -A^2 & 0 & 0 \\ -A^2 & 0 & 0 & 0 \end{pmatrix}, \tag{5.20}$$

and the sources, $\boldsymbol{S}$, are

$$\boldsymbol{S} = -\Bigg(-\frac{(\beta+2\lambda+1)(\alpha(\beta-1)-2(\lambda+1))FY^2A^2}{\alpha(\beta-1)(\beta+3\lambda+2)B^2}+\frac{(\beta\alpha+\alpha+2(\alpha+1)\lambda+2)\left(F^2-r^2{B_r}^2\right)A^2}{r^2\alpha(\beta-1)(\beta+3\lambda+2)B^2F}$$
$$+\frac{\left(F\left(-r^2(\beta+\lambda)(\alpha(\beta-1)-2(\lambda+1))X^2-2(\beta\alpha+\alpha+2(\alpha+1)\lambda+2)\right)-4r(\alpha-2)(\lambda+1)F_r\right)A^2}{2r^2\alpha(\beta-1)(\beta+3\lambda+2)F^2}$$
$$-\frac{2B_r\left((\alpha(\beta-1)+6(\lambda+1))F+r(\alpha-2)(\lambda+1)F_r\right)A^2}{r\alpha(\beta-1)(\beta+3\lambda+2)BF^2}+\frac{2(\beta-1)B^2Fk_1XA}{r}$$
$$+\frac{2(\beta-1)BFk_1\left(rXB_r-FY\right)A}{r}-(\beta+\lambda)B^2k_1XF_rA-\frac{4B_r\partial_rAA}{(\beta-1)BF}$$
$$-\frac{2\left(r(\beta-1)(\beta+\lambda)k_1YB_rF^3+2\partial_rA\right)A}{r(\beta-1)F}-\frac{2(\alpha(\beta+4\lambda+3)-2(\lambda+1))(\partial_rA)^2}{(\beta-1)(\beta+3\lambda+2)F},$$
$$-\frac{((\beta+\lambda)(\beta+2\lambda+1)-\alpha(\beta-1)(\lambda+1))Y^2A^2}{\alpha(\beta-1)(\beta+3\lambda+2)B}+\frac{(\beta+\lambda)(\alpha(\beta-1)-2(\lambda+1))XYA^2}{\alpha(\beta-1)(\beta+3\lambda+2)F}$$
$$+\frac{(\lambda\alpha+\alpha+\beta+\lambda)\left(r^2{B_r}^2-F^2\right)A^2}{r^2\alpha(\beta-1)(\beta+3\lambda+2)BF^2}+\frac{2(-\beta-\lambda+\alpha(\beta+2\lambda+1))B(\partial_rA)^2}{(\beta-1)(\beta+3\lambda+2)F^2}-(\beta+\lambda)B^2k_2XF_rA$$
$$-\frac{B\left(F\left(r^2(\beta+\lambda)(\alpha(\beta-1)+\beta+\lambda)X^2-2(\lambda\alpha+\alpha+\beta+\lambda)\right)-2r(\alpha-2)(\beta+\lambda)F_r\right)A^2}{2r^2\alpha(\beta-1)(\beta+3\lambda+2)F^3}$$
$$+\frac{B_r\left(2(-\beta\alpha+\alpha+3(\beta+\lambda))F+r(\alpha-2)(\beta+\lambda)F_r\right)A^2}{r\alpha(\beta-1)(\beta+3\lambda+2)F^3}+\frac{2(\beta-1)B^2Fk_2XA}{r}+\frac{2BA\partial_rA}{r(\beta-1)F^2}$$
$$+\frac{2(\beta-1)BFk_2\left(rXB_r-FY\right)A}{r}+\frac{2B_r\left(\partial_rA-(\beta-1)(\beta+\lambda)F^4k_2Y\right)A}{(\beta-1)F^2},-2AY\partial_rA,-2AX\partial_rA\Bigg). \tag{5.21}$$

The source of the equation of A reads

$$R=\frac{1}{4\alpha r^2B^2F}\Big\{4\alpha r\partial_rAB\left(B\left(rF_r-2F\right)-2rB_rF\right)$$
$$-4\alpha k_3r^2A^3B^2F\left[B^2\left(F\left(r(\beta+\lambda)\partial_rX+2(\beta-1)X\right)-r(\beta+\lambda)F_rX\right)\right.$$
$$\left.+2BF\left((\beta-1)rB_rX+F\left((\lambda+1)r\partial_rY-(\beta-1)Y\right)\right)-2r(\beta+\lambda)B_rF^2Y\right]$$
$$+A\left[B^2\left(F\left(r^2(\beta+\lambda)X^2-2\right)+4rF_r\right)+2\left(F^3\left(r^2(\beta+2\lambda+1)Y^2+1\right)-r^2{B_r}^2F\right)\right.$$
$$\left.+4rB\left(rF\left((\lambda+1)FXY-\partial_rB_r\right)+B_r\left(rF_r-3F\right)\right)\right]\Big\}\,, \tag{5.22}$$

where k_1, k_2 and k_3 are three arbitrary functions of t and r, which can be chosen at will. The characteristic matrix has four eigenvalues

$$\dot{r}=0\,, \tag{5.23}$$
$$\dot{r}=ABF\left(k_1(\beta+\lambda)B+2(\lambda+1)k_2F\right)\,, \tag{5.24}$$
$$\dot{r}=\pm s_0\frac{A^2}{F}\,, \tag{5.25}$$

where

$$s_0^2=\frac{(\alpha-2)(\beta+\lambda)}{\alpha(\beta-1)(\beta+3\lambda+2)}\,, \tag{5.26}$$

is the propagation speed squared for the spin-0 modes in Minkowski space. This

means that the sub-system X, Y, B_r, F_r is strongly hyperbolic provided $k_1 = k_2 \neq 0$, i.e has 4 unique eigenvectors [20, p158-164]. Finally, the constraint equation reads

$$\begin{aligned} A\Big[&2BF\left(F(\lambda+1)r\partial_t\partial_r B + (\beta-1)(\partial_r B\partial_t Fr - \partial_t BF)\right) \\ &+B^2(Fr(\beta+\lambda)\partial_t\partial_r F + \partial_t F(2(\beta-1)F - \partial_r Fr(\beta+\lambda))) - 2\partial_r B\partial_t BF^2 r(\beta+\lambda)\Big] \\ &-2\partial_r ABFr(B\partial_t F(\beta+\lambda) + 2\partial_t BF(\lambda+1)) = 0 \end{aligned} \tag{5.27}$$

To specify our initial data, we can first remind ourselves that we can set $B(t = 0, r) = 1$ by tweaking our gauge, hence $B_r(t = 0, r) = 0$. That leaves us with initial data for X, Y, F_r, subject to the constraint equation given by Eqn. (5.27). Therefore we are left with two pieces of independent initial data. We can choose time-symmetric initial data with $X = Y = 0$, then Eqn. (5.27) is automatically satisfied, and we are only left with the choice of F_r. We also need two boundary conditions for the equation for A, Eq. (5.19).

To attempt to figure out the remaining initial conditions and boundary conditions, we can examine work carried out in [230, 238, 255]. We can consider a general static, spherically symmetric vacuum solution in Schwarzschild coordinates (t', r', θ, ϕ). This is relevant because if the boundary of our computational grid is sufficiently far it is reasonable to assume the boundary to be static. In more detail, the metric and aether for a static, spherically symmetric vacuum solution reads

$$ds^2 = -f(r')dt'^2 + \frac{b(r')^2}{f(r')}dr'^2 + r'^2 d\Omega^2, \tag{5.28}$$

$$u_{\mu'}dx^{\mu'} = \frac{1 + f(r')a(r')^2}{2a(r')}dt' + \frac{b(r')}{2a(r')}\left[\frac{1}{f(r')} - a(r')^2\right]dr' . \tag{5.29}$$

Near spatial infinity, we can imposes asymptotic flatness such that f, a, b takes the series expanded form [230]

$$f(r') = 1 + \frac{f_1}{r'} + \frac{\alpha}{48}\frac{f_1^3}{r'^3} + \cdots , \tag{5.30}$$

$$b(r') = 1 + \frac{\alpha}{16}\frac{f_1^2}{r'^2} - \frac{\alpha}{12}\frac{f_1^3}{r'^3} + \cdots , \tag{5.31}$$

$$a(r') = 1 - \frac{1}{2}\frac{f_1}{r'} + \frac{a_2}{r'^2} + \left(\frac{1}{16}f_1^3 - \frac{\alpha}{96}f_1^3 - f_1 a_2\right)\frac{1}{r'^3} + \cdots , \tag{5.32}$$

where the constants f_1 and a_2 specify the solution. In more detail, f_1 is the solution's "characteristic size" as measured at spatial infinity, i.e. we can define a "gravitational radius", $r_g = -f_1$, which is in turn related to the solution's total mass $M_{\rm tot}$ (as measured by an observer at spatial infinity) by $r_g = 2G_N M_{\rm tot}$.

The coordinate transformation from Schwarzschild coordinates and our coordi-

nates (t, r, θ, ϕ) are defined by

$$r' \equiv rB(t, r)\,, \tag{5.33}$$

$$\frac{\partial r'(r,t)}{\partial t} = -u_{r'}(r')u_{t'}(r')\frac{f(r')}{b(r')^2} = -u_{t'}(r')u^{r'}(r')\,, \tag{5.34}$$

$$t' = t + R(r')\,, \tag{5.35}$$

where $u_{t'}(r')$, $u_{r'}(r')$ and $u^{r'}(r')$ are given by Eq. (5.29). Under this coordinate transformation, Eqs. (5.28) and (5.29) become

$$ds^2 = -u_{t'}(r')^2dt^2 + \frac{[b(r')\partial_r r']^2}{u_{t'}(r')^2}dr^2 + r^2B(t,r)^2d\Omega^2, \tag{5.36}$$

$$u_\mu dx^\mu = u_{t'}(r')dt\,. \tag{5.37}$$

We can observe that $N(r,t) = A(r,t) = u_{t'}(r') = u_{t'}(rB(t,r)) = 1 + f_1/(2r') = 1+f_1/[2rB(t,r)]+...$, which provides boundary conditions for $A(r,t)$ and $\partial A(r,t)/\partial r$ as $r \to \infty$[4]. When choosing the initial data for F (and thus for F_r) at $t = 0$, we want to make sure they are static near spatial infinity. Now, Eq. (5.36) gives $F(t,r) = b(r')\partial_r r'/u_{t'}(r')$, but at $t = 0$, $r' = r$, hence $F(t = 0, r) = b(r)/u_{t'}(r) = 1 - f_1/(2r) + ...$ Therefore we can choose our initial condition for F to be

$$F = 1 - \frac{f_1}{2r}\left(1 + \tanh\left(r - r_c\right)\right)\,, \tag{5.38}$$

where we can define r_c to be some point where we want to centre our bump. This would correspond to a shell of the Khronon field. We impose regularity at the centre of the grid as in [246]. Our evolution variables are (X, Y, F_r, B_r), but the source of the evolution equations depends on F and B. To obtain these variables we integrate $\partial_r B = B_r$ and $\partial_r F = F_r$ on each slice.

5.4 Numerical simulations

To study the described system, and to ultimately simulate gravitational collapse of the Khronon field, code was written in C utilising the PETSc toolkit. PETSc is a suite of data structure and routines for the scalable solutions of systems modelled by partial differential equations [256]. This code can be easily adapted to solve other 1 dimensional problems, and has the following key features:

- *MPI scalability:* PETSc contains features that allows the user to program using

[4]Alternatively, one can impose that $\partial_r A = 0$ at $r = 0$ via regularity. In the work that follows, both variations of the boundary condition where implemented, with the regularity condition being used for results presented in this thesis.

MPI [135], and are implemented in the code. MPI allows the code to scale efficiently to several thousand CPU-cores per run, and hence, allows highly resolved simulations to take place.

- *Fixed grid mesh refinement:* The code features fixed mesh refinement around $r = 0$, which allows the user to run highly resolved simulations near where the universal horizon would form, but maintain an outer boundary at $r = R$ which is far enough away from the $r = 0$ to be considered static. The code uses 2nd order stencils at the boundaries between meshes.

- *4th order discretisation in time, and up to 4th order discretisation in space:* PETSc features solvers in time that allow upto 6th order discretisation, however for this implementation we use Runge-Kutta 4th order (RK4) [137]. The code allows a user to take upto 4th order spatial derivatives, but 2nd order are used due to the 2nd order stencils at the fixed mesh boundaries.

- *Elliptical equation solver:* An elliptical solver is implemented using RK2, but simple trapezium and Euler methods are optional within the code. The elliptical solver can also be initialised before evolution takes place to solve initial conditions, and runs until the values converge.

- *Kreiss-Oliger dissipation:* Kreiss-Oliger dissipation [138] is used to control errors and a 3rd Order method was implemented to ensure stability of the system.

- *Common output and restart:* PETSc allows the easy use of MPI Read/Write, which allows the code to output the values of any chosen variable upto every time step in *.dat* format. These files can then be used to restart the code, and due to the filetype, allow for easy analysis.

- *Error monitoring:* The code monitors and outputs the value of the constraint equation. The code will automatically stop if the value gets too high.

Using the described code, we solved for gravitational collapse of the Khronon field as follows: We set up our initial conditions, and then calculate A by solving the initial conditions of Eqn. (5.19) using the codes elliptical solver until a solution for A converged. We choose the RK2 method of the elliptical equation solver. Next, as mentioned above, we time evolve using RK4, hence solving Eqn. (5.18). After a time step has taken place, we solve Eqn. (5.19) for that time step, and then recover B and F by integrating $\partial_r B$ and $\partial_r F$ using RK2. Once this process has been completed we take another time step, and repeat until some predefined end time, or the code automatically stops due to a crash. As A, B and F are of order 1 plus small and

our other variables are order small, a cut off $\pm 10^{-18}$ was introduced due to machine precision. This is an optional feature in the code, and can easily be disabled.

Data was analysed using a set of parallelised Python scripts. As well as analysing the data, the scripts would perform unit tests on the code, as well as provide visualisation of the variables. The initial conditions where also verified using a Mathematica script to ensure that A was calculated correctly.

A number of simulations were using values for the dimensionless coupling constants, α, β, λ that are currently[5] permitted by observation. We also ran simulations with values that were larger (but still allowed under general theoretical considerations) such that a broad range of parameters could can be tested.

It was found that this system of equations was largely unstable for theoretically allowed values for the parameters α, β and λ, therefore no firm results were obtained. In the following sections we will investigate what could have caused the instability (Sec. 5.5), as well as showing how to regularise the equations (Sec. 5.6). The results of the regularisation will then be discussed.

5.5 Instability of gravitational collapse

When using the system of equations outlined in Sec. 5.3, and using theoretically allowed values for the parameters α, β and λ, it was found that we could not achieve gravitational collapse of the Khronon field, due to values at small r exponentially growing, and causing the simulations to crash. In the following section, we shall explore what could be causing the instability at low r, and show some results to help validate the cause of the instability.

5.5.1 Analysis of $r << 1$

To gain an understanding of what is causing our instability at small r, we focus on terms in Eqn. (5.18) of type $1/r^n$, where $n > 0$. Analysing Eqn. (5.18), we find that they will be dominated by 2 of the 4 equations, $\dot{X}$ and $\dot{Y}$ as they contain r^{-2} terms, whilst $\dot{B}_r$ and $\dot{F}_r$ do not. Looking at the r^{-2} terms we see that we can reduce Eqn. (5.18) to

$$\dot{X} = \frac{1}{r^2}\frac{(\alpha\beta + 2(\alpha+1)\lambda + \alpha + 2)A(t,r)^2\left(B(t,r)^2 - F(t,r)^2\right)}{\alpha(\beta-1)(\beta+3\lambda+2)B(t,r)^2F(t,r)} + \dots, \quad (5.39)$$

$$\dot{Y} = \frac{-1}{r^2}\frac{(\alpha\lambda + \alpha + \beta + \lambda)A(t,r)^2\left(B(t,r)^2 - F(t,r)^2\right)}{\alpha(\beta-1)(\beta+3\lambda+2)B(t,r)F(t,r)^2} + \dots, \quad (5.40)$$

[5]The values tested were valid when the simulations were initially ran, however the latest constraints have currently ruled much of this parameter space out.

where we emphasise that in the analysis that follows we will be ignoring $\dot{B}_r$ and $\dot{F}_r$ equations. For simplicity, we will drop the +... notation, and combine the constants in Eqn. (5.39) and Eqn. (5.40) into simpler terms

$$\dot{X} = \frac{1}{r^2}\frac{\sigma}{\omega}\frac{A(t,r)^2\left(B(t,r)^2 - F(t,r)^2\right)}{B(t,r)^2F(t,r)}\,, \tag{5.41}$$

$$\dot{Y} = \frac{-1}{r^2}\frac{\gamma}{\omega}\frac{A(t,r)^2\left(B(t,r)^2 - F(t,r)^2\right)}{B(t,r)F(t,r)^2}\,, \tag{5.42}$$

where

$$\begin{aligned}\sigma &= \alpha\beta + 2(\alpha+1)\lambda + \alpha + 2\,,\\ \gamma &= \alpha\lambda + \alpha + \beta + \lambda\,,\\ \omega &= \alpha(\beta-1)(\beta+3\lambda+2)\,.\end{aligned} \tag{5.43}$$

A simple observation one can make is that there could be other terms that could contribute to the small r instability, and that the terms chosen here could easily be neglected if the r terms in in the numerator and denominator cancel somehow. A simple way to counter this argument is to perform a perturbation around Minkowski to study the behaviour of Eqn. (5.41) and Eqn. (5.42) at the $r << 1$ limit. The perturbation is of the form

$$B(t,r) = 1 + \epsilon\delta B(t,r) + O(\epsilon^2)\,, \tag{5.44}$$

$$F(t,r) = 1 + \epsilon\delta F(t,r) + O(\epsilon^2)\,, \tag{5.45}$$

$$A(t,r) = 1 + \epsilon\delta A(t,r) + O(\epsilon^2)\,, \tag{5.46}$$

where ϵ is small constant. Using the perturbation, we note that by definition

$$X(t,r) = \frac{\epsilon\delta\dot{F}}{(1+\epsilon\delta A(t,r))^2} + O(\epsilon^2) \approx \epsilon\delta\dot{F} + O(\epsilon^2)\,, \tag{5.47}$$

$$Y(t,r) = \frac{\epsilon\delta\dot{B}}{(1+\epsilon\delta A(t,r))^2} + O(\epsilon^2) \approx \epsilon\delta\dot{B} + O(\epsilon^2)\,. \tag{5.48}$$

Therefore, it is easy to see that $\dot{X} \approx \epsilon\delta\ddot{F}$ and $\dot{Y} \approx \epsilon\delta\ddot{B}$. We can now compute the perturbation around Minkowski of Eqn. (5.41) and Eqn. (5.42). This results in the following

$$\delta\ddot{F} = \frac{1}{r^2}\frac{2\sigma}{\omega}\left(\delta B(t,r) - \delta F(t,r)\right) + O(\epsilon)\,, \tag{5.49}$$

$$\delta\ddot{B} = \frac{-1}{r^2}\frac{2\gamma}{\omega}\left(\delta B(t,r) - \delta F(t,r)\right) + O(\epsilon)\,, \tag{5.50}$$

where we have divided through by ϵ to simplify our equations, and dropped all terms that are of order ϵ^2 or higher orders. Using the transformation of $Z = \delta B - \delta F$, $\ddot{Z} = \delta\ddot{B} - \delta\ddot{F}$, we can combine Eqn. (5.49) and Eqn. (5.50) into one equation

$$\ddot{Z} = -\frac{2(\gamma+\sigma)}{r^2\omega}Z \tag{5.51}$$

Simplifying the constants in Eqn. (5.51), results in the final form of Eqn. (5.51)

$$\ddot{Z} = \frac{-2}{r^2}\frac{\alpha+1}{\alpha(\beta-1)}Z \equiv \frac{-2\mathcal{C}}{r^2}Z \tag{5.52}$$

where $\mathcal{C} = \frac{\alpha+1}{\alpha(\beta-1)}$. In this new formulation, we can easily answer the argument that we described earlier, however now the stability no longer depends on the r terms, but instead is a result of considering what happens at $r << 1$ and only considering $\frac{1}{r^2}$ terms. When $\mathcal{C}$ is positive Eqn. (5.52) will be stable, however when $\mathcal{C}$ is negative Eqn. (5.52) will be unstable. It is interesting to note that the stability has no relation on the value of λ, and that for theoretically allowed values of α and β the value of $\mathcal{C}$ could be positive. However, when considering observationally allowed values, $\mathcal{C}$ will be negative, and we should have an instability at small r.

5.5.2 Numerical results: value of $\mathcal{C}$

To test the validity of hypothesis that $\mathcal{C}$ controls the stability of the system at low r, a series of simulations where ran in two regimes: 1.) Varying $\mathcal{C}$ via α and β and λ to broadly check the hypothesis, and; 2) Varying $\mathcal{C}$ with $\alpha = \beta$ and $\lambda = 0$ to reduce our parameter space. For all of the simulations that were undertaken in the regime of 1, we maintained a real propagation speed for the spin-0 modes, i.e Eqn. (5.26)> 0, whereas for simulations performed in the regime of 2 this condition was relaxed.

All simulations were run on a single processor with 4 cores and 12GB of ram[6]. Fig. 5.1 shows the results of all of the simulations ran in regime 1, with Fig. 5.2 highlighting a subset of these results. Fig. 5.3 shows the results of the simulations ran in regime 2. We shall now discuss the results of the simulations with respect to the regimes in turn.

Simulations that were run under the restrictions of regime 1, broadly corresponded to validating our hypothesis i.e a positive C will result in a stable simulation, whereas a negative C will result in an unstable simulation. Note, here we define a stable simulation as one that does not fail, and not as one that successfully forms a universal horizon, or with the Khronon shell dissipating. This shall be discussed

[6]Although unrelated, it should be noted that the computational resources required to run a 1D simulation for the gravitational collapse of the Khronon were vastly smaller then the computational resources need to run a simulation, like the ones specified in Chap. (2-4), with GRChombo.

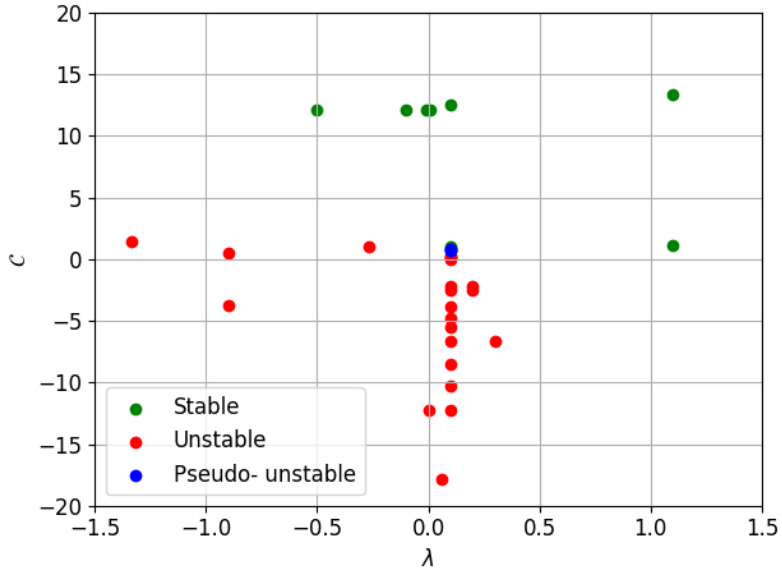

Figure 5.1: The results of a large quantity of simulations with the goal of checking the stability of Eqn. (5.18) while varying $\mathcal{C}$ via α and β and λ. This corresponds to regime 1 within the text and it should be noted that we maintained a real propagation speed for the spin-0 modes. It can be seen that for large positive values of $\mathcal{C}$, we would get stable simulations, however for large negative values of $\mathcal{C}$, we would get unstable simulations. There are also a number simulations with small positive values of $\mathcal{C}$ that resulted in pseudo-unstable or unstable simulations. This indicates that $\mathcal{C}$ does not dictate stability when it's values are small, and other terms in Eqn. (5.18) must be dominating.

at the end of the section. There are a variety of interesting features that arise in this regime.

Fig. 5.1 contains some simulations that would be initially stable to the extent that the incoming Khronon shell would reach small r, before the simulation began to fail. This is in stark contrast to a simulation that outright fails, as in that case the small r instability would cause a failed simulation in a very short amount of time i.e far before the Khronon shell would reach small r. This behaviour was classified as being pseudo-stable, and was not seen for very large or very small values of $\mathcal{C}$.

One can attempt to explain the pseudo-stable behaviour, by simply saying that it encompasses physics that is not described well by the stability according to $\mathcal{C}$, and that other terms in Eqn. (5.18) dominate. A further hint at this, is that for small positive values of $\mathcal{C}$, the simulations would still be unstable, which implies that our hypothesis is valid for large values of $\mathcal{C}$ only.

Fig. 5.2 contains subset of data from Fig. 5.1, where $\lambda = 0.1$ and we vary $\mathcal{C}$. Here, it can be seen that as $\mathcal{C}$ transitions from negative to positive, the stability of the system changes, however as previously stated, a small positive value of $\mathcal{C}$ is not sufficient to get a stable simulation.

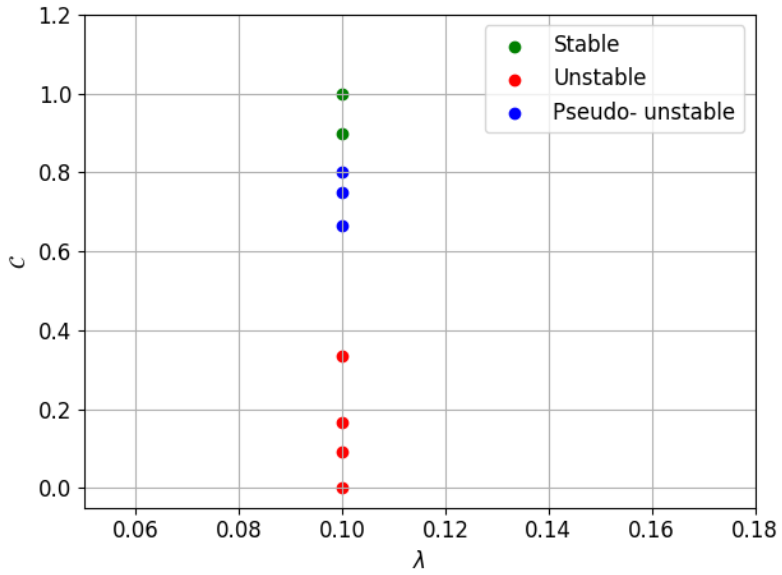

Figure 5.2: A subset of the simulations ran while varying $\mathcal{C}$ via α and β but with $\lambda = 0.1$ i.e regime 1. Here the transition between unstable, pseudo-unstable and stable can be seen as the value of $\mathcal{C}$ transitions from negative to positive.

The simulations performed under regime 1 would suggest that we have found that large values of $\mathcal{C}$ can influence the apparent stability of the system. We will now explore the parameter space of regime 2 such that we can look at a specific slice of our parameter space. We remind the reader that in this regime of exploration, we set $\alpha = \beta$ and $\lambda = 0$. For reference Eqn. (5.51) is reduced to

$$\ddot{Z} = \frac{-2}{r^2}\frac{\alpha+1}{\alpha^2-\alpha}Z\,, \tag{5.53}$$

and the propagation speed squared for the spin-0 modes in Minkowski space becomes

$$s_0^2 = \frac{-2+\alpha}{-2+\alpha+\alpha^2}\,. \tag{5.54}$$

It is not possible to choose α such that we have positive $\mathcal{C}$ factor whilst maintaining a real sound speed for the spin zero mode within the theoretical bounds that $0 \leq \alpha \leq 2$. However, inspired by the parameter choice used in [231][7], we found a parameter space such that $\mathcal{C}$ is negative, however we have stable simulations. This parameter space lies between $0.36 \leq \alpha \leq 0.54$ and Fig. 5.3 shows a summary of these results.

Although this stability region is in contradiction to the hypothesis that $\mathcal{C}$ dictates the stability of the system, it should be noted that this region is where $\mathcal{C}$ is closest to 0. We can then theorise that $\mathcal{C}$ is still having some influence on the stability of

[7]We would like to emphasise to the reader that the paper referenced was done for Einstein-Aether Theory, however there exists a mapping between the parameters of both theories that allowed us to interpret the parameter used in that paper.

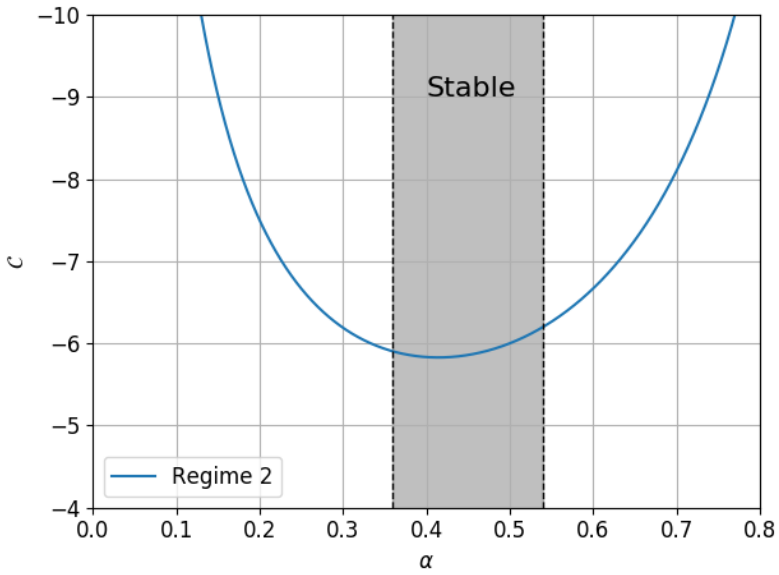

Figure 5.3: Simulations where performed under regime 2, i.e $\alpha = \beta$ and $\lambda = 0$. The grey panel in the region of $0.36 \leq \alpha \leq 0.54$ indicates an area where stable simulations would happen, and curiously, where the value of $\mathcal{C}$ is closest to 0. Simulations outside of this area are unstable.

the system, however there must be other physics not explained by it which become dominant.

Throughout this section we have tried to give some explanation as to why the simulations performed were unstable/unsuccessful. To complete this story we must reiterate that a stable simulation is one that does not fail, and not one that successfully forms a universal horizon, or with the Khronon shell dissipating. To expand on this, when the Khronon shell reaches small r, the simulation does not crash, however the constraint violation, Eqn. (5.27), becomes large i.e our simulations are no longer representative of our system of equations.

With this fact, one can ask why you would call these simulations stable at all? Simply put, the constraint violation becoming large may be a symptom of another problem, so for the purposes of this explanation, simulations running until after the Khronon shell reaches small r are stable. Using the idea that the constraint violation becoming large may be a symptom of another problem, the next section consists of an attempt to regularise our system, and hence lower the constraint violation to acceptable levels.

5.6 Regularisation

The objective of this section is to demonstrate how you can regularise the equations that govern spherically symmetric collapse in Khronometric theory. This was done

in an effort to increase the stability, and ultimately attempt to lower the constraint violation in the simulations that were classified as stable in Sec. 5.5.2, to levels that were acceptable. A number of simulations where conducted to explore if the regularisation achieved this goal, and the results of these are presented later in the section, Sec. 5.6.2.

5.6.1 Modified equations and auxiliary variables

In this section we will present a method to regularise the evolution equations, Eqn. (5.18). We will be using the specific notation and terminology that is used in [20].

We have seen that for $r << 1$, there is some numerical evidence that the stability of the system can be controlled be $\mathcal{C}$. However, when first investigating this phenomena, recall that we sorted Eqn. (5.18) into powers of $1/r^n$ (specifically for the time derivatives of X and Y, and we excluded $\dot{B}_r$ and $\dot{F}_r$ as they did not contain any $1/r^2$ terms). Doing the same sorting exercise for the radial derivative of A, we find that

$$\partial_r^2 A \;=\; \frac{A\left(F^2-B^2\right)}{2\alpha r^2 B^2}+\mathcal{O}\left(\frac{1}{r}\right)+\ldots\,, \tag{5.55}$$

where it should be noted we are not truncating the equations as before, but we are merely algebraically rearranging them. Note we have removed the (t,r) notation for compactness reasons. Regularity dictates that at $r=0$, $A(t,0)=B(t,0)=F(t,0)=1$ and due to the symmetry of A, B and F, the radial derivatives must be equal to 0. When $r=$ small, (r_s), one can note that if we do not want the right hand side of Eqn. (5.55) to rapidly become large, one must impose that $A(t,r_s)=1+A1(t)r_s^2$, $B(t,r_s)=1+B1(t)r_s^2$ and $F(t,r_s)=1+F1(t)r_s^2$. However now we must additionally impose that $F1(t)=B1(t)$, which would stop Eqn. (5.55) rapidly becoming large. This results in our system of differential equations now becoming over-determined. The same problem is present in Eqn. (5.39) and Eqn. (5.40)[8].

Analytically, consistency of our differential equations implies that if our equations are initially satisfied then they will be satisfied for all time, i.e there should be nothing troublesome with what we have described. However numerically because of truncation error the "additional boundary condition" will not be enforced, and hence the $1/r^2$ terms will become large at small r, and cause a rapid numerical instability.

An attempted solution to this problem is to introduce two auxiliary variables

[8]When referring to these equations we want to emphasise that we are referring to the untruncated versions

[257, 258], $J1(t,r)$ and $J2(t,r)$, defined as

$$J1(t,r) \equiv \frac{(B^2-F^2)}{rB^2}, \tag{5.56}$$

$$J2(t,r) \equiv \frac{(F^2-B^2)}{rF^2}, \tag{5.57}$$

$$\tag{5.58}$$

such that the $1/r^2$ terms in Eqn. (5.18) become

$$\partial_r^2 A = -\frac{A}{2\alpha r} J1 + \mathcal{O}\left(\frac{1}{r}\right) + \dots, \tag{5.59}$$

$$\dot{X} = \frac{\sigma A^2}{r\omega F} J1 + \mathcal{O}\left(\frac{1}{r}\right) + \dots, \tag{5.60}$$

$$\dot{Y} = \frac{\gamma A^2}{r\omega B} J2 + \mathcal{O}\left(\frac{1}{r}\right) + \dots. \tag{5.61}$$

As we have added two new auxiliary variables, we must add their corresponding evolution equations. Hence

$$\partial_t J1 = -\frac{2F\left(B\partial_t F - \partial_t B F\right)}{rB^3}, \tag{5.62}$$

$$\partial_t J2 = \frac{2B\left(B\partial_t F - \partial_t B F\right)}{rF^3}. \tag{5.63}$$

At first glance it would appear we have we have simply shifted our $1/r^2$ problem into two equations containing $1/r$, however we can rearrange the constraint equation, Eqn. (5.27), such that

$$\begin{aligned}(B\partial_t F - \partial_t B F) = \frac{r}{2ABF(\beta-1)}\Big[&- 2\partial_r ABF\Big(2\partial_t BF(1+\lambda) + B\partial_t F(\beta+\lambda)\Big) \\ &+A\Big(- 2\partial_r B\partial_t BF^2(\beta+\lambda) + B^2(F\partial_r\partial_t F - \partial_r F\partial_t F)(\beta+\lambda) \\ &+2BF(\partial_r B\partial_t F(-1+\beta)\partial_r\partial_t BF(1+\lambda))\Big)\Big].\end{aligned} \tag{5.64}$$

It can be seen that the right hand side of Eqn. (5.64) contains a r term, that when substituted into Eqn. (5.62) and Eqn. (5.63), will remove the $1/r$ term from the evolution equations for $J1(t,r)$ and $J2(t,r)$. The process of removing troublesome parts of the evolution equations is known as regularisation, and should result in increased stability during evolution.

5.6.2 Numerical results: regularised equations

A large number of simulations where conducted to test whether the regularisation presented in Sec. 5.5.2 had been successful at both increasing the stability of evo-

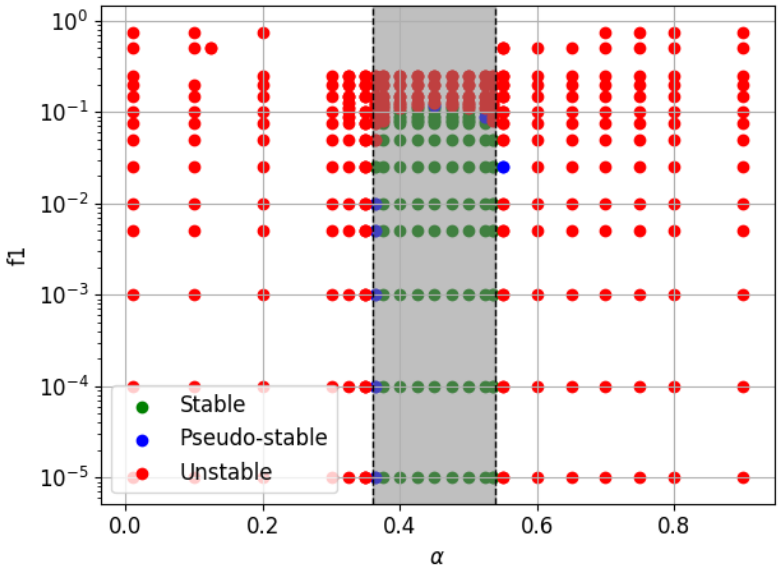

Figure 5.4: The results of a 2D parameter scan of $f1$, and α, where $\alpha = \beta$ and $\lambda = 0$, for the regularised equations. Here it can be seen, as before, that there appears to be a stable region of $0.36 \leq \alpha \leq 0.54$, although as before these simulations have an unacceptably high constraint violation. It would appear that the regularisation has been unsuccessful.

lution, and lowering the constraint violation in simulations that were previously deemed stable. A 2-dimensional parameter space scan was undertaken in α, with $\alpha = \beta$ and $\lambda = 0$, and in $f1$, which we remind the reader is defined as the characteristic size of the incoming Khronon shell. This parameter space should allow us to probe regions in which the gravitational collapse should form a black hole, as well as result in dissipation of the in-falling Khronon shell. The results of this scan are shown in Fig. 5.4, with a subset being showed in Fig. 5.5.

The regularisation scheme described above was unsuccessful due to the stable simulations maintaining an unacceptably high constraint violation. However there are two interesting, although related features of the simulation results, which is best highlighted in Fig. 5.5.

When lowering $f1$, it can be seen that the range in which the values of α correspond to stable simulations increases. A similar feature can be seen when increasing $f1$, and the "stable$(\alpha, f1)$" curve roughly traces out where $\mathcal{C}$ is closest to 0. One could assign 2 potential explanations to this: 1.) $\mathcal{C}$ is managing the stability of our simulations as per Fig. 5.3, or 2.) When $f1$ is small, the incoming khronon shell is small, and via rearranging Eqn. (5.55)

$$\frac{A}{2\alpha r^2}\frac{F^2 - B^2}{B^2} \approx \frac{-A}{2\alpha r^2}\left(1 - \frac{(1 + F1r^2)^2}{(1 + B1r^2)^2}\right) , \tag{5.65}$$

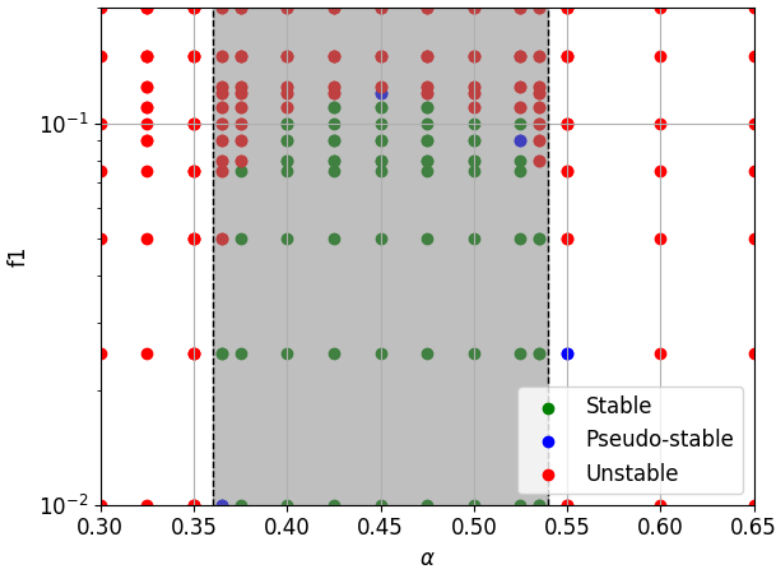

Figure 5.5: A subset of the results of a 2D parameter scan of $f1$, and α, where $\alpha = \beta$ and $\lambda = 0$, for the regularised equations, highlighting the region between unstable and stable. There appears to be different maximum allowed values of $f1$ for a stable simulation for each value of α, although as before these simulations have an unacceptably high constraint violation. The "stable($\alpha, f1$)" curve roughly traces out where $\mathcal{C}$ is closest to 0, so could be a consequence of that.

it is easy to see that as $F1$ and $B1$ will be small values, $\frac{(1+F1r^2)^2}{(1+B1r^2)^2}$, will be closer to 1, and hence numerically, the values generated by truncation error will be smaller, and the simulation is more likely to be deemed as stable. The terms in the second argument have been removed via regularisation, however if there are terms that contain $\frac{1}{r}$, and have a similar structure, this could explain the behaviour.

Ultimately though, the instability of the system could be fully contained within the unconsidered $\frac{1}{r}$ terms in our system, and hence, our regularisation could have simply made instability "not as numerically bad", and not entirely removed it.

5.7 Conclusion

In this chapter we have discussed Lorentz-Violating gravity, and specifically black holes in the low-energy limit of Horava gravity known as Khronometric theory. We have constructed a system of equations, initial conditions and boundary conditions that would allow us to model to collapse of a Khronon shell, and showed that ultimately, the simulations failed due to an apparent instability that occurred at small r. We demonstrated a potential reason for this, with the value of $\mathcal{C}$, Eqn. (5.52), and also attempted to regularise the equations to remove the instability. Regularisation proved ineffective, and we hypothesised that there could be more terms of the structure $\frac{1}{r}\left(1 - \frac{1+\kappa}{1+\delta}\right)$ that could be causing an instability to occur.

With that in mind, one can suggest another method for numerically stabilising our system. If we were to introduce an additional damping term such that at small r, if $\kappa \neq \delta$, we slowly realign the values to be equal, it could potentially stabilise our system, providing this additional term condition did not cause a large constraint violation. This would have to be tuned by hand, and we could encounter problems at the small r cut-off where we impose this "brute force" condition.

Alternatively one can go back to the regularisation, and attempt to analyse all $1/r^n$ like terms to see if they can be removed. This has not yet been shown to be possible.

Since this research was performed, the allowed parameter space for the 3 coupling constants was shown to be significantly reduced as a result of the GWs from the NS-NS binary coalescence [240–242]. The parameter space is expected to be further reduced with the detection of GWs from extreme mass ratio BH-BH binary coalescence events with LISA. However, in [242] it was shown that for slowly moving BHs, for generic values of the coupling constants a curvature singularity appears at the universal horizon. In contrast, if $\alpha = \beta = 0$ and $\lambda \neq 0$, slowly moving BHs become regular everywhere, and coincide with BHs from GR. This subset of coupling constants coincides with those selected by the recent constraints.

Due to the form of our system of equations, we cannot impose the subset of coupling constants due to $1/\alpha$ terms being present. Therefore to study the subset of coupling constants we would need to rederive the equations themselves. This presents an avenue of future research.

Chapter 6

Conclusion

"Live long and prosper."

Mr Spock
Star Trek: The Original Series

Throughout this thesis we have examined two distinct topics; dark matter (DM), and Khronometric theory. Although the topics are different, the examination of them has shared a common approach; the use of numerical techniques to solve problems that cannot be solved analytically. When studying DM physics in full General Relativity (GR), we utilised the well known Arnowitt Deser Misner (ADM) decomposition to split spacetime into *space and time*, before solving for a number of scenarios using GRChombo. In contrast, Khronometric theory contains a natural foliation defined by the Khronon scalar field, and hence, we use a custom code written using PETSc to study this topic. We shall now comment on both areas of study.

When referring to the study of DM throughout the work presented here, we specifically refer to axions as our chosen DM model. We simulated a quasi-stable, localised oscillating solution to the equations of motion of a scalar field known as an axion star, which is a type of exotic compact object (ECO). As these objects undergo gravitational collapse, either they can remain stable, hence remaining as an axion star, or form black holes, or, if the axion decay constant, f_a, is low, disperse in a so called "axion star supernovae". In Chap. 2, we simulated the formation of compact axion stars from aspherical initial conditions that could represent the final stages of axion dark matter structure formation, and showed that this follows the well known relationship[1] of initial mass and axion decay constant, f_a, first studied in [114]. Within the same work, we used a toy model to demonstrate how this information can be used to predict the number densities and masses of such compact objects, and find that they could be detectable by the LIGO/Virgo collaboration for an axion

[1] See Fig. 1.8.

mass of $10^{-9} < m_a < 10^{-11}$ eV. Furthermore, we showed using peak statistics that there exists a "mass gap" between the masses of axion stars and black holes formed from collapse when studying $f_a < 0.2M_{pl}$.

As our study of DM continued into Chap. 3 and Chap. 4, we considered oscillotons (OS), which are a good approximation of an axion star where the leading order ϕ^4 interaction is negligible due to having a large axion decay constant, f_a. Specifically, in Chap. 3, we investigated the physics of black hole formation from the head-on collisions of boosted equal mass OS, for both the cases where the OS have equal phases or are maximally off-phase (anti-phase). While unboosted OS collisions will form a BH as long as their initial compactness $\mathcal{C} \equiv GM/R$ is above a numerically determined critical value $\mathcal{C} > 0.035$, we found that imparting a small initial boost counter-intuitively *prevents* the formation of black holes even if $\mathcal{C} > 0.035$. If the boost is further increased, at very high boosts $\gamma > 1/12\mathcal{C}$, BH formation occurs as predicted by the hoop conjecture, leading to a "stability band" where collisions result in either the OS "passing through" (equal phase) or "bouncing back" (anti-phase), with a "critical point" occurring around $\mathcal{C} \approx 0.07$. We argued that the existence of this stability band can be explained by the competition between the free fall and the interaction timescales of the collision.

In Chap. 4 we presented in detail how to construct the initial data for a boosted pair of OS as well as the modifications needed during evolution. We commented on the further use of this initial data, focussing on two scenarios; OS-OS binary coalescence and colliding OS with an impact parameter. If the first scenario is simulated, it could provide gravitational wave (GW) templates, that could be used by the LIGO/Virgo collaboration, or future LISA mission, to search for DM. If these signals were detected, it would be a smoking gun for the existence of DM, and more specifically, OS and/or axion stars. The latter scenario is currently being explored in a paper in prep with Thomas Helfer, Eugene Lim, Marcos A.G. Garcia, and Mustafa A. Amin.

Signalling the end of our exploration of DM, Chap. 5 detailed our study of a form of Lorentz-Violating (LV) gravity known as Khronometric theory. Within this chapter, we showed the equations and initial conditions for spherically symmetric collapse of the Khronon field, and presented our numerical results. We were unsuccessful in simulating the collapse, even after a reformulation of the equations of motion using auxiliary variables to remove the $1/r^2$ from them. We found that this could be linked with a value of $\mathcal{C}$, which is the combination of some of the model parameters. Since this work was undertaken, due to the neutron star (NS)-NS binary coalesce detected by LIGO/Virgo, it was shown in [240, 241] that the constraints on the model parameters have increased by several orders of magnitudes. However, in [242] it was shown that for slowly moving BHs, for generic values of the coupling

constants a curvature singularity appears at the universal horizon. In contrast, if $\alpha = \beta = 0$ and $\lambda \neq 0$, slowly moving BHs become regular everywhere, and coincide with BHs from GR. This reduced parameter space for the coupling constants is a possible avenue of future research.

It is hoped that the work presented throughout this thesis will provide useful insight and knowledge that will lead to the furthering of the field. On a personal note, this thesis marks my departure from Physics, and the transition into the field of deep learning. I direct the interested reader to my first paper within this new field, [259], which is about the optimization of binarized neural networks.

Bibliography

[1] K. Clough, P. Figueras, H. Finkel, M. Kunesch, E. A. Lim and S. Tunyasuvunakool, *GRChombo : Numerical Relativity with Adaptive Mesh Refinement*, *Class. Quant. Grav.* **32** (2015) 245011 [1503.03436].

[2] J. Y. Widdicombe, T. Helfer, D. J. E. Marsh and E. A. Lim, *Formation of Relativistic Axion Stars*, *JCAP* **1810** (2018) 005 [1806.09367].

[3] J. Y. Widdicombe, T. Helfer and E. A. Lim, *Black hole formation in relativistic Oscillaton collisions*, *JCAP* **01** (2020) 027 [1910.01950].

[4] M. J. Turk, B. D. Smith, J. S. Oishi, S. Skory, S. W. Skillman, T. Abel et al., *yt: A Multi-code Analysis Toolkit for Astrophysical Simulation Data*, *The Astrophysical Journal Supplement Series* **192** (2011) 9 [1011.3514].

[5] E. Jones, T. Oliphant, P. Peterson et al., *SciPy: Open source scientific tools for Python*, 2001.

[6] J. D. Hunter, *Matplotlib: A 2d graphics environment*, *Computing In Science & Engineering* **9** (2007) 90.

[7] LIGO Scientific Collaboration and Virgo Collaboration collaboration, *Observation of gravitational waves from a binary black hole merger*, *Phys. Rev. Lett.* **116** (2016) 061102.

[8] LIGO Scientific Collaboration and Virgo Collaboration collaboration, *Gw151226: Observation of gravitational waves from a 22-solar-mass binary black hole coalescence*, *Phys. Rev. Lett.* **116** (2016) 241103.

[9] LIGO Scientific and Virgo Collaboration collaboration, *Gw170104: Observation of a 50-solar-mass binary black hole coalescence at redshift 0.2*, *Phys. Rev. Lett.* **118** (2017) 221101.

[10] B. P. Abbott, R. Abbott, T. D. Abbott, F. Acernese, K. Ackley, C. Adams et al., *Gw170608: Observation of a 19 solar-mass binary black hole coalescence*, *The Astrophysical Journal Letters* **851** (2017) L35.

[11] LIGO Scientific Collaboration and Virgo Collaboration collaboration, *Gw170814: A three-detector observation of gravitational waves from a binary black hole coalescence*, *Phys. Rev. Lett.* **119** (2017) 141101.

[12] Virgo, LIGO Scientific collaboration, *GWTC-1: A Gravitational-Wave Transient Catalog of Compact Binary Mergers Observed by LIGO and Virgo during the First and Second Observing Runs*, 1811.12907.

[13] B. P. Abbott, R. Abbott, T. D. Abbott, F. Acernese, K. Ackley, C. Adams et al., *GW170817: Observation of Gravitational Waves from a Binary Neutron Star Inspiral*, *Physical Review Letters* **119** (2017) 161101 [1710.05832].

[14] B. P. Abbott, R. Abbott, T. D. Abbott, F. Acernese, K. Ackley, C. Adams et al., *Gravitational waves and gamma-rays from a binary neutron star merger: Gw170817 and grb 170817a*, *The Astrophysical Journal Letters* **848** (2017) L13.

[15] B. P. Abbott, R. Abbott, T. D. Abbott, F. Acernese, K. Ackley, C. Adams et al., *Multi-messenger observations of a binary neutron star merger*, *The Astrophysical Journal Letters* **848** (2017) L12.

[16] B. F.Schutz, *A First Course in General Relativity*. Cambridge University Press, 1985.

[17] S. M. Carroll, *Spacetime and geometry: An introduction to general relativity*. 2004.

[18] A. Einstein, *Zur elektrodynamik bewegter körper*, *Annalen der Physik* **322** (1905) 891 [https://onlinelibrary.wiley.com/doi/pdf/10.1002/andp.19053221004].

[19] A. Einstein, *Ist die trägheit eines körpers von seinem energieinhalt abhängig?*, *Annalen der Physik* **323** (1905) 639 [https://onlinelibrary.wiley.com/doi/pdf/10.1002/andp.19053231314].

[20] M. Alcubierre, *Introduction to 3+1 Numerical Relativity*, International Series of Monographs on Physics. OUP Oxford, 2008.

[21] A. Einstein, *Die Feldgleichungen der Gravitation*, *Sitzungsberichte der Königlich Preußischen Akademie der Wissenschaften (Berlin), Seite 844-847.* (1915) .

[22] J. A. Wheeler, *A journey into gravity and spacetime / John Archibald Wheeler*. Scientific American Library : Distributed by W. H. Freeman and Co New York, 1990.

[23] A. Einstein, *Die grundlage der allgemeinen relativitätstheorie*, *Annalen der Physik* **354** (1916) 769 [https://onlinelibrary.wiley.com/doi/pdf/10.1002/andp.19163540702].

[24] F. W. Dyson, A. S. Eddington and C. Davidson, *Ix. a determination of the deflection of light by the sun's gravitational field, from observations made at the total eclipse of may 29, 1919*, *Philosophical Transactions of the Royal Society of London. Series A, Containing Papers of a Mathematical or Physical Character* **220** (1920) 291 [https://royalsocietypublishing.org/doi/pdf/10.1098/rsta.1920.0009].

[25] R. V. Pound and G. A. Rebka, *Gravitational red-shift in nuclear resonance*, *Phys. Rev. Lett.* **3** (1959) 439.

[26] T. W. Baumgarte and S. L. Shapiro, *Numerial Relativity : Solving Einstein's Equations on the Computer* . CUP, 2010.

[27] H.-a. Shinkai, *Formulations of the Einstein equations for numerical simulations*, *J. Korean Phys. Soc.* **54** (2009) 2513 [0805.0068].

[28] E. Gourgoulhon, *3+1 formalism and bases of numerical relativity*, gr-qc/0703035.

[29] R. L. Arnowitt, S. Deser and C. W. Misner, *The Dynamics of general relativity*, *Gen. Rel. Grav.* **40** (2008) 1997 [gr-qc/0405109].

[30] J. W. York, Jr., *Kinematics and dynamics of general relativity*, in *Sources of Gravitational Radiation*, L. L. Smarr, ed., pp. 83–126, 1979.

[31] M. Alcubierre, *Introduction to 3+1 numerical relativity*, *Introduction to 3+1 Numerical Relativity* (2006) .

[32] S. Frittelli, *Note on the propagation of the constraints in standard (3+1) general relativity*, *Phys. Rev.* **D55** (1997) 5992.

[33] A. Lichnerowicz, *L'intégration des équations de la gravitation relativiste et le problème des n corps.*, *J. Math. Pures Appl. (9)* **23** (1944) 37.

[34] J. W. York, *Gravitational degrees of freedom and the initial-value problem*, *Phys. Rev. Lett.* **26** (1971) 1656.

[35] J. W. York, Jr., *Role of conformal three geometry in the dynamics of gravitation*, *Phys. Rev. Lett.* **28** (1972) 1082.

[36] J. W. York, Jr., *Conformal 'thin sandwich' data for the initial-value problem*, *Phys. Rev. Lett.* **82** (1999) 1350 [gr-qc/9810051].

[37] S. G. Hahn and R. W. Lindquist, *The two-body problem in geometrodynamics*, *Annals of Physics* **29** (1964) 304 .

[38] B. Reimann, *Slice stretching at the event horizon when geodesically slicing the Schwarzschild spacetime with excision*, *Class. Quant. Grav.* **21** (2004) 4297 [gr-qc/0405016].

[39] C. Bona, J. Masso, E. Seidel and J. Stela, *A New formalism for numerical relativity*, *Phys. Rev. Lett.* **75** (1995) 600 [gr-qc/9412071].

[40] T. Nakamura, Y. Kojima and K. Oohara, *General Relativistic Collapse to Black Holes and Gravitational Waves from Black Holes*, *Progress of Theoretical Physics Supplement* **90** (1987) 1.

[41] M. Shibata and T. Nakamura, *Evolution of three-dimensional gravitational waves: Harmonic slicing case*, *Phys. Rev. D* **52** (1995) 5428.

[42] T. W. Baumgarte and S. L. Shapiro, *On the numerical integration of Einstein's field equations*, *Phys. Rev.* **D59** (1999) 024007 [gr-qc/9810065].

[43] M. Campanelli, C. O. Lousto, P. Marronetti and Y. Zlochower, *Accurate evolutions of orbiting black-hole binaries without excision*, *Phys. Rev. Lett.* **96** (2006) 111101 [gr-qc/0511048].

[44] O. Sarbach, G. Calabrese, J. Pullin and M. Tiglio, *Hyperbolicity of the BSSN system of Einstein evolution equations*, *Phys. Rev.* **D66** (2002) 064002 [gr-qc/0205064].

[45] P. A. M. Dirac, *Fixation of coordinates in the hamiltonian theory of gravitation*, *Physical Review - PHYS REV X* **114** (1959) 924.

[46] L. Smarr and J. W. York, *Radiation gauge in general relativity*, *Phys. Rev. D* **17** (1978) 1945.

[47] M. Alcubierre, B. Bruegmann, P. Diener, M. Koppitz, D. Pollney, E. Seidel et al., *Gauge conditions for long term numerical black hole evolutions without excision*, *Phys. Rev.* **D67** (2003) 084023 [gr-qc/0206072].

[48] J. G. Baker, J. Centrella, D.-I. Choi, M. Koppitz and J. van Meter, *Gravitational wave extraction from an inspiraling configuration of merging black holes*, *Phys. Rev. Lett.* **96** (2006) 111102 [gr-qc/0511103].

[49] M. Hannam, S. Husa, F. Ohme, B. Bruegmann and N. O'Murchadha, *Wormholes and trumpets: The Schwarzschild spacetime for the moving-puncture generation*, *Phys.Rev.* **D78** (2008) 064020 [0804.0628].

[50] J. Schombert, *Galaxies and the expanding universe lecture notes*, .

[51] C. M. da Silva Ph.D, *Neolithic cosmology: The equinox and the spring full moon*, *Journal of Cosmology* **9** (2010) 2207.

[52] A. Liddle, *An Introduction to Modern Cosmology*. Wiley, 2003.

[53] Planck Collaboration collaboration, *Planck 2013 results. I. Overview of products and scientific results*, *Astron.Astrophys.* **571** (2014) A1 [1303.5062].

[54] A. S. Eddington and A. G. Lemaître, *The Expanding Universe*, *Monthly Notices of the Royal Astronomical Society* **91** (1931) 490.

[55] E. Hubble, *A relation between distance and radial velocity among extra-galactic nebulae*, *Proceedings of the National Academy of Sciences* **15** (1929) 168 [https://www.pnas.org/content/15/3/168.full.pdf].

[56] M. J. Mortonson, D. H. Weinberg and M. White, *Dark Energy: A Short Review*, 1401.0046.

[57] Planck collaboration, *Planck 2018 results. VI. Cosmological parameters*, 1807.06209.

[58] D. Baumann, *Inflation*, in *Physics of the large and the small, TASI 09, proceedings of the Theoretical Advanced Study Institute in Elementary Particle Physics, Boulder, Colorado, USA, 1-26 June 2009*, pp. 523–686, 2011, 0907.5424, DOI.

[59] Wikimedia Commons, "Timeline of the universe." https://commons.wikimedia.org/wiki/File:CMB_Timeline300_no_WMAP.jpg.

[60] K. Freese, *Review of Observational Evidence for Dark Matter in the Universe and in upcoming searches for Dark Stars*, *EAS Publ. Ser.* **36** (2009) 113 [0812.4005].

[61] G. Bertone and D. Hooper, *History of dark matter*, *Rev. Mod. Phys.* **90** (2018) 045002 [1605.04909].

[62] V. C. Rubin and J. Ford, W. Kent, *Rotation of the Andromeda Nebula from a Spectroscopic Survey of Emission Regions*, *ApJ* **159** (1970) 379.

[63] A. Bosma, *21-cm line studies of spiral galaxies. II. The distribution and kinematics of neutral hydrogen in spiral galaxies of various morphological types.*, *AJ* **86** (1981) 1825.

[64] V. C. Rubin, J. Ford, W. K., N. Thonnard and D. Burstein, *Rotational properties of 23Sb galaxies.*, *ApJ* **261** (1982) 439.

[65] M. Milgrom, *A modification of the Newtonian dynamics as a possible alternative to the hidden mass hypothesis.*, *ApJ* **270** (1983) 365.

[66] J. K. Adelman-McCarthy, M. A. Agüeros, S. S. Allam, K. S. J. Anderson, S. F. Anderson, J. Annis et al., *The Fourth Data Release of the Sloan Digital Sky Survey*, *ApJS* **162** (2006) 38 [astro-ph/0507711].

[67] U. G. Briel and J. P. Henry, *An X-ray temperature map of Coma*, in *Untangling Coma Berenices: A New Vision of an Old Cluster*, A. Mazure, F. Casoli, F. Durret and D. Gerbal, eds., p. 170, Jan., 1998, astro-ph/9711237.

[68] M. Markevitch, A. H. Gonzalez, D. Clowe, A. Vikhlinin, W. Forman, C. Jones et al., *Direct constraints on the dark matter self-interaction cross section from the merging galaxy cluster 1e 0657-56*, *The Astrophysical Journal* **606** (2004) 819.

[69] B. Carr, F. Kuhnel and M. Sandstad, *Primordial Black Holes as Dark Matter*, *Phys. Rev.* **D94** (2016) 083504 [1607.06077].

[70] Y. B. Zel'dovich and I. D. Novikov, *The Hypothesis of Cores Retarded during Expansion and the Hot Cosmological Model*, *Soviet Ast.* **10** (1967) 602.

[71] S. Hawking, *Gravitationally collapsed objects of very low mass*, *MNRAS* **152** (1971) 75.

[72] B. J. Carr and S. W. Hawking, *Black Holes in the Early Universe*, *Monthly Notices of the Royal Astronomical Society* **168** (1974) 399.

[73] P. Meszaros, *The behaviour of point masses in an expanding cosmological substratum*, *A&A* **37** (1974) 225.

[74] LIGO Scientific, Virgo collaboration, *Search for Subsolar-Mass Ultracompact Binaries in Advanced LIGO's First Observing Run*, *Phys. Rev. Lett.* **121** (2018) 231103 [1808.04771].

[75] Y. Ali-Haïmoud and M. Kamionkowski, *Cosmic microwave background limits on accreting primordial black holes*, *Phys. Rev. D* **95** (2017) 043534.

[76] A. S. Josan, A. M. Green and K. A. Malik, *Generalised constraints on the curvature perturbation from primordial black holes*, *Phys. Rev.* **D79** (2009) 103520 [0903.3184].

[77] H. Niikura, M. Takada, N. Yasuda, R. H. Lupton, T. Sumi, S. More et al., *Microlensing constraints on $10^{-10}M_\odot$-scale primordial black holes from high-cadence observation of M31 with Hyper Suprime-Cam*, *ArXiv e-prints* (2017) [1701.02151].

[78] T. Bringmann, P. F. Depta, V. Domcke and K. Schmidt-Hoberg, *Strong constraints on clustered primordial black holes as dark matter*, 1808.05910.

[79] G. Arcadi, M. Dutra, P. Ghosh, M. Lindner, Y. Mambrini, M. Pierre et al., *The waning of the WIMP? A review of models, searches, and constraints*, *Eur. Phys. J.* **C78** (2018) 203 [1703.07364].

[80] Z. G. Berezhiani, M. Yu. Khlopov and R. R. Khomeriki, *Cosmic Nonthermal Electromagnetic Background from Axion Decays in the Models with Low Scale of Family Symmetry Breaking*, *Sov. J. Nucl. Phys.* **52** (1990) 65.

[81] Z. G. Berezhiani and M. Yu. Khlopov, *Cosmology of Spontaneously Broken Gauge Family Symmetry*, *Z. Phys.* **C49** (1991) 73.

[82] A. S. Sakharov and M. Yu. Khlopov, *The Nonhomogeneity problem for the primordial axion field*, *Phys. Atom. Nucl.* **57** (1994) 485.

[83] Z. G. Berezhiani, A. S. Sakharov and M. Yu. Khlopov, *Primordial background of cosmological axions*, *Sov. J. Nucl. Phys.* **55** (1992) 1063.

[84] R. Peccei and H. R. Quinn, *CP Conservation in the Presence of Instantons*, *Phys. Rev. Lett.* **38** (1977) 1440.

[85] S. Weinberg, *A New Light Boson?*, *Phys. Rev. Lett.* **40** (1978) 223.

[86] F. Wilczek, *Problem of Strong p and t Invariance in the Presence of Instantons*, *Phys. Rev. Lett.* **40** (1978) 279.

[87] A. G. Dias, A. C. B. Machado, C. C. Nishi, A. Ringwald and P. Vaudrevange, *The quest for an intermediate-scale accidental axion and further ALPs*, *Journal of High Energy Physics* **6** (2014) 37 [1403.5760].

[88] J. Jaeckel and A. Ringwald, *The Low-Energy Frontier of Particle Physics*, *Annual Review of Nuclear and Particle Science* **60** (2010) 405 [1002.0329].

[89] P. Svrcek and E. Witten, *Axions in string theory*, *JHEP* **6** (2006) 51 [hep-th/0605206].

[90] A. Arvanitaki, S. Dimopoulos, S. Dubovsky, N. Kaloper and J. March-Russell, *String axiverse*, *Phys. Rev. D* **81** (2010) 123530 [0905.4720].

[91] J. P. Conlon, *The QCD axion and moduli stabilisation*, *Journal of High Energy Physics* **5** (2006) 078 [hep-th/0602233].

[92] D. J. E. Marsh, *Axion Cosmology*, *Phys. Rept.* **643** (2016) 1 [1510.07633].

[93] M. Cicoli, M. Goodsell and A. Ringwald, *The type IIB string axiverse and its low-energy phenomenology*, *JHEP* **10** (2012) 146 [1206.0819].

[94] A. Arvanitaki, S. Dimopoulos, S. Dubovsky, N. Kaloper and J. March-Russell, *String Axiverse*, *Phys. Rev.* **D81** (2010) 123530 [0905.4720].

[95] D. J. E. Marsh, *Axion Cosmology*, *Phys. Rept.* **643** (2016) 1 [1510.07633].

[96] R. Peccei, *The Strong CP problem and axions*, *Lect. Notes Phys.* **741** (2008) 3 [hep-ph/0607268].

[97] D. di Wu, *A brief introduction to the strong cp problem*, *Zeitschrift für Naturforschung A* **52** (1997) .

[98] A. Hook, *TASI Lectures on the Strong CP Problem and Axions*, *PoS* **TASI2018** (2019) 004 [1812.02669].

[99] G. 't Hooft, *Symmetry breaking through bell-jackiw anomalies*, *Phys. Rev. Lett.* **37** (1976) 8.

[100] C. Baker et al., *An Improved experimental limit on the electric dipole moment of the neutron*, *Phys. Rev. Lett.* **97** (2006) 131801 [hep-ex/0602020].

[101] B. D. Fields, P. Molaro and S. Sarkar, *Big-Bang Nucleosynthesis*, *Chin. Phys. C* **38** (2014) 339 [1412.1408].

[102] R. D. Peccei and H. R. Quinn, CP *conservation in the presence of pseudoparticles*, *Phys. Rev. Lett.* **38** (1977) 1440.

[103] C. Vafa and E. Witten, *Parity conservation in quantum chromodynamics*, *Phys. Rev. Lett.* **53** (1984) 535.

[104] F. Wilczek, *Problem of strong p and t invariance in the presence of instantons*, *Phys. Rev. Lett.* **40** (1978) 279.

[105] S. Weinberg, *A new light boson?*, *Phys. Rev. Lett.* **40** (1978) 223.

[106] M. Shifman, A. Vainshtein and V. Zakharov, *Can confinement ensure natural cp invariance of strong interactions?*, *Nuclear Physics B* **166** (1980) 493 .

[107] J. E. Kim, *Weak-interaction singlet and strong* CP *invariance*, *Phys. Rev. Lett.* **43** (1979) 103.

[108] M. Dine, W. Fischler and M. Srednicki, *A simple solution to the strong cp problem with a harmless axion*, *Physics Letters B* **104** (1981) 199 .

[109] A. Zhitnitsky, *On Possible Suppression of the Axion Hadron Interactions. (In Russian)*, *Sov. J. Nucl. Phys.* **31** (1980) 260.

[110] P. Svrcek and E. Witten, *Axions In String Theory*, *JHEP* **06** (2006) 051 [hep-th/0605206].

[111] J. E. Kim, *Light Pseudoscalars, Particle Physics and Cosmology*, *Phys. Rept.* **150** (1987) 1.

[112] S. Dimopoulos, S. Kachru, J. McGreevy and J. G. Wacker, *N-flation*, *JCAP* **0808** (2008) 003 [hep-th/0507205].

[113] M. S. Turner, *Coherent scalar-field oscillations in an expanding universe*, *Phys. Rev. D* **28** (1983) 1243.

[114] T. Helfer, D. J. E. Marsh, K. Clough, M. Fairbairn, E. A. Lim and R. Becerril, *Black hole formation from axion stars*, *JCAP* **3** (2017) 055 [1609.04724].

[115] E. Braaten and H. Zhang, *Axion Stars*, 1810.11473.

[116] I. Tkachev, *On the possibility of bose-star formation*, *Physics Letters B* **261** (1991) 289 .

[117] D. J. Kaup, *Klein-gordon geon*, *Physical Review* **172** (1968) 1331.

[118] R. Ruffini and S. Bonazzola, *Systems of Self-Gravitating Particles in General Relativity and the Concept of an Equation of State*, *Physical Review* **187** (1969) 1767.

[119] A. R. Liddle and M. S. Madsen, *The Structure and formation of boson stars*, *Int.J.Mod.Phys.* **D1** (1992) 101.

[120] E. Seidel and W.-M. Suen, *Formation of solitonic stars through gravitational cooling*, *Physical Review Letters* **72** (1994) 2516 [gr-qc/9309015].

[121] E. Seidel and W.-M. Suen, *Oscillating soliton stars*, *Physical Review Letters* **66** (1991) 1659.

[122] D. G. Levkov, A. G. Panin and I. I. Tkachev, *Relativistic Axions from Collapsing Bose Stars*, *Physical Review Letters* **118** (2017) 011301 [1609.03611].

[123] L. Visinelli, S. Baum, J. Redondo, K. Freese and F. Wilczek, *Dilute and dense axion stars*, *Phys. Lett.* **B777** (2018) 64 [1710.08910].

[124] J. Barranco and A. Bernal, *Self-gravitating system made of axions*, *Phys. Rev. D* **83** (2011) 043525 [1001.1769].

[125] F. Michel and I. G. Moss, *Relativistic collapse of axion stars*, 1802.10085.

[126] M. Alcubierre, R. Becerril, S. F. Guzman, T. Matos, D. Nunez and L. A. Urena-Lopez, *Numerical studies of Phi**2 oscillatons*, *Class. Quant. Grav.* **20** (2003) 2883 [gr-qc/0301105].

[127] H.-Y. Schive, M.-H. Liao, T.-P. Woo, S.-K. Wong, T. Chiueh, T. Broadhurst et al., *Understanding the Core-Halo Relation of Quantum Wave Dark Matter from 3D Simulations*, *Phys. Rev. Lett.* **113** (2014) 261302 [1407.7762].

[128] K. Clough, *Scalar Fields in Numerical General Relativity: Inhomogeneous inflation and asymmetric bubble collapse*, Ph.D. thesis, King's Coll. London, Cham, 2017. 1704.06811. 10.1007/978-3-319-92672-8.

[129] S. Tunyasuvunakool, *Applications of Numerical Relativity Beyond Astrophysics*, Ph.D. thesis, Cambridge U., 2017. 10.17863/CAM.7743.

[130] M. Kunesch, *Numerical simulations of instabilities in general relativity*, Ph.D. thesis, 2018. 10.17863/CAM.30498.

[131] M. Adams, P. Colella, D. T. Graves, J. N. Johnson, N. D. Keen, T. J. Ligocki et al., *Chombo Software Package for AMR Applications - Design Document, Lawrence Berkeley National Laboratory Technical Report LBNL-6616E.*, .

[132] M. Berger and J. Oliger, *Adaptive mesh refinement for hyperbolic partial differential equations*, *J. Comput. Phys.* (1984) 484.

[133] M. J. Berger and P. Colella, *Local adaptive mesh refinement for shock hydrodynamics*, *Journal of Computational Physics* **82** (1989) 64.

[134] M. J. Berger and I. Rigoutsos, *An algorithm for point clustering and grid generation*, *IEEE Trans. Sys. Man & Cyber.* **21** (1991) 1278.

[135] M. P. Forum, *Mpi: A message-passing interface standard*, .

[136] L. Dagum and R. Menon, *Openmp: An industry-standard api for shared-memory programming*, *IEEE Comput. Sci. Eng.* **5** (1998) 46.

[137] H.-O. Kreiss and G. Scherer, *Method of lines for hyperbolic differential equations*, *SIAM Journal on Numerical Analysis* **29** (1992) 640.

[138] H. Kreiss, H. Kreiss, J. Oliger and G. A. R. P. J. O. Committee, *Methods for the approximate solution of time dependent problems*, GARP publications series. International Council of Scientific Unions, World Meteorological Organization, 1973.

[139] G. F. Giudice, M. McCullough and A. Urbano, *Hunting for dark particles with gravitational waves*, *JCAP* **10** (2016) 001 [1605.01209].

[140] V. Cardoso, S. Hopper, C. F. B. Macedo, C. Palenzuela and P. Pani, *Gravitational-wave signatures of exotic compact objects and of quantum corrections at the horizon scale*, *Phys. Rev.* **D94** (2016) 084031 [1608.08637].

[141] L. Hui, J. P. Ostriker, S. Tremaine and E. Witten, *Ultralight scalars as cosmological dark matter*, *Phys. Rev.* **D95** (2017) 043541 [1610.08297].

[142] C. Palenzuela, I. Olabarrieta, L. Lehner and S. L. Liebling, *Head-on collisions of boson stars*, *Phys. Rev.* **D75** (2007) 064005 [gr-qc/0612067].

[143] R. Brito, V. Cardoso, C. F. B. Macedo, H. Okawa and C. Palenzuela, *Interaction between bosonic dark matter and stars*, *Phys. Rev.* **D93** (2016) 044045 [1512.00466].

[144] C. Hanna, M. C. Johnson and L. Lehner, *Estimating gravitational radiation from super-emitting compact binary systems*, *Phys. Rev.* **D95** (2017) 124042 [1611.03506].

[145] X. Du, B. Schwabe, J. C. Niemeyer and D. Bürger, *Tidal disruption of fuzzy dark matter subhalo cores*, *Phys. Rev.* **D97** (2018) 063507 [1801.04864].

[146] J. Veltmaat, J. C. Niemeyer and B. Schwabe, *Formation and structure of ultralight bosonic dark matter halos*, *Phys. Rev.* **D98** (2018) 043509 [1804.09647].

[147] H.-Y. Schive, T. Chiueh and T. Broadhurst, *Cosmic Structure as the Quantum Interference of a Coherent Dark Wave*, *Nature Phys.* **10** (2014) 496 [1406.6586].

[148] B. Schwabe, J. C. Niemeyer and J. F. Engels, *Simulations of solitonic core mergers in ultralight axion dark matter cosmologies*, *Phys. Rev. D* **94** (2016) 043513 [1606.05151].

[149] D. G. Levkov, A. G. Panin and I. I. Tkachev, *Gravitational Bose-Einstein condensation in the kinetic regime*, *Phys. Rev. Lett.* **121** (2018) 151301 [1804.05857].

[150] P. Ajith et al., *Inspiral-merger-ringdown waveforms for black-hole binaries with non-precessing spins*, *Phys. Rev. Lett.* **106** (2011) 241101 [0909.2867].

[151] T. Helfer, E. A. Lim, M. A. G. Garcia and M. A. Amin, *Gravitational Wave Emission from Collisions of Compact Scalar Solitons*, *Phys. Rev.* **D99** (2019) 044046 [1802.06733].

[152] T. Banks, M. Dine, P. J. Fox and E. Gorbatov, *On the possibility of large axion decay constants*, *JCAP* **06** (2003) 001 [hep-th/0303252].

[153] N. Arkani-Hamed, L. Motl, A. Nicolis and C. Vafa, *The String landscape, black holes and gravity as the weakest force*, *JHEP* **06** (2007) 060 [hep-th/0601001].

[154] E. Silverstein and A. Westphal, *Monodromy in the CMB: Gravity Waves and String Inflation*, *Phys. Rev. D* **78** (2008) 106003 [0803.3085].

[155] T. C. Bachlechner, M. Dias, J. Frazer and L. McAllister, *Chaotic inflation with kinetic alignment of axion fields*, *Phys. Rev. D* **91** (2015) 023520 [1404.7496].

[156] B. Heidenreich, M. Reece and T. Rudelius, *Weak Gravity Strongly Constrains Large-Field Axion Inflation*, *JHEP* **12** (2015) 108 [1506.03447].

[157] T. C. Bachlechner, C. Long and L. McAllister, *Planckian Axions and the Weak Gravity Conjecture*, *JHEP* **01** (2016) 091 [1503.07853].

[158] P.-H. Chavanis, *Phase transitions between dilute and dense axion stars*, *Phys. Rev.* **D98** (2018) 023009 [1710.06268].

[159] K. Clough, E. A. Lim, B. S. DiNunno, W. Fischler, R. Flauger and S. Paban, *Robustness of Inflation to Inhomogeneous Initial Conditions*, *JCAP* **1709** (2017) 025 [1608.04408].

[160] X. Du, C. Behrens, J. C. Niemeyer and B. Schwabe, *Core-halo mass relation of ultralight axion dark matter from merger history*, *Phys. Rev.* **D95** (2017) 043519 [1609.09414].

[161] A. S. Sakharov, D. D. Sokoloff and M. Yu. Khlopov, *Large scale modulation of the distribution of coherent oscillations of a primordial axion field in the universe*, *Phys. Atom. Nucl.* **59** (1996) 1005.

[162] C. J. Hogan and M. J. Rees, *Axion miniclusters*, *Phys. Lett. B* **205** (1988) 228.

[163] E. W. Kolb and I. I. Tkachev, *Nonlinear axion dynamics and formation of cosmological pseudosolitons*, *Phys. Rev.* **D49** (1994) 5040 [astro-ph/9311037].

[164] M. Khlopov, A. Sakharov and D. Sokoloff, *The nonlinear modulation of the density distribution in standard axionic cdm and its cosmological impact*, *Nuclear Physics B - Proceedings Supplements* **72** (1999) 105 .

[165] U. H. Hernandez-Belmonte, V. Ayala-Ramirez and R. E. Sanchez-Yanez, *A comparative review of two-pass connected component labeling algorithms*, in *Advances in Soft Computing*, I. Batyrshin and G. Sidorov, eds., (Berlin, Heidelberg), pp. 452–462, Springer Berlin Heidelberg, 2011.

[166] A. Rosenfeld and J. L. Pfaltz, *Sequential operations in digital picture processing*, *J. ACM* **13** (1966) 471.

[167] L. D. Stefano and A. Bulgarelli, *A simple and efficient connected components labeling algorithm*, in *Proceedings 10th International Conference on Image Analysis and Processing*, pp. 322–327, 1999, DOI.

[168] L. He, Y. Chao, K. Suzuki and K. Wu, *Fast connected-component labeling*, *Pattern Recognition* **42** (2009) 1977 .

[169] K. Suzuki, I. Horiba and N. Sugie, *Linear-time connected-component labeling based on sequential local operations*, *Comput. Vis. Image Underst.* **89** (2003) 1.

[170] S. Bird, I. Cholis, J. B. Muñoz, Y. Ali-Haïmoud, M. Kamionkowski, E. D. Kovetz et al., *Did LIGO detect dark matter?*, *ArXiv e-prints* **116** (2016) 201301 [1603.00464].

[171] D. Croon, M. Gleiser, S. Mohapatra and C. Sun, *Gravitational Radiation Background from Boson Star Binaries*, 1802.08259.

[172] R. Brito, S. Ghosh, E. Barausse, E. Berti, V. Cardoso, I. Dvorkin et al., *Gravitational wave searches for ultralight bosons with LIGO and LISA*, *Phys. Rev.* **D96** (2017) 064050 [1706.06311].

[173] M. W. Choptuik and F. Pretorius, *Ultra Relativistic Particle Collisions*, *Phys. Rev. Lett.* **104** (2010) 111101 [0908.1780].

[174] N. Sennett, T. Hinderer, J. Steinhoff, A. Buonanno and S. Ossokine, *Distinguishing Boson Stars from Black Holes and Neutron Stars from Tidal Interactions in Inspiraling Binary Systems*, *Phys. Rev.* **D96** (2017) 024002 [1704.08651].

[175] C. Palenzuela, P. Pani, M. Bezares, V. Cardoso, L. Lehner and S. Liebling, *Gravitational Wave Signatures of Highly Compact Boson Star Binaries*, *Phys. Rev.* **D96** (2017) 104058 [1710.09432].

[176] M. Bezares, C. Palenzuela and C. Bona, *Final fate of compact boson star mergers*, *Phys. Rev.* **D95** (2017) 124005 [1705.01071].

[177] B. J. Carr, *Primordial black holes: Recent developments*, *eConf* **C041213** (2004) 0204 [astro-ph/0504034].

[178] S. Kasuya and M. Kawasaki, *Axion isocurvature fluctuations with extremely blue spectrum*, *Phys. Rev.* **D80** (2009) 023516 [0904.3800].

[179] D. J. Chung and A. Upadhye, *Bump in the blue axion isocurvature spectrum*, *Phys. Rev.* **D95** (2017) 023503 [1610.04284].

[180] G. Efstathiou and J. R. Bond, *Isocurvature cold dark matter fluctuations*, *MNRAS* **218** (1986) 103.

[181] M. Yu. Khlopov and A. G. Polnarev, *PRIMORDIAL BLACK HOLES AS A COSMOLOGICAL TEST OF GRAND UNIFICATION*, *Phys. Lett.* **97B** (1980) 383.

[182] T. Harada, C.-m. Yoo, K. Kohri, K.-i. Nakao and S. Jhingan, *Primordial Black Hole Formation in the Matter-dominated Phase of the Universe*, *ApJ* **833** (2016) 61 [1609.01588].

[183] G. D. Coughlan, W. Fischler, E. W. Kolb, S. Raby and G. G. Ross, *Cosmological problems for the polonyi potential*, *Phys. Lett. B* **131** (1983) 59.

[184] L. Iliesiu, D. J. E. Marsh, K. Moodley and S. Watson, *Constraining supersymmetry with heavy scalars: Using the CMB*, *Phys. Rev. D* **89** (2014) 103513 [1312.3636].

[185] Y. Kahn, B. R. Safdi and J. Thaler, *Broadband and Resonant Approaches to Axion Dark Matter Detection*, *Phys. Rev. Lett.* **117** (2016) 141801 [1602.01086].

[186] D. Budker, P. W. Graham, M. Ledbetter, S. Rajendran and A. O. Sushkov, *Proposal for a Cosmic Axion Spin Precession Experiment (CASPEr)*, *Phys. Rev. X* **4** (2014) 021030 [1306.6089].

[187] L. Di Luzio, F. Mescia and E. Nardi, *Redefining the Axion Window*, *Phys. Rev. Lett.* **118** (2017) 031801 [1610.07593].

[188] T. Lee and Y. Pang, *Nontopological solitons*, *Physics Reports* **221** (1992) 251 .

[189] M. Colpi, S. L. Shapiro and I. Wasserman, *Boson stars: Gravitational equilibria of self-interacting scalar fields*, *Phys. Rev. Lett.* **57** (1986) 2485.

[190] J. A. Wheeler, *Geons*, *Phys. Rev.* **97** (1955) 511.

[191] E. A. Power and J. A. Wheeler, *Thermal geons*, *Rev. Mod. Phys.* **29** (1957) 480.

[192] K. Clough, T. Dietrich and J. C. Niemeyer, *Axion star collisions with black holes and neutron stars in full 3D numerical relativity*, 1808.04668.

[193] T. Dietrich, F. Day, K. Clough, M. Coughlin and J. Niemeyer, *Neutron star – axion star collisions in the light of multi-messenger astronomy*, 1808.04746.

[194] T. Dietrich, S. Ossokine and K. Clough, *Full 3D Numerical Relativity Simulations of Neutron Star – Boson Star Collisions with BAM*, 1807.06959.

[195] D. N. Page, *Classical and quantum decay of oscillatons: Oscillating selfgravitating real scalar field solitons*, *Phys. Rev.* **D70** (2004) 023002 [gr-qc/0310006].

[196] X. Du, C. Behrens and J. C. Niemeyer, *Substructure of fuzzy dark matter haloes*, *MNRAS* **465** (2017) 941 [1608.02575].

[197] M. A. Amin and P. Mocz, *Formation, Gravitational Clustering and Interactions of Non-relativistic Solitons in an Expanding Universe*, 1902.07261.

[198] W. E. East and F. Pretorius, *Ultrarelativistic black hole formation*, *Phys. Rev. Lett.* **110** (2013) 101101 [1210.0443].

[199] L. Rezzolla and K. Takami, *Black-hole production from ultrarelativistic collisions*, *Class. Quant. Grav.* **30** (2013) 012001 [1209.6138].

[200] K. S. Thorne, *Nonspherical Gravitational Collapse–A Short Review*, p. 231. 1972.

[201] S. L. Liebling and C. Palenzuela, *Dynamical Boson Stars*, *Living Rev. Rel.* **15** (2012) 6 [1202.5809].

[202] *Movie for oscillaton in-phase collision C = 0.065 v = 0.3c : https://youtu.be/mOPzPxIaDVg* .

[203] *Movie for oscillaton in-phase collision C = 0.065 v = 0.5c : https://youtu.be/ZyYhJlYN3d8* .

[204] *Movie for oscillaton in-phase collision C = 0.065 v = 0.7c : https://youtu.be/66uwXSIY8tI* .

[205] J. T. Giblin, Jr, L. Hui, E. A. Lim and I.-S. Yang, *How to Run Through Walls: Dynamics of Bubble and Soliton Collisions*, *Phys. Rev.* **D82** (2010) 045019 [1005.3493].

[206] M. A. Amin, E. A. Lim and I.-S. Yang, *A scattering theory of ultrarelativistic solitons*, *Phys. Rev.* **D88** (2013) 105024 [1308.0606].

[207] M. A. Amin, E. A. Lim and I.-S. Yang, *Clash of Kinks: Phase Shifts in Colliding Nonintegrable Solitons*, *Phys. Rev. Lett.* **111** (2013) 224101 [1308.0605].

[208] H. Okawa, H. Witek and V. Cardoso, *Black holes and fundamental fields in Numerical Relativity: initial data construction and evolution of bound states*, *Phys. Rev.* **D89** (2014) 104032 [1401.1548].

[209] *Movie for oscillaton off-phase collision C = 0.065 v = 0.3c : https://youtu.be/NyaB3zjtaQ4* .

[210] *Movie for oscillaton off-phase collision C = 0.065 v = 0.5c : https://youtu.be/uACT89NESHw* .

[211] *Movie for oscillaton off-phase collision C = 0.065 v = 0.7c : https://youtu.be/bdYYbXSgUcY* .

[212] A. Paredes and H. Michinel, *Interference of dark matter solitons and galactic offsets*, *Physics of the Dark Universe* **12** (2016) 50 [1512.05121].

[213] M. Alcubierre, R. Becerril, F. S. Guzmán, T. Matos, D. Núñez and L. A. Ureña-López, *Numerical studies of Φ^2-oscillatons*, *Classical and Quantum Gravity* **20** (2003) 2883 [gr-qc/0301105].

[214] L. A. Ureña-López, T. Matos and R. Becerril, *Inside oscillatons*, *Class. Quant. Grav.* **19** (2002) 6259.

[215] L. A. Ureña-López, *Oscillatons revisited*, *Class. Quant. Grav.* **19** (2002) 2617 [gr-qc/0104093].

[216] R. Becerril, T. Matos and L. Ureña-López, *Geodesics around oscillatons*, *General Relativity and Gravitation - GEN RELATIV GRAVIT* **38** (2006) 633.

[217] J. M. Bardeen and T. Piran, *General relativistic axisymmetric rotating systems: coordinates and equations.*, *Phys. Rep.* **96** (1983) 205.

[218] M. W. Choptuik, *Consistency of finite-difference solutions of einstein's equations*, *Phys. Rev. D* **44** (1991) 3124.

[219] C. R. Evans, *An approach for calculating axisymmetric gravitational collapse*, in *Dynamical Spacetimes and Numerical Relativity*, J. M. Centrella, ed., pp. 3–39, 1986.

[220] P. Figueras, M. Kunesch and S. Tunyasuvunakool, *End point of black ring instabilities and the weak cosmic censorship conjecture*, *Phys. Rev. Lett.* **116** (2016) 071102.

[221] P. Figueras, M. Kunesch, L. Lehner and S. Tunyasuvunakool, *End Point of the Ultraspinning Instability and Violation of Cosmic Censorship*, *Phys. Rev. Lett.* **118** (2017) 151103 [1702.01755].

[222] M. P. Hertzberg and E. D. Schiappacasse, *Scalar dark matter clumps with angular momentum*, *JCAP* **1808** (2018) 028 [1804.07255].

[223] KAGRA, LIGO Scientific, VIRGO collaboration, *Prospects for Observing and Localizing Gravitational-Wave Transients with Advanced LIGO, Advanced Virgo and KAGRA*, *Living Rev. Rel.* **21** (2018) 3 [1304.0670].

[224] T. Clifton, P. G. Ferreira, A. Padilla and C. Skordis, *Modified Gravity and Cosmology*, *Phys. Rept.* **513** (2012) 1 [1106.2476].

[225] Virgo, LIGO Scientific collaboration, *Tests of general relativity with GW150914*, *Phys. Rev. Lett.* **116** (2016) 221101 [1602.03841].

[226] LIGO Scientific, Virgo collaboration, *Tests of General Relativity with GW170817*, 1811.00364.

[227] A. Einstein, *Näherungsweise Integration der Feldgleichungen der Gravitation, Sitzungsberichte der Königlich Preußischen Akademie der Wissenschaften (Berlin), Seite 688-696.* (1916) .

[228] A. Rocci, *On first attempts to reconcile quantum principles with gravity*, *J. Phys. Conf. Ser.* **470** (2013) 012004 [1309.7336].

[229] P. Horava, *Quantum Gravity at a Lifshitz Point*, *Phys. Rev.* **D79** (2009) 084008 [0901.3775].

[230] E. Barausse, T. Jacobson and T. P. Sotiriou, *Black holes in Einstein-aether and Horava-Lifshitz gravity*, *Phys. Rev.* **D83** (2011) 124043 [1104.2889].

[231] D. Garfinkle, C. Eling and T. Jacobson, *Numerical simulations of gravitational collapse in Einstein-aether theory*, *Phys. Rev.* **D76** (2007) 024003 [gr-qc/0703093].

[232] M. Bhattacharjee, S. Mukohyama, M.-B. Wan and A. Wang, *Gravitational collapse and formation of universal horizons in Einstein-aether theory*, *Phys. Rev.* **D98** (2018) 064010 [1806.00142].

[233] D. Hansen, N. Yunes and K. Yagi, *Projected Constraints on Lorentz-Violating Gravity with Gravitational Waves*, *Phys. Rev.* **D91** (2015) 082003 [1412.4132].

[234] D. Blas, O. Pujolas and S. Sibiryakov, *On the Extra Mode and Inconsistency of Horava Gravity*, *JHEP* **10** (2009) 029 [0906.3046].

[235] D. Blas and H. Sanctuary, *Gravitational Radiation in Horava Gravity*, *Phys. Rev.* **D84** (2011) 064004 [1105.5149].

[236] D. Blas, O. Pujolas and S. Sibiryakov, *Models of non-relativistic quantum gravity: The Good, the bad and the healthy*, *JHEP* **04** (2011) 018 [1007.3503].

[237] D. Blas, O. Pujolas and S. Sibiryakov, *Consistent Extension of Horava Gravity*, *Phys. Rev. Lett.* **104** (2010) 181302 [0909.3525].

[238] E. Barausse and T. P. Sotiriou, *Black holes in Lorentz-violating gravity theories*, *Class. Quant. Grav.* **30** (2013) 244010 [1307.3359].

[239] K. Yagi, D. Blas, E. Barausse and N. Yunes, *Constraints on Einstein-aether theory and Ho?ava gravity from binary pulsar observations*, *Phys. Rev.* **D89** (2014) 084067 [1311.7144].

[240] A. Emir Gümrükçüoğlu, M. Saravani and T. P. Sotiriou, *Hořava gravity after GW170817*, *Phys. Rev.* **D97** (2018) 024032 [1711.08845].

[241] Y. Gong, S. Hou, E. Papantonopoulos and D. Tzortzis, *Gravitational waves and the polarizations in Hořava gravity after GW170817*, *Phys. Rev.* **D98** (2018) 104017 [1808.00632].

[242] O. Ramos and E. Barausse, *Constraints on Hořava gravity from binary black hole observations*, *Phys. Rev.* **D99** (2019) 024034 [1811.07786].

[243] B. Audren, D. Blas, M. M. Ivanov, J. Lesgourgues and S. Sibiryakov, *Cosmological constraints on deviations from Lorentz invariance in gravity and dark matter*, *JCAP* **1503** (2015) 016 [1410.6514].

[244] S. M. Carroll and E. A. Lim, *Lorentz-violating vector fields slow the universe down*, *Phys. Rev.* **D70** (2004) 123525 [hep-th/0407149].

[245] J. Oost, S. Mukohyama and A. Wang, *Constraints on Einstein-aether theory after GW170817*, *Phys. Rev.* **D97** (2018) 124023 [1802.04303].

[246] J. Bhattacharyya, A. Coates, M. Colombo and T. P. Sotiriou, *Evolution and spherical collapse in Einstein-Aether theory and Horava gravity*, *Phys. Rev.* **D93** (2016) 064056 [1512.04899].

[247] T. Jacobson, *Extended Horava gravity and Einstein-aether theory*, *Phys. Rev.* **D81** (2010) 101502 [1001.4823].

[248] M. Bonetti and E. Barausse, *Post-Newtonian constraints on Lorentz-violating gravity theories with a MOND phenomenology*, *Phys. Rev.* **D91** (2015) 084053 [1502.05554].

[249] L. Blanchet and S. Marsat, *Modified gravity approach based on a preferred time foliation*, *Phys. Rev.* **D84** (2011) 044056 [1107.5264].

[250] R. Penrose, *Gravitational collapse: The role of general relativity*, *Riv. Nuovo Cim.* **1** (1969) 252.

[251] M. W. Choptuik, *Universality and scaling in gravitational collapse of a massless scalar field*, *Phys. Rev. Lett.* **70** (1993) 9.

[252] D. Blas and S. Sibiryakov, *Horava gravity versus thermodynamics: The Black hole case*, *Phys. Rev.* **D84** (2011) 124043 [1110.2195].

[253] A. Wang, *Hořava Gravity at a Lifshitz Point: A Progress Report*, 1701.06087.

[254] J. Bhattacharyya, M. Colombo and T. P. Sotiriou, *Causality and black holes in spacetimes with a preferred foliation*, *Class. Quant. Grav.* **33** (2016) 235003 [1509.01558].

[255] C. Eling and T. Jacobson, *Black Holes in Einstein-Aether Theory*, *Class. Quant. Grav.* **23** (2006) 5643 [gr-qc/0604088].

[256] S. Balay, S. Abhyankar, M. F. Adams, J. Brown, P. Brune, K. Buschelman et al., "PETSc Web page." http://www.mcs.anl.gov/petsc, 2016.

[257] M. Alcubierre and J. A. Gonzalez, *Regularization of spherically symmetric evolution codes in numerical relativity*, *Comput. Phys. Commun.* **167** (2005) 76 [gr-qc/0401113].

[258] A. Arbona and C. Bona, *Dealing with the center and boundary problems in 1d numerical relativity*, *Computer Physics Communications* **118** (1999) 229 .

[259] K. Helwegen, J. Widdicombe, L. Geiger, Z. Liu, K.-T. Cheng and R. Nusselder, *Latent weights do not exist: Rethinking binarized neural network optimization*, in *Advances in Neural Information Processing Systems 32*, pp. 7533–7544, Curran Associates, Inc., (2019), http://papers.nips.cc/paper/8971-latent-weights-do-not-exist-rethinking-binarized-neural-network-optimization.pdf.